Spring 1-1-2015

Electrowetting Variable Optics for Visible and Infrared Applications

Alexander Maxwell Watson
University of Colorado at Boulder, watsonam13@gmail.com

ELECTROWETTING VARIABLE OPTICS FOR VISIBLE AND INFRARED APPLICATIONS

by

ALEXANDER MAXWELL WATSON

B.E.E., University of Dayton, 2010

M.S., University of Dayton, 2011

A thesis submitted to the

Faculty of the Graduate School of the

University of Colorado in partial fulfillment

of the requirement for the degree of

Doctor of Philosophy

Department of Mechanical Engineering

2015

This thesis entitled:
Electrowetting Variable Optics for Visible and Infrared Applications
written by Alexander Maxwell Watson
has been approved for the Department of Mechanical Engineering

_____

_____

Date_____

The final copy of this thesis has been examined by the signatories, and we find that both the content and the form meet acceptable presentation standards of scholarly work in the above mentioned discipline.

Watson, Alexander Maxwell (Ph.D., Mechanical Engineering)

Electrowetting Variable Optics for Visible and Infrared Applications

Thesis directed by Professor Victor M. Bright

Miniaturized variable optical devices are important for the fields of medical technology, optical communication, and consumer imaging devices. Areas ranging from endoscopy and optogenetics to atomic clocks and imaging all benefit from versatile optical systems. These applications all require precise and rapid control of imaging focal depth and lateral scanning. Electrowetting variable optics is one emergent technology that has the capability to provide focus tuning, beam steering, and even phase modulation in a small and robust package which requires no moving parts. Furthermore, electrowetting based devices there are attractive due to their transmissive nature, polarization insensitivity, low insertion loss, low electrical power requirements, and high optical quality. These features mean that electrowetting adaptive optical components are an attractive solution, compared with MEMS and liquid crystal optical components.

Electrowetting is a technique that enables control of the shape of a liquid droplet with applied voltage. A conductive droplet on a dielectric surface alters its contact angle due to charges that build up between an underlying electrode and the surface of the droplet. This effect can be used to tune the curvature and tilt of liquids within cavities. The liquid boundary creates a high quality surface to use for lensing or steering applications. This thesis will focus on the development of electrowetting

based lenses and prisms and applications in imaging for both visible and infrared wavelengths.

Within this dissertation is the first demonstration of electrowetting lenses for phase control, as well as the investigation of non-aqueous electrowetting lens liquids for electrowetting lenses operation in the infrared. Key considerations that affect the performance and reliability are dielectric material and thickness, liquid selection and source of ionic conduction. The optical devices presented herein utilize judicious selection of dielectric material and electrowetting liquids to enable low voltage variable optics and demonstrate applications in microscopy and microendoscopy.

ACKNOWLEDGEMENTS

I was always told that graduate school would be the most difficult time in my life. Indeed, after going through it, I have to admit it was the most challenging endeavor of my life, though not in the way I had first imagined. I had excelled in college and naively assumed graduate school would be more of the same: a technical challenge, but with specific set goals given to me to work toward. What was most difficult was taking a project from proposal ideas and independently developing the goals for myself. Learning to do this effectively for an engineering or research project is, in my opinion, the value of studying in graduate school. I am very thankful for the opportunities and guidance provided by my advisor Dr. Victor Bright. He taught me the essential lessons for time management, goal setting, effective communication, and professionalism in research by his words and his actions. Exposing me to proposal writing experience and educating me on the nuances of project management are lessons I will take with me in my career and life.

Research in graduate school requires discipline and vision. I was very lucky to have Dr. Juliet Gopinath's guidance as my co-advisor and leader of the electrowetting group at CU Boulder. Her dedication to the projects and her students kept the group moving forward in a direction that was beneficial to us all. I learned a great deal about experimental design and how to effectively collaborate with other students on multidisciplinary projects.

I would like to thank the members of the electrowetting group:

- Robert Niederriter, for working closely with me the first couple years and doing all of the optical setup and analysis for our first paper and lens

array device. He was also instrumental in setting up the knife-edge measurement for my infrared lenses characterization.

- Soraya Terrab, for learning as much about electrowetting in one year as I did in three so that we could make a great team in tacking the challenges of electrowetting together. She developed and fabricated the electrowetting prisms that I used to characterize the beam steering in the infrared. She also designed and fabricated the optical shutter device.
- Kevin Dease, for his strong effort in characterizing the liquid lens aberrations in the second publication. He was also responsible for calculating the magnification of the lens used in the compound microscope.
- Ryan Montoya, the super undergraduate who led the effort to further develop the optical shutter.
- Omkar Supekar, who has the noble job of carrying the electrowetting torch for the future projects.
- Dr. Andrew Jones and Dr. Keith Cobry, for sharing their knowledge of optics design and electrowetting design, respectively.

I would extend my gratitude to all of the members who were part of Prof. Bright's MEMS group while I was there: Dr. Joseph Brown, Dr. Jason Gray, Dr. Harris Hall, Dr. Matthew Brubaker, Dr. Joel Weber, Dr. Christopher Oshman, Nathan Eigenfeld, Jonas Gertsch, Cully Little, Yizi Xu, and Kristin Genter. Their insight into everything from the fundamental phenomena of physics and fabrication challenges to the minutiae of everyday graduate research taught me more than I could learn in any class.

I would like to express my gratitude to Chris Roath and VSI Parylene for their professional assistance in all of the parylene coatings used in our devices. His service and friendship allowed this research to move forward quickly and reliably.

I had the pleasure of working closely with another co-advisor from the National Institute of Science and Technology, Dr. James Booth. He was a fantastic boss and a very inspiring presence to work with in the lab. Even though our research effort wasn't based on electrowetting and isn't covered in this thesis, I am very thankful for working with him and learned a great deal about microwave circuit design and microfluidics, both of which I am utilizing in my new job.

One of my most cherished opportunities I had in graduate school was the chance to work on an amazing multidisciplinary microendoscope project with collaborators in both Bioengineering and Neuroscience at CU Denver. I'm grateful for microscopy expert Dr. Emily Gibson and co-director of the Center for NeuroScience Dr. Diego Restrepo for sharing their knowledge and expertise on brain endoscopy, showing me the true potential for the optics that I am developing. I'd like to thank their students Baris Ozbay and Justin Losacco for a fun and exciting partnership in developing the microendoscope. They were both solely responsible for the development of the fiber-coupled microendoscope which we modified to integrate my electrowetting lens for application demonstration.

I'm very happy to have had the assistance of Tzu-Min Oh, Ryan Brow, Zefram Marks and the staff at the Colorado Nanofabrication Laboratory. Without their expert advice, I might still be scratching my head in the lab there today.

Thank you to Dr. Robert Cormack, Dr. Carol Cogswell and Ramzi Zahreddine for their insight in the optical characterization of the liquid lenses from the first publication.

I'd like to also thank Dr. David Alchenberger, Dr. Parag Shah, Dr. Darren Forman, Ryan Glugla, Martha Bodine, Kenneth Underwood, Molly Krogstad and

Dennice Roberts for their professional assistance in all of my optical characterization needs.

I am grateful for funding throughout my time in graduate school from the following organizations: National Science Foundation (NSF) IDBR DBI-1353757 grant, The Butcher Program from the University of Colorado Boulder, NSF SBIR with Dr. Erik Thoen of Verdant Networks, DARPA Microsystems Technology Office DARPA-BAA-12-64, the Professional Research Experience Program funding from the National Institute of Science and Technology, the Chief of Naval Research (CNR) Challenge Program Award N00014-11-1-0574, the NNIN at the Colorado Nanofabrication Laboratory and the National Science Foundation under grant ECS-0335765.

I'd like to express my deep appreciation for the lively discussions of all things science with Dr. Zheng Zhang, Lewis Cox, Paul Schroeder, Scott Wieland and Trevor DiMartino.

Finally, I am very thankful for the love and support I received from my parents, Ed and Cindy Watson and my brothers Ben and Danny. Your love and encouragement helped me through the toughest time in my life and I cannot fully express how much that means to me.

Alexander M. Watson

CONTENTS

FIGURES

CHAPTER I – INTRODUCTION

Electrowetting traces its roots to 1875 when Gabriel Lippmann performed the first experiments showing that liquid contact angle can be altered with an applied voltage [1]. Lippmann called the effect electrocapillarity, and was able to create a very sensitive electrometer and a motor based on his studies [2]. However, in Lippmann's investigation, an electrolyte (conducting liquid) was placed in direct contact with liquid mercury. The method suffered from an inherent flaw: only a few hundred millivolts could be applied before the onset of electrolyte decomposition due to high currents halted the experiment. Because of this problem, the idea of practical electrowetting was shelved for over a century, until the pioneering work of Berge [3] in the early 1990s enabled resurgence in the field. Berge included a dielectric between conductive droplet and metal electrode, raising the threshold for electrolysis significantly. A basic schematic of electrowetting of a liquid droplet is shown below in Figure 1-1.

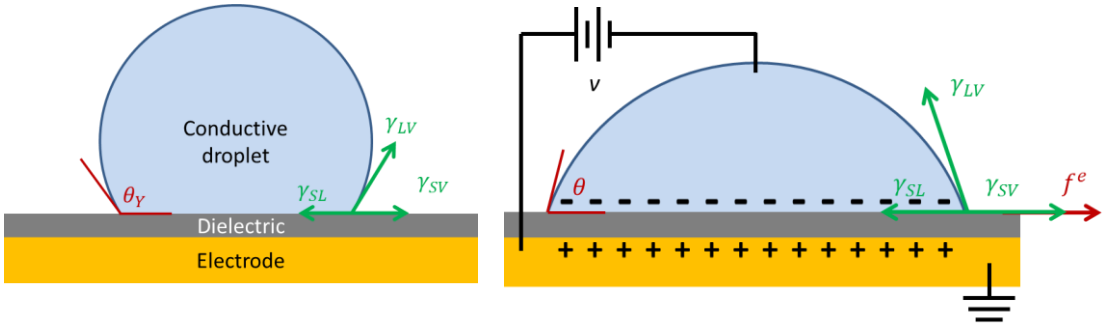

Figure 1-1 Basic schematic of electrowetting of liquid droplet. The surface tension forces γ between substrate, liquid and vapor phases balance to form a resting contact angle θ_Y. By applying a potential v, charges build up and pull the droplet toward the substrate, resulting in a net electrowetting force, f^e that rebalances the surface tension forces and creates new contact angle θ.

With this new innovation, the door was opened for electrowetting in practical applications. The number of journal publications in electrowetting has increased exponentially since 2000. Applications include variable optical components like lenses and prisms [4-28], optical switches [29-30], lab-on-chip bio assays [31-46], and displays [47-57].

As the demand for smaller, more compact imaging systems continues to grow for medical devices such as endoscopes and commercial products like cell phone cameras, the demand for switchable, agile optics follows the same trend. The goal for adaptive optics is to recreate the same quality of solid optics, but allow for variable performance which ultimately reduces the real estate needed to employ the variable optics within the imaging system. The challenge is to design quality miniature optical systems with high quality, despite the reduction in numerical aperture that comes with miniaturization. Electrowetting-based variable optics can satisfy this need, with devices that have a transmissive geometry, small size, low operating voltages [58-59], fast response time[19], [60-61], low insertion losses, polarization insensitivity, large tuning range [13], [15], [23] and good optical quality [13], [21]. These properties make electrowetting a more versatile and favorable option than existing technologies like spatial light modulators [62-63], microelectromechanical segmented and deformable mirrors [64-67], piezo-actuated deformable mirrors, and membrane-based lenses [9], [68-69].

Another beneficial feature is the capacitive nature of electrowetting. Devices store energy and consume very little power, even with voltage applied [13]. The low power consumption makes devices ideal candidates for light tracking devices for solar energy applications [6] or light steering devices for room lighting or headlights.

Additionally, electrowetting lenses and prisms can provide the three degrees of freedom necessary for complete wavefront control. With liquid lenses, we can

control the curvature of a wavefront propagating through the device; with an electrowetting prism, we can also control the tip-tilt or beam steering angle [6], [8]. The third aspect of wavefront engineering requires control over the piston, or phase of transmitted light, which can be achieved by placing the electrowetting lens at the focal point of a fixed lens telescope [21]. Thus, electrowetting optics has the power to compensate for all aspects of a distorted waveform, making it a very attractive tool for free space communication. Given the broad scope of applications, the study of the electrowetting phenomenon becomes more imperative, especially considering the relatively young state the research is currently in. The size of these devices might be considered on the mezzo scale: small for a standard optical device, but still large for a "chip-scale" device. The device dimensions are within millimeter range, containing microliter volumes of liquids, and utilizing down to nanometer thickness thin films to implement the electrowetting-on-dielectrics capability.

The primary focus of this research is the development of liquid optical devices based on electrowetting, with a focus on low operating voltage and exploring new, non-aqueous electrowetting materials to enable converging lens modes and to increase the wavelength of operation to the infrared. Chapter II will detail the fundamentals of electrowetting and review the development of electrowetting based optics from its invention in 2000 to the present. It also includes a discussion of the design parameters required for an electrowetting lens system. The two different liquid lens systems created and characterized are covered in Chapter III, with their performance compared to previous electrowetting lens systems reported in literature. In the second liquid lens system, applications for microscopy and microendoscopy are demonstrated and detailed in Chapter IV. Two non-aqueous polar liquids are explored in this lens system: propylene glycol and a room temperature ionic liquid. The former is covered as part of Chapter III while the latter is used in both a lens and prism device featured in Chapter V.

CHAPTER II – FUNDAMENTAL PRICIPLES OF ELECTROWEETING

2.1 **Theory of Electrowetting**

The electrowetting effect is a surface phenomenon. As the dimensions of a liquid droplet reach millimeter sizes and the coatings approach submicron thicknesses, the surface-area-to-volume-ratio vastly increases. At these scales, surface tension becomes the dominant force, and gravity is negligible [70]. The dimensionless Bond number provides guidance as to whether one is operating in a surface tension or gravity-dominated regime. The Bond number measures the ratio of gravitational force to surface energy of the liquid-vapor interface of a droplet in ambient air:

$$B_o = \frac{\rho_L g h^2}{\gamma_{lv}} \tag{2.1}$$

where ρ_L is liquid density (or density difference between two liquids, in the case of a two liquid system), g is the gravitational acceleration, h is the height of the spherical cap and γ_{lv} is the interfacial energy at the liquid – vapor boundary. When $B_o \ll 1$, we observe that capillary surface forces dominate over gravitational effects. This typically occurs for droplets on the millimeter scale and below [70].

An electromechanical approach is the most rigorous way to evaluate the forces in electrowetting as the phenomenon is a mechanical motion driven by electrical stimulus. To derive the basic formulas used to predict the operation of liquids under applied voltage, a conductive sessile droplet on top of an ideal hydrophobic dielectric material and an electrode is analyzed, as seen in Figure 2-1.

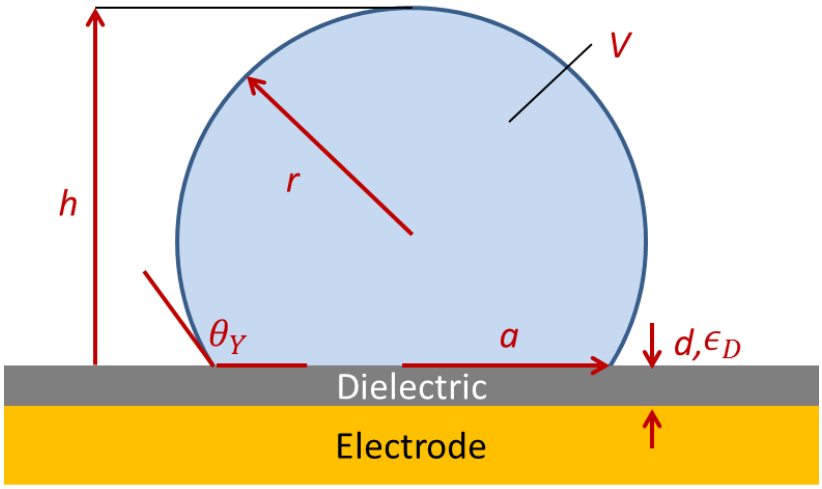

Figure 2-1 Cross-sectional view of sessile droplet on dielectric/electrode. V is the droplet volume, h is the droplet height, r is the radius of curvature, a is the radius of contact, d is the thickness of the dielectric, ϵ_d is the dielectric constant and θ_Y is the initial Young's contact angle.

Since the droplet has fixed volume V, Berthier [71] and Jones [72] have shown a relationship between the droplet height h, the radius of contact a, the radius of the spherical cap r, and the contact angle θ. The relationships are as follows:

$$h^3 + 3a^2h - \frac{6V}{\pi} = 0 \tag{2.2}$$

$$r = \frac{h^2+a^2}{2h} \tag{2.3}$$

$$cos\theta_Y = \sqrt{1 - \left(\frac{a}{r}\right)^2} \tag{2.4}$$

The best choice for a variable to continue the analysis is the radius of circular contact since it can be physically identified with the capillary and electrostatic forces. The dimensions of the radius align with the forces observed during electrowetting actuation [72].

The spherical surface area, A_{LV} and circular contact area of the droplet, A_{SL} are:

$$A_{LV}(a) = 2\pi r(a)h(a) \tag{2.5}$$

$$A_{SL} = \pi a^2 \tag{2.6}$$

and the total surface energy of the system is:

$$W(a) = \gamma_{LV}A_{LV} + \gamma_{SL}A_{SL} + \gamma_{SV}(A_T - A_{SL}) \qquad 2.7$$

where, as in Figure 1-1, the subscripts LV, SL, and SV denote the liquid – vapor, solid – liquid and solid – vapor interfaces, respectively. A_T represents the total area of the dielectric covered electrode and a describes the radius of droplet contact. A direct computation of the force per unit length along the contact line (i.e. the circle of intersection of the droplet, the surface and the surrounding vapor phases) yields:

$$f(a) = -\frac{1}{2\pi a}\frac{\partial W}{\partial a} \qquad 2.8$$

which can be simplified by substituting the geometrical factors from equations 2.2 – 2.4 and using equation 2.7. This yields:

$$f(a) = \gamma_{SV} - \gamma_{SL} - \gamma_{LV}cos\theta_Y \qquad 2.9$$

To arrive at Young's equation relating the surface energies at the three interfaces to the contact angle of the droplet, the equilibrium condition on the force causes $f = 0$, Rearranging yields:

$$cos\theta_Y = \frac{\gamma_{SV}-\gamma_{SL}}{\gamma_{LV}} \qquad 2.10$$

Now we can evaluate how an applied voltage affects the equilibrium condition we see from the basic static mechanical sessile droplet. Since the dielectric thickness is orders of magnitude less than the droplet radius, we can neglect the effects of fringe fields at the edge of the droplet. The conductive droplet resting on the dielectric layer on an electrode forms a capacitor system, with capacitance that is a function of the liquid contact area $A_{SL} = \pi a^2$ [72].

$$C(a) \approx \frac{\epsilon_d\epsilon_0 A_{SL}}{d} = \frac{\epsilon_d\epsilon_0\pi a^2}{d} \qquad 2.11$$

From Figure 2-1, we see that κ_d is the dielectric constant, d is the dielectric thickness, and ϵ_0 is the permittivity of free space. The next steps in the derivation from Jones [72] utilize the concept of coenergy for an energy conservative system and Legendre transform [73-74]. The full derivation is included in Appendix C. It leads to the electrical energy stored in a capacitor:

$$W_e(v,a) = \frac{1}{2}C(a)v^2 \tag{2.12}$$

Since the function is analytical, we can use equation 2.8 to write

$$f^e = \frac{1}{2\pi a}\frac{\partial W_e}{\partial a} \tag{2.13}$$

And holding a constant voltage, equation 2.13 can be expressed as

$$f^e = \frac{1}{2\pi a}\frac{v^2}{2}\frac{\mathrm{d}C}{\mathrm{d}a} \tag{2.14}$$

By taking the final derivative of capacitance with respect to droplet contact radius, the electrically induced force per unit length on the contact line is expressed as:

$$f^e = \frac{\epsilon_d\epsilon_0}{2d}v^2 \tag{2.15}$$

One aspect interesting to note is that the force acting on the contact line is not a function of the droplet area in contact, but only of the dielectric material and applied voltage. To arrive at the final Lippmann-Young equation governing contact angle change due to applied electric force, the two contact line forces are set in equilibrium $f^e = -f$.

$$cos\theta(v) = cos\theta^Y + \frac{\epsilon_d\epsilon_0}{2d\gamma_{LV}}v^2 \tag{2.16}$$

The initial contact angle from Young's equation is θ^Y while the final contact angle is $\theta(v)$. $\kappa_d\epsilon_0$ is the electric permittivity of the dielectric, d is the thickness of the dielectric, γ_{LV} is the interfacial energy between liquid an vapor phase, and v is the applied voltage. This is the Lippmann-Young equation that describes the relationship between droplet contact angle and applied voltage. This equation is valid even for two liquid electrowetting systems, in which the vapor medium is replaced by another liquid that is immiscible with the conductive droplet such as an oil. In this case, the interfacial energy between the two liquids replaces the γ_{LV} term from above.

The Lippmann-Young equation is valid for all electrowetting systems where contact angles remain above ~80°. However, a phenomenon known as contact angle saturation (CAS) limits the change in contact angle with increased applied voltage, causing the system to deviate from the equation. CAS and other limiting phenomenon of electrowetting are discussed in Section 2.1.3.

2.1.1 ***Limiting phenomenon***

At a small enough contact angle, all electrowetting experiments observe the onset of contact angle saturation (CAS). In CAS, the contact angle no longer decreases with further applied voltage, thus deviating from the Lippmann-Young equation. The electrowetting community as of June 2014 has not agreed upon a simple and unifying theoretical rationale behind the appearance of CAS [75].

Apart from CAS, there are also physical phenomena that limit the behavior of electrowetting. A summary of these challenges can be seen in [24] and [76].

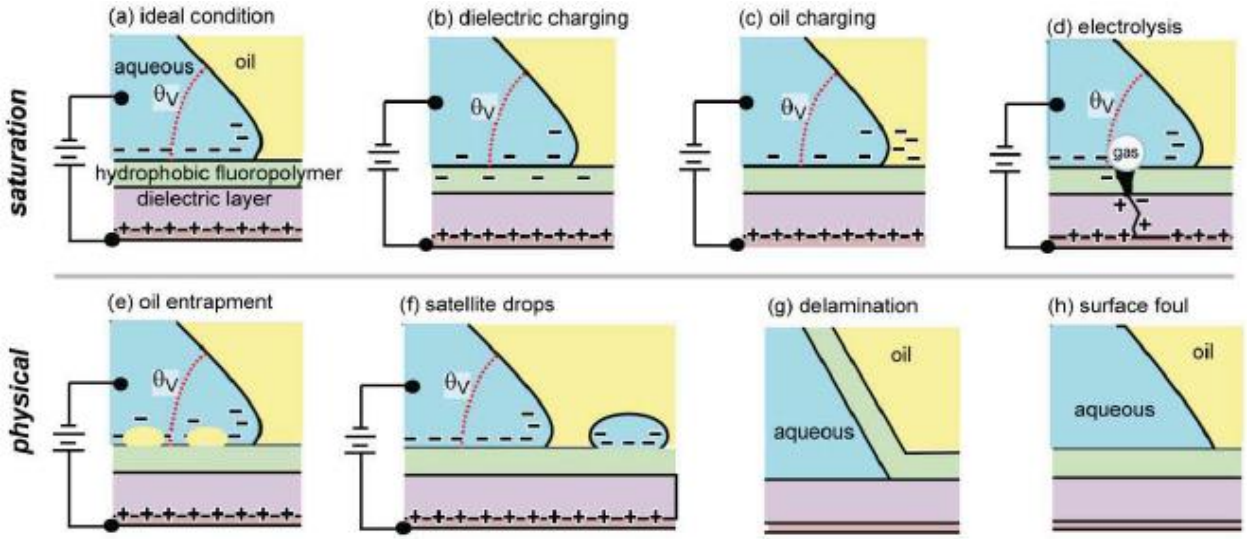

Figure 2-2 Examples of the challenges and limiting phenomena that occur in electrowetting systems. (a) Shows the ideal case for electrowetting before CAS onset. Potential sources for CAS include (b) dielectric charging and (c) oil charging, where these materials take charges from the electrowetting liquid and screen the electrowetting effect. (d) Depicts the case of breakdown resulting in electrolysis and device failure. Some physical limitations to electrowetting include (e) oil entrapment between electrowetting liquid and dielectric, conversely (f) satellite droplets expelled into the oil, (g) thin film delamination and (h) surface fouling of the dielectric / hydrophobic coating. Figure from [24].

As illustrated in Figure 2-2(b-d), a number of potential limitations have arisen, including dielectric charge trapping, oil phase charging and dielectric breakdown leading to electrolysis. Dielectric charging occurs when ions from the liquid become injected and trapped within the dielectric stack between conductive liquid and electrode. Accumulation of charge screens the charge at the liquid surface, thereby reducing the force present at the contact line. Charging typically occurs when a voltage has been held on the dielectric for an extended period or when a high voltage is applied that can drive the ions into the dielectric [77]. Oil charging can happen when impurities exist in the oil or if the conductive liquid is absorbed within the oil. Any charge at the oil surface will again screen the charge at the polar liquid surface, reducing the effect of the electrically driven force [76]. Finally, dielectric breakdown is the most detrimental of all electrically-induced limitations. Dielectric breakdown causes microshorts between droplet and electrode that causes electrolysis of the conductive liquid, forming gas bubbles and catastrophically

destroying the dielectric. With careful selection of dielectric materials and attention to design parameters such as dielectric thickness, ion source and liquid materials, these challenges can be mitigated.

There are also physical challenges that can arise in electrowetting systems, as seen in Figure 2-2(e-h). Oil can become trapped within the conductive droplet or satellite polar droplets can be expelled from the main part of the conductive liquid. In oil entrapment, we see an artificial increase in "dielectric" thickness in the areas covered by the oil. For satellite drops, we see another screening potential with the ions trapped on the droplets. Delamination of the top hydrophobic coating will lead to the droplet pinning to the underlying hydrophilic dielectric. Finally, surface fouling or defect sites can also cause pinning points for the polar droplet to stick to, causing distortion in the surface profile and contact angle hysteresis.

While these phenomena present a challenge for electrowetting systems, with careful consideration of the dielectric materials, the liquid combinations, ion choices and applied voltage, these problems can be successfully mitigated. The prevailing challenge remaining is CAS, for which a comprehensive description and model remains elusive.

2.2 **Electrowetting Lenses and Prisms**

The first liquid lens tuned by electrowetting was introduced at the turn of the millennium by Berge and Peseux [4]. They showed a repeatable lens tuning performance capable of adjusting its optical power over 60 diopters with the application of 220 volts. For comparison, the average optical power adjustment of the human eye is 15 diopters at 18 years of age and down to 4 diopters at 50 years of age [78]. The device design and optical tuning range can be seen in Figure 2-3.

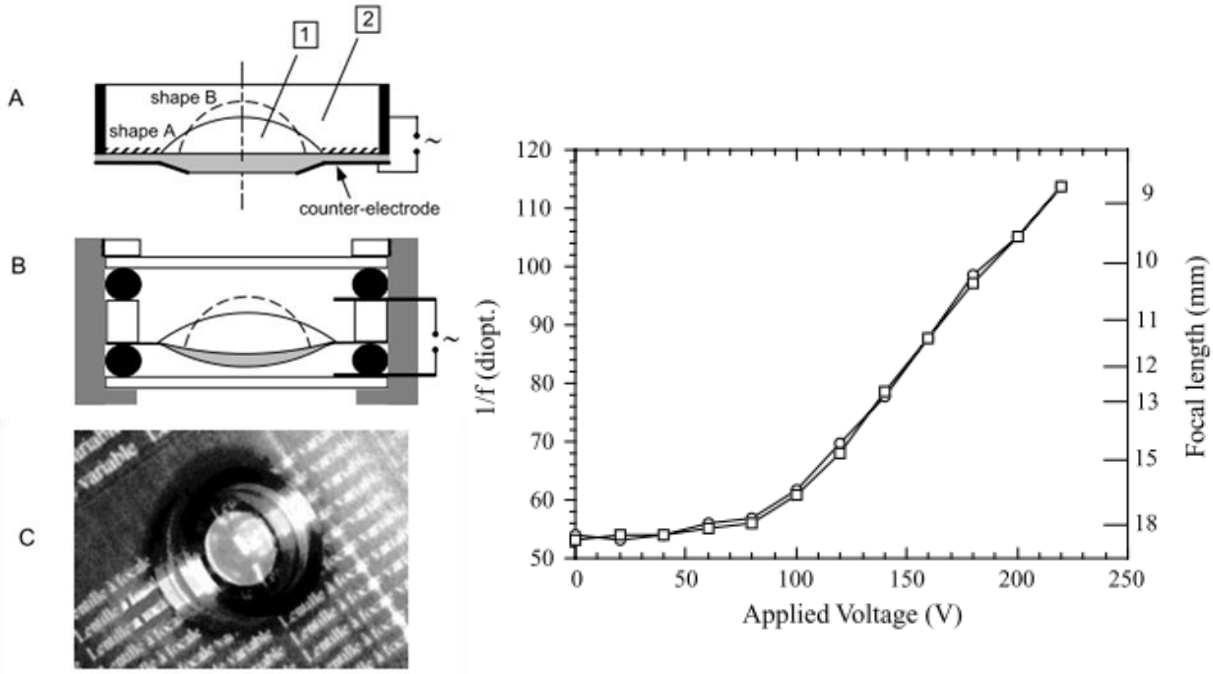

Figure 2-3 Electrowetting lens by Berge and Peseux. (A) Schematic of the system with [1] insulating, non-polar fluid surrounded by [2] sodium sulfate water solution. (B) Cell is sealed by o-rings with a central diameter of 5mm. (C) Photo of the entire device, with a 12mm stainless steel outer case. The device tunes its focal length from ~20 to ~9 mm with the application of just over 200V. Figure from [4].

This initial use of electrowetting-on-dielectric (EWOD) for a tunable lens device provides the foundation for liquid optics as a practical solution for non-mechanical adaptive optics. The next big stride in electrowetting lenses came from Kuiper and Hendriks [15], with the cylindrical glass tube lens. The big innovation was the deposition of electrodes on the inner vertical sidewall of a cylinder which holds the liquids, thus allowing the tuning lens to vary its curvature from convex to flat to concave with high enough voltages. Their device can be seen in Figure 2-4.

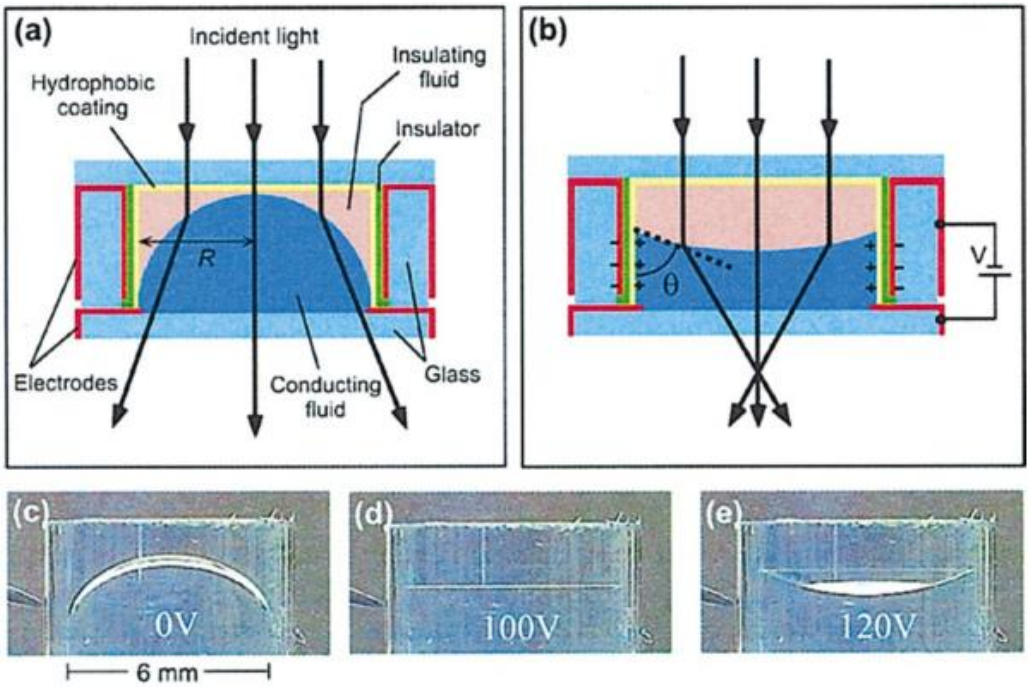

Figure 2-4 Cylindrical liquid lens developed by Philips' researchers Kuiper and Hendriks. Their design allows for both convex and concave liquid profiles, meaning a lens that can tune from diverging, to flat, to converging, covering a very large range of focal lengths. Figure from [15].

Kuiper and Hendriks' success defined their material system as a staple for future electrowetting investigations. The dielectric insulator used was Parylene-N and the hydrophobic coating is Dupont's Teflon AF1600. These materials (or variations of them) are used in the majority of electrowetting systems and studies to this day.

Next, Krogmann *et al.* demonstrated the microfabrication of a liquid lens cavity within a silicon chip [13]. The liquids are sealed within the cavity of the silicon layer between two glass slides that are anodically bonded to the silicon. The device is shown in Figure 2-5.

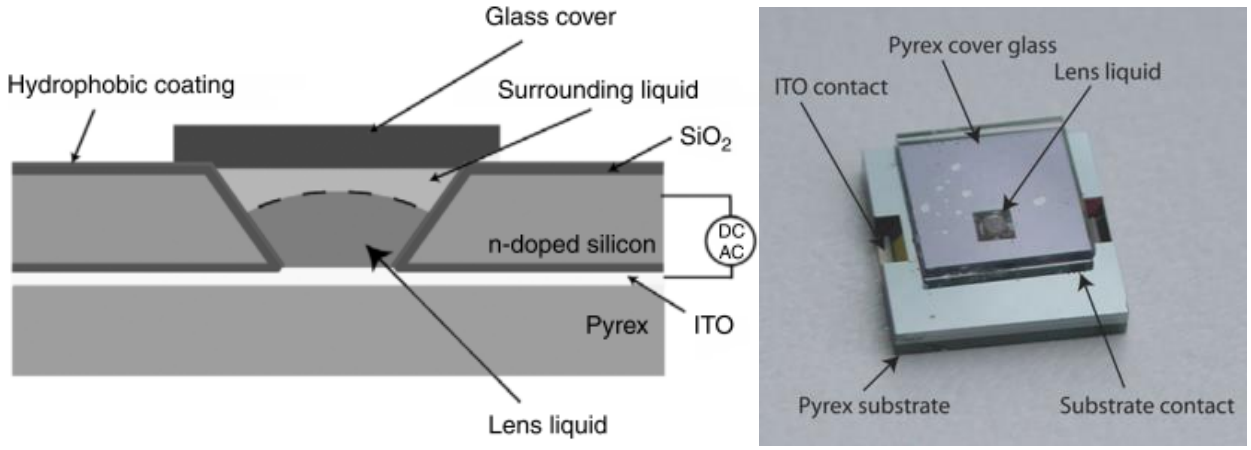

Figure 2-5 Three chip stack electrowetting lens developed by Krogmann et al. The liquid cavity is created by a KOH etch through the silicon. The dielectric is thermally grown silicon dioxide, known for its low defect count and low pinhole density compared to other types of silicon dioxide. The device is hermetically sealed by the anodic bonding process that seals the surfaces of silicon and glass together with high temperatures and electric fields that drive the alkali ions from the glass into the silicon. Figure from [13].

The device is an important step forward for electrowetting optics for two reasons: it miniaturized the lens down to 300 μm, showcasing the compactness of electrowetting technology. Secondly, the device was fabricated using standard microfabrication techniques, fully compatible with chip-scale mass production. However, the liquid cavity has square openings that are not ideal for optical apertures, as the liquid surface is distorted from a spherical shape at the square aperture. Despite this issue, the lens optical quality is good, comparable to conventional fixed glass microlenses [79]. Finally, the measured power consumption of the device was hundreds of μW, within the power capabilities of small, handheld commercial or medical devices. The device provides a nice demonstration of the compatibility of electrowetting variable optics with small, portable electronics on a scale of mass production.

Another important step is the introduction of multiple electrodes to enable more sophisticated electrowetting control. With multiple individually addressable electrodes, the liquid interface has more degrees of freedom and can assume the shape of not only a spherical cap, but also a flat surface to act as a prism with angle

depending on how the voltage is applied. This development began at the University of Cincinnati with Smith *et al.* [25] and was followed up by Hou *et al.* [11].

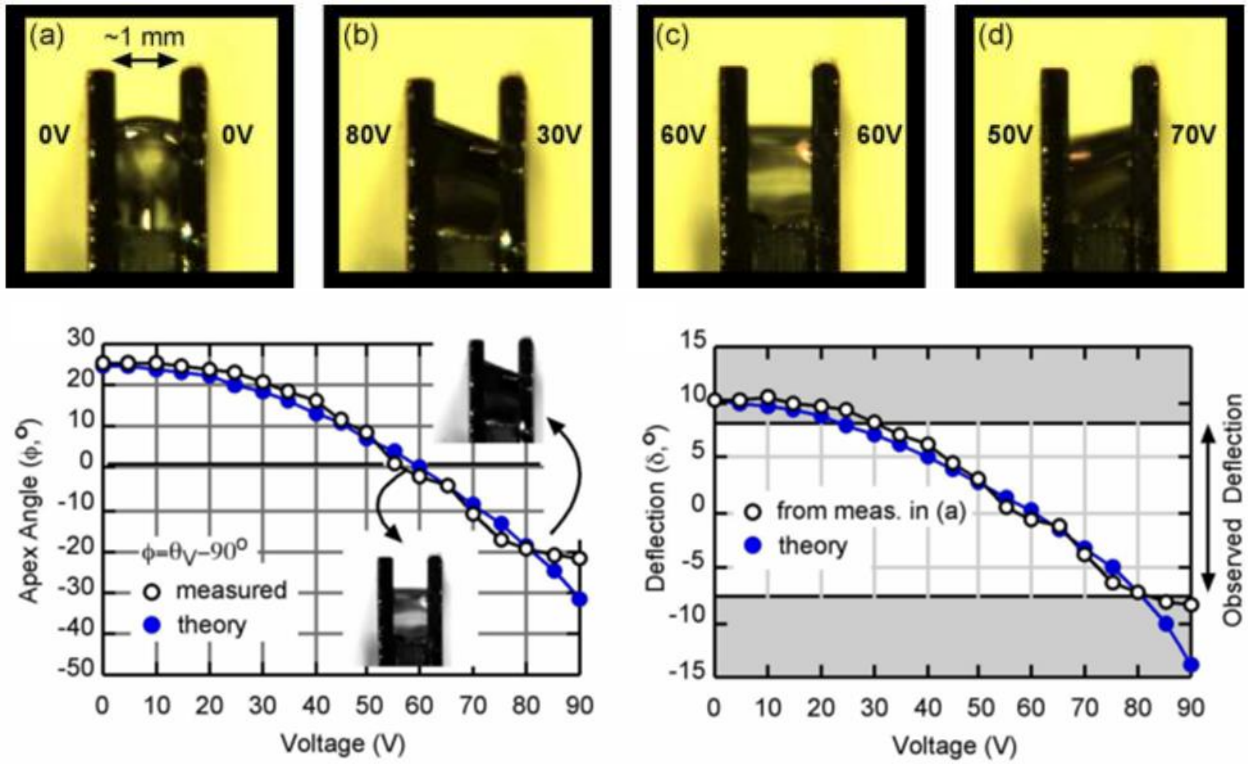

Figure 2-6 Electrowetting based prism device. Top: The electrowetting prism effect showing multiple modes of liquid tip-tilt achieved by addressing each sidewall with different voltages. Apex angles of +/- 25° yield beam deflection angles of +/- 7°. Figures from [25].

The first implementation of electrowetting prisms included only two sidewalls and appears as a trench prism capable of tilting on one axis. A beam steering device with no moving parts is very attractive for free space optical communications and laser detection and ranging [80]. The agility of liquid prisms can overcome the disadvantages associated with mechanical beam steering such as bulky size, slow speeds, and large power consumption. While advances have been made with decentered prisms [81] and optical phased arrays enabled by liquid crystal gratings [82], they still achieve wide angle steering by using multi-stage devices in cascade with difficult fabrication. Thus, developing an electrowetting based prism with simple fabrication and wide-angle deflection is an attractive alternative.

Continuing on this work, Hou *et al.* fabricated a macro-scale electrowetting prism by bonding 4 electrode covered prism sidewalls to make a prism device capable of tuning on a two axes, tip-tilt configuration [11]. By placing a 65 µm thick mirror on the surface of the water, the steering becomes geometrically dependent on the apex angle, as opposed to the smaller refracted angle, dependent on Snell's Law. Much wider beam steering angles are enabled, at the cost of the device being operated in reflection as opposed to transmission. The device by Hou *et al.* can be seen in Figure 2-7.

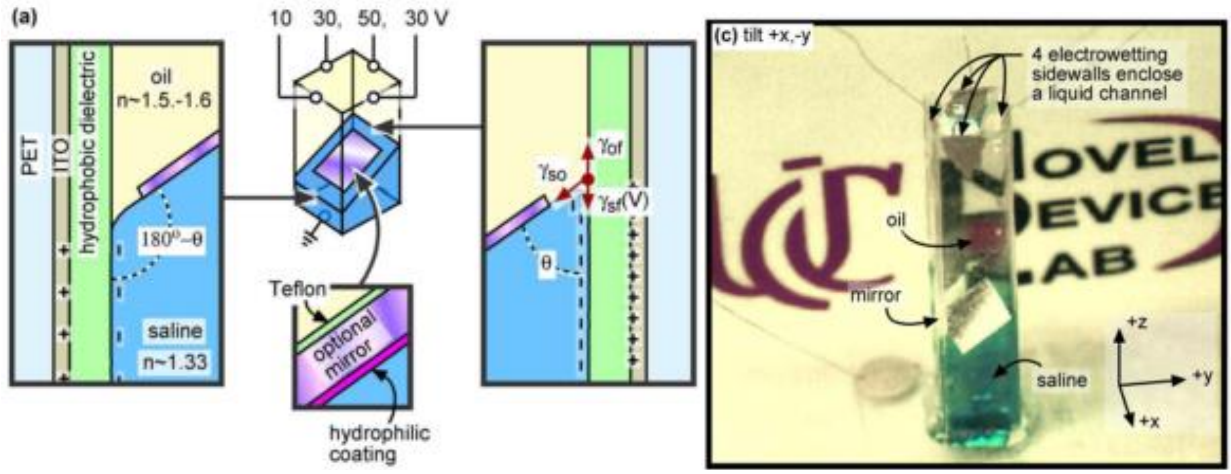

Figure 2-7 Improved prism device with floating mirror. This prism device contains four independently addressed electrodes, one on each sidewall. The additional electrodes allow the prism to tilt on two axes, giving greater control of the beam steering. Furthermore, the addition of a floating metal mirror at the liquid interface enables high beam steering angles (up to 20° in one direction) at the cost of operating in reflection rather than transmission. Figures from [11].

These initial proofs of concept for electrowetting prisms show great promise for the technology to evolve and find a role in the market of free-space optical communication. Increasing the aperture size of the prisms allows for more applications. Simple increase of the prism dimensions can introduce issues associated with density mismatch between liquids. At the small millimeter scale, surface tension forces dominate the liquids and the force of gravity and density mismatch do not affect the optical quality. As soon as the droplet size is increased beyond a few millimeters, the effects of gravity causes problems for orientation, as

liquids with unmatched densities will shift within the cavity due to the directional force of gravity. One approach to increasing the optical area without introducing the negative effects seen by large droplets is to fabricate arrays of small electrowetting optical elements.

Fabrication of an array of lenses is not a trivial task, particularly if the desire is to electrically address each lens in the array individually. Research on this endeavor started with Smith *et al.* and arrayed liquid lenses [23]. The liquid lens cavities are made from a photodefinable epoxy KMPR, and are 300μm in radius and 300 μm tall. The bottom of the substrate is metallized to make contact to the sputtered sidewall electrode and the top is sealed by a rubber gasket and a top-plate of indium tin oxide coated glass. This means that each lens is not indivudially addressable, and tuning occurs across the entire array simultaneously. This work was a great advancement for arrayed electrowetting optics, and was followed up with a review article coming from the same group in which the authors lay out the potential for arrayed electrowetting optics for laser radar, 3D displays, adaptive camoflage, electronic paper, retroreflector communication and microlens arrays [51]. The lens array operates at low voltage for electrowetting optics, tuning from -375 to +225 diopters with the application of 25V.

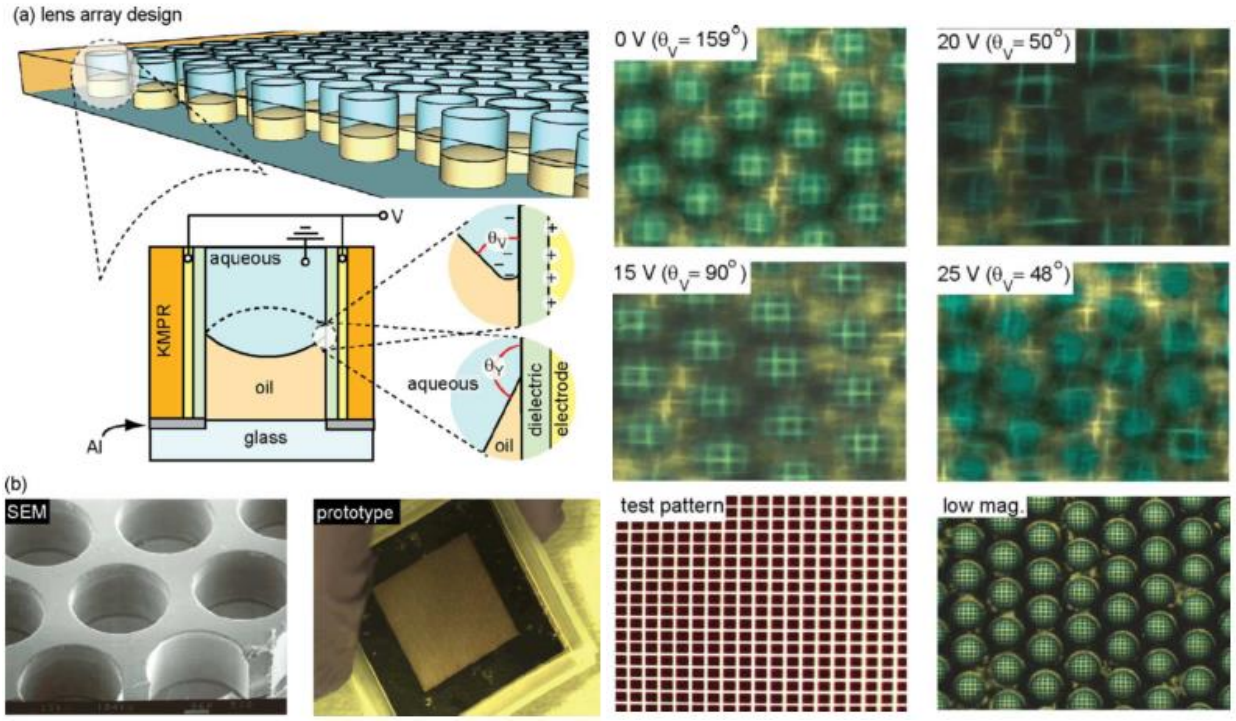

Figure 2-8 Designs and prototype of array liquid lenses. KMPR is used as the device layer material on top of a substrate with a thin film metal. Parylene-C is the dielectric and Fluoropel is used as the hydrophobic coating. The lens cavities are filled by self-oil dosing (described in [83]), in which the array is held vertically and slowly extracted from a container of water with an oil film resting on top. The lens array is tested with a cross hatch pattern. Figure from [23].

The logical next step was an array of liquid microprisms, which the same group demonstrated in 2010 [10]. The paper shows the basic of microprism array functionality without individual addressability, as the main purpose is to lay out a scalable fabrication process for developing arrayed electrowetting optics. The work done in [10] was a great advancement in addressing the challenges of manufacturing these arrayed electrowetting devices. Combined with the display technology's knowledge of active matrix transistor control over pixel elements, a new breakthrough in this technology is in sight for the very near future.

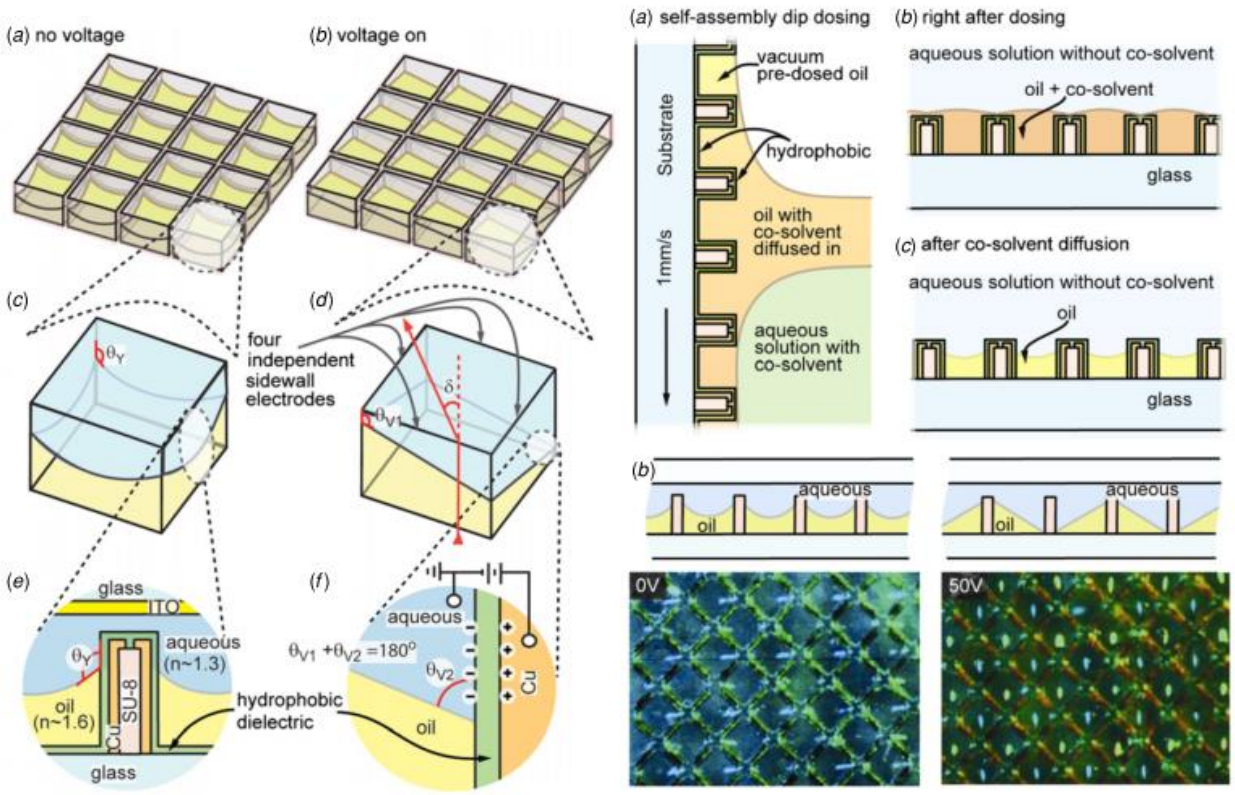

Figure 2-9 An array of 150 µm square prism cavities is patterned in SU-8. The electrodes for each lens are created by sputtered copper and covered with Parylene C and Cytonix Fluoropel 1601 V. To fill the liquids, the devices use tetradecane oil. The array was then dipped filled with an aqueous solution. The prototype prism array as demonstrated to image blue and yellow off-axis LEDs. Figure from [10].

In 2011, Kuiper used a similar liquid lens device previously developed in [15] for an endoscope application [16]. The outer diameter of the lens is 5 mm and the endoscope outer diameter is 7 mm. The system is capable of focusing on objects at a range from 100 mm down to 5 mm away. The endoscope device and sample images taken with it can be seen in Figure 2-10.

This work proved the applicability of liquid lenses for medical devices and further established electrowetting optics as a legitimate technology for realizing variable optical devices. Kuiper also addresses the challenges of making close-up images in endoscopes. With narrow diameter requirements, it becomes difficult to use conventional mechanical systems with actuators to move lenses for variable focus optics. The added bulk of mechanical systems poses a challenge in the axial

dimension, as a large displacement length is needed to cover the focal depth seen in endoscope [16]. Not only are electrowetting lenses applicable to endoscopy, with their small dimensions and lack of moving parts, they are better suited to the job.

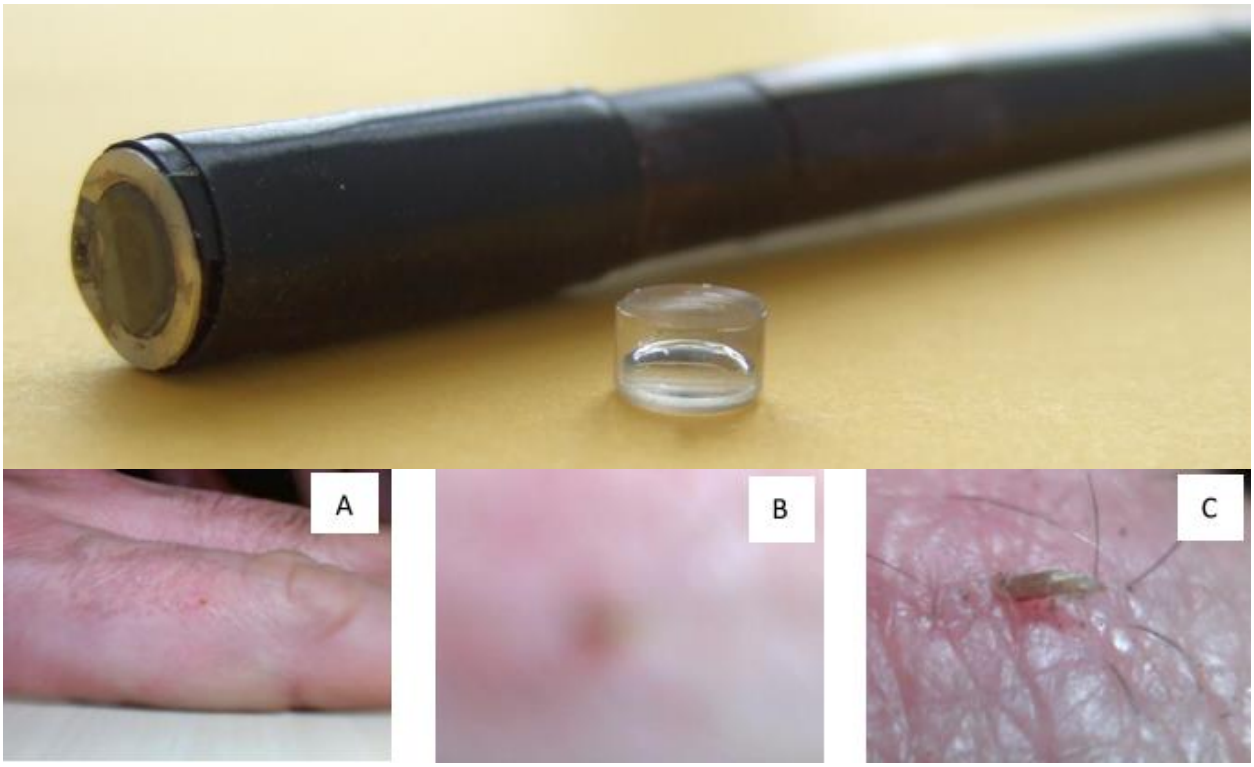

Figure 2-10 The liquid lens based endoscope. Endoscope device is shown with a separate liquid lens for comparison. (A) A small lesion is imaged at 10cm, (B) the lesion shown at 0.5cm without adjusting the liquid lens, and (C) at 0.5cm after tuning the liquid lens. Figure from [16].

Another application for electrowetting variable optics was demonstrated in 2011. An electrowetting macro-prism was developed for tracking the motion of the sun to guide light onto a solar cell [6]. Cheng and Chen fabricated a 10 mm x 10 mm rectangular prism by sealing 4 sidewalls with epoxy and individually addressing each wall. The scale of this rectangular prism is large enough that gravitational forces on the liquid begin to alter the surface profile, causing a sagging effect. Also, the liquid's density mismatch at this length scale means the device is only operable in an upright fashion. Nevertheless, the application of the electrowetting prism is what's important for this device. Since the prism is controlled completely

electronically, a simple feedback system could be included to allow a sun tracking electrowetting prism adjust its tilt angle dynamically for maximum solar collection.

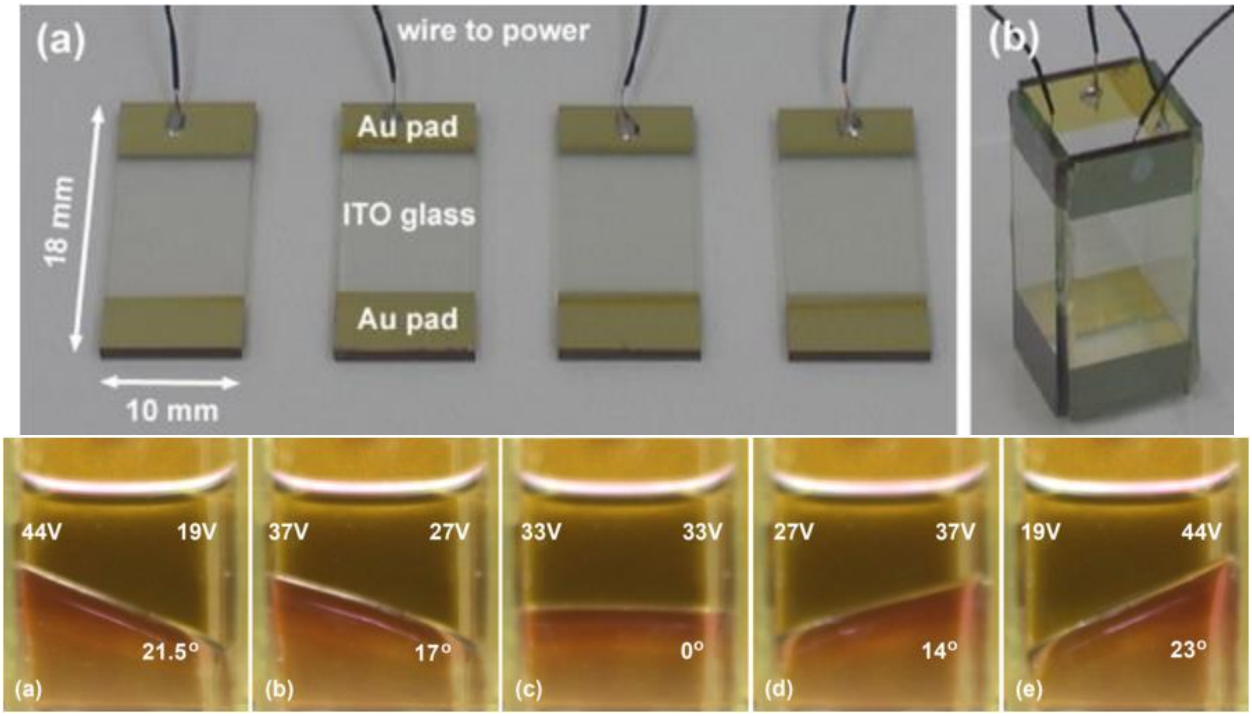

Figure 2-11 Adaptive electrowetting prism for sun tracking with a solar cell. The large scale of the prism puts it into a macro-prism regime, where gravitational effects will begin to alter the liquids' shapes. Figure from [6].

The most recent advancement for arrayed electrowetting prisms shows drastic improvement to the state of arrayed electrowetting optics. Kwon *et al.* demonstrated an array of 200μm square pixels with 4 separate sidewall electrodes and individual addressability for each pixel [17]. Figure 2-12 shows close up scanning electron microscope images of the individually addressable prism array. The sidewall device material is a photodefinable epoxy and the sidewall metallization is done with an electroplating process to enable the high aspect ratio.

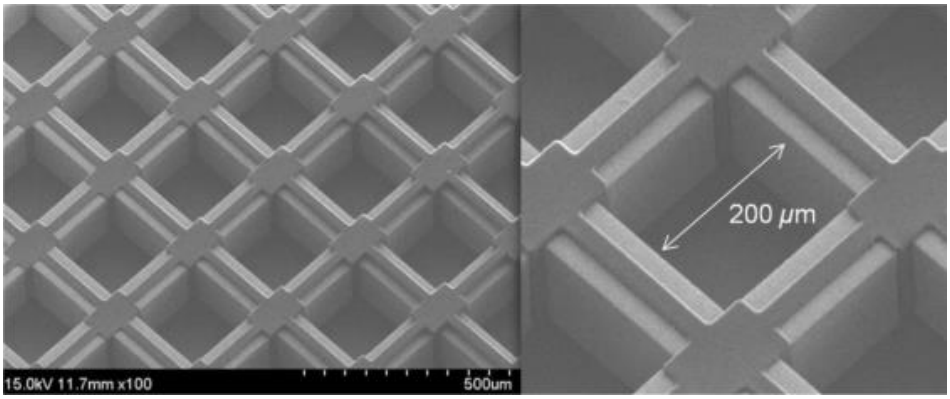

Figure 2-12 SEM image of arrayed electrowetting microprisms. The light grey is metal that was electroplated up through a thick photoresist. The dark grey is an insulating photoresist. The bottom substrate has many tightly packed electrodes that can individually address each pixel element and separate sidewall. Figure from [17].

The prism array depicted in Figure 2-12 looks highly pristine and has a decent fill factor when considering the fact that each of the four sidewalls has independent voltage control. In the same paper, the authors demonstrate what looks to be a slightly modified version of the device from above. See Figure 2-13 for the prism array device that was demonstrated in the article.

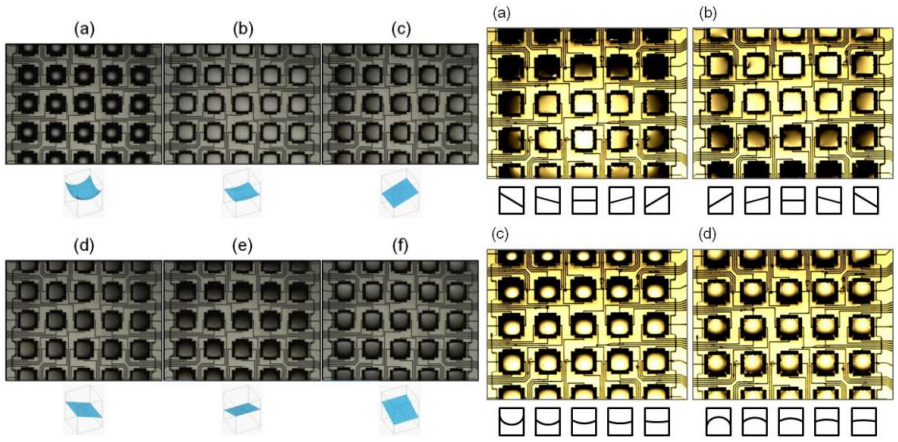

Figure 2-13 Electrowetting microprism array in action. Left: the common sidewalls for each pixel are electrically connected, realizing an array that can tune its angle simultaneously. Right: each pixel's sidewalls are addressed separately, enabling variable beam angles on a pixel by pixel basis. Each element can achieve convex or concave liquid profiles, and the reported prism angle is +/- 30° for each axis. Figure from [17].

This level of control for individual electrowetting elements is unprecedented. It demonstrates an array of microprism elements with tip-tilt control as well as the possibility for lens control, depending on how the voltage is applied to the four

electrodes for each element. While the need for many fanned out electrodes decreases the fill factor which directly affects the efficiency of the device when used in transmission, it still nevertheless displays a high level of optical agility in a small package. It shows that by using the fabrication techniques laid out in [10] and [17], arrayed electrowetting optics is fast becoming a commercially viable product.

Presently, the company Varioptic founded by Berge in 2002 has several electrowetting based liquid lens products commercially available. They report large range of focusing and high optical quality independent of the aperture size [84]. Wavefront error is the biggest cause of image distortion for any liquid lens, and Berge *et al.* report numbers down to approximately 1/15 of a wavelength, or roughly 40 nm, showing that the lens quality of electrowetting optics allows for high quality applications.

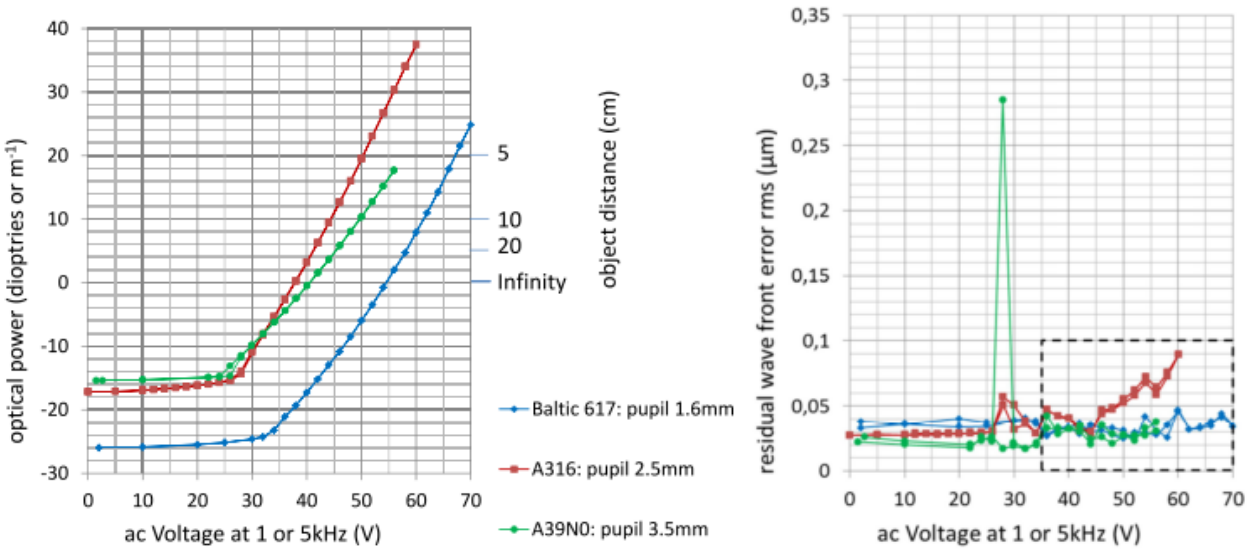

Figure 2-14 Commercially available electrowetting lens devices. Baltic 617, Arctic 316 and A39N0 from Varioptic. Outer package diameter for Baltic 617 and Arctic 316 are 7.5 mm, while A39N0 has outer diameter of 13 mm. Measured residual wave front error is around 40 nm. Figure from [84].

The development of electrowetting optics has steadily increased in the last decade as more effort is put into studying the materials to enable reliability and longevity of these devices for practical implementation. A common thread in the

research for electrowetting lenses and prisms is that to achieve the large tuning ranges enabled by the devices, high voltages (on the order of 40 V and above) must be applied which leads to challenging integration with miniaturized devices, which is where the advantages lie with electrowetting liquid optics. This voltage limit has been due to the need for thick dielectric films in order to prevent ion infiltration. Another area that these optical devices have been limited is in the operable wavelength. Electrowetting devices based on aqueous polar materials are limited to wavelengths below 1,450 nm due to the absorption characteristics of water. The details of electrowetting lens design are covered in Section 2.3.

2.3 **Electrowetting Lens Design Parameters**

There are several aspects of a lens design that affect key performance metrics such as contact angle range, lens power, voltage requirements, hysteresis, and failure point. Examining the Lippmann-Young electrowetting equation (2.19), we see the obvious factors that determine change in contact angle which is linked to lens focal length by equation (2.20). These factors include the initial contact angle, dielectric permittivity, dielectric thickness, and interfacial energy between electrowetting liquid and non-polar liquid.

2.3.1 ***Electrical constraints***

To minimize required voltage, it is desirable to have a high dielectric constant material be as thin as possible and use an electrowetting liquid system which minimizes interfacial energy between polar and non-polar fluid states. One design constraint that is evident from this approach is that at some critical thickness, the voltage across the dielectric that induces electrowetting will cause an electric field that exceeds the dielectric strength of the material, causing electrical breakdown. This breakdown allows electrical conductivity leading to shorting, and current

spikes that causes electrolysis in the liquids and burning of the materials, consistent with device failure.

Minimizing dielectric thickness with high-k dielectrics can be great for reducing electrowetting voltage [85], but introduces further design considerations. Capacitance of the system is directly related to dielectric constant and inversely related to the thickness. A high capacitance system helps reduce the voltage requirement of electrowetting, yet has another effect on the system dynamics. Since the electrowetting liquid has a resistivity dependent on the frequency of applied voltage, the droplet and dielectric device can be modeled as an RC series circuit.

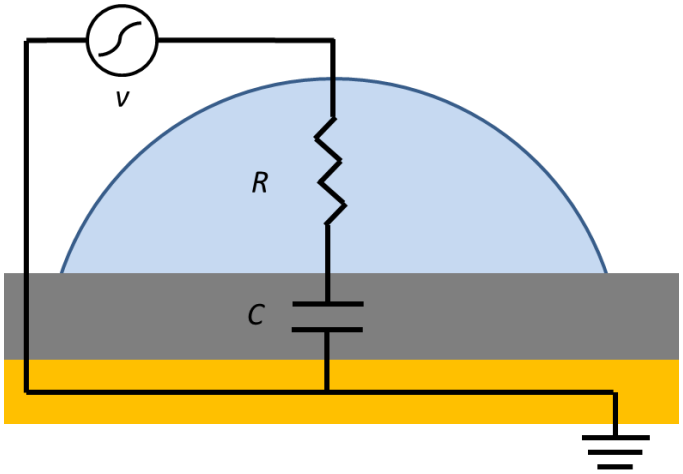

Figure 2-15 Basic AC circuit model electrowetting systems. Shows the RC circuit components in series which leads to transient charge time dependent on values of resistance R and capacitance C.

An RC circuit in series has an associated charge time constant, $\tau = RC$. The transient voltage a capacitor is given by the following [86]:

$$V(t) = V_0(1 - e^{-\frac{t}{\tau}}) \qquad 2.17$$

Where V_0 is the applied potential, t is time. This becomes important because if the capacitance is very high and the resistivity of the liquid causes high resistance, the time to reach peak charge on the device can increase drastically. This can affect the response time of the droplet if the values of τ begin to approach the time scale of

the droplet's hydrodynamic response, which is typically limited to tens and hundreds of milliseconds [70].

2.3.2 Material considerations

As stated in the previous section, a thinner film dielectric has a lower voltage requirement. The challenge is ensuring that the thin film dielectric remains quasi pinhole free, such that the leakage current is never large enough to cascade into microshorting that leads to device failure by electrolysis [27], [87]. A thin film deposition technique known as Atomic Layer Deposition (ALD) can enable extremely pristine and pinhole free conformal coatings at ultra-thin device layers. ALD based dielectrics have been successful in electrowetting studies [51], [85] due to its pinhole free nature. Its potential as a barrier layers to prevent ion transport through electrowetting dielectrics with preliminary data was briefly studied and merits a full investigation. This work can be seen in Section 6.2.3. A summary of successful electrowetting dielectrics and hydrophobic coatings is listed in Table 2.1.

Table 2.1 Properties of dielectrics and hydrophobic coatings for electrowetting applications. Values for parylene from [106], Al_2O_3 and HFO_2 from [141], SiO_2 from [142], Teflon from [143], Fluoropel from [144] and CYTOP from [145].

Dielectric	Hydrophobic	Deposition processes	Dielectric Constant	Dielectric Strength (MV/m)
SiO_2	N	ALD, Thermal	3.9	600-1000
Al_2O_3	N	ALD	10.3	694.9
HfO_2	N	ALD	18.7	548.4
Parylene-N	N	Vapor phase	2.65	275.6
Parylene-C	N	Vapor phase	3.1	220.5
Parylene-HT	N	Vapor phase	2.2	212.6
Teflon AF 1600	Y	Dip coat	1.93	21
Cytonix Fluoropel	Y	Dip coat	2.25	100
CYTOP	Y	Dip coat	2.1	100

Surface roughness of the substrate plays an important role in the wetting state of the droplet. Droplet wetting to a rough surface is not a trivial study, as different degrees of roughness can cause different wetting states. To further complicate things, there are cases of roughness that allow pockets of air (or whatever ambient fluid) to hold the electrowetting liquid and prevent total wetting, known as Cassie-Baxter mode wetting. Roughness of substrates like silicon and glass is very low (on the order of nanometers) and has negligible effect on the droplet hysteresis. But roughness on the order of tens of micrometers begins to affect the wetting performance of droplets, causing transition from Cassie-Baxter wetting to Wenzel mode wetting, where liquid infiltrates the microstructures and can become pinned, as seen in microstructured surfaces [70]. A study on hierarchical surface roughness by Lee and Kim [88] provides a good review of how roughness at different levels (i.e. nanostructured and microstructured) can affect the wetting and hydrophobicity of the surface. Suffice to say that engineering the surface with micro- and nano-structures is a great way to enable superhydrophobic coatings that eliminated hysteresis and droplet pinning.

Liquid material selection also has many effects on the lens system. The initial contact angle is dependent on the balance of interfacial energies between each phase in the system. Maillard *et al.* [89] investigate the effects that surface energy matching between these three phases has on initial contact angle and hysteresis. By matching the surface energy of the non-polar liquid to the surface energy of the substrate, higher initial contact angles can be realized. Furthermore, this also has the effect of mitigating hysteresis in the contact angles. As displayed in [89], matching these surface energies is a challenge, due to the various polar and dispersion components of the three surface phases in the system.

Apart from the interfacial energies of the liquids, one must also consider the densities of the liquids. For Bond numbers << 1, i.e. systems small enough where

surface energy forces dominated over gravitational forces, liquid density mismatch is not a challenge. However, when the forces of gravity begin to be near the same order as the surface tensions, such as for droplet of greater than 1 mm diameter [70], differences in density can adversely affect the system. Mismatched liquids can shift around within the lens or prism cavity, depending on device orientation. The liquid interface that forms the lens can also begin to sag under the effects of gravity, causing distortion in the image. Modeling has shown that even with larger droplet sizes of 2 mm diameter, the effect of gravity on liquid lenses made from density matched water and oil is negligible, causing only λ/50 deviations from a spherical surface profile [7].

A large majority of electrowetting experiments use water as the polar liquid and dissolve various ion sources to increase the conductivity. However, there are several reasons why electrowetting is limited by this selection, including its small molecular size, leading to permeation through dielectrics and its absorption of light above 1.4 μm wavelength. Table 2.2 shows a comparison of 8 non-aqueous electrowetting liquids that have been studied in [90], with additional properties from [91] and [92].

The conductivity listed is the native conductivity of the liquid without any ion source added (except water, which is reported with its 1 wt% SDS solution conductivity). Tetrabutylammonium bromide (TBAB) and sodium dodecyl sulfate (SDS) are ion sources that are added to the liquids to achieve a conductivity of 20 μS/cm. This conductivity figure was determined by Chevalliot *et al.* as being optimal for ion transport for successful electrowetting and liquid resistance for the RC charging [90]. The interfacial energy figure is measured with pendent drop method between the electrowetting liquid and a blend of silicone oils from Dow Corning: 80 wt% OS-20, 10 wt% OS-10 and 10 wt% OS-30. The contact angle comes from

measurements on 1 μm parylene-C and 50 nm of Cytonix Fluoropel with the electrowetting fluid submerged within the silicone oil blend.

Table 2.2 Properties of non-aqueous electrowetting liquids. σ is the conductivity, TBAB is Tetrabutylammonium bromide, SDS is sodium dodecyl sulfate, γ is the interfacial tension with silicone oil blend, and CA is contact angle. Properties from [90-92]

Liquid	σ μS/cm	TBAB wt%	SDS wt%	γ_{LV} mN/M	CA at +30 V	CA at -30 V	CA at 30 V_{rms}	Melt. pt. °C	Boil. pt. °C
Water	877	-	1	6	58 ±1°	55 ±1°	69 ±2°	-	-
Propylene glycol	~0	0.305	0.372	8.5	65 ±1°	66 ±2°	90 ±1°	-60	187.6
Propylene carbonate	5.3	0.027	0.039	8.6	57 ±1°	80 ±2°	91 ±3°	-48.8	242
2-pyrrolidone	4.6	0.086	0.135	7.8	59 ±1°	75 ±4°	82 ±4°	25	251
γ-butyrolactone	0.84	0.016	0.033	7.0	58 ±1°	74 ±4°	78 ±2°	-43.3	204
Formamide	1500	-	-	23.8	115±2°	120±1°	121 ±2°	2.6	220
N-methyl formamide	160	-	-	6.8	62 ±4°	88°	76 ±2°	-3.8	199.5
Ethylene glycol	0.03	0.072	-	15.6	93 ±2°	99 ±1°	113 ±2°	-1	197.3
DMSO	0.62	0.018	0.026	8.5	64 ±1°	84 ±3°	97 ±3°	18.5	189

*2.3.3 **Optical parameters***

By containing the immiscible liquids within a cylindrical cavity, a lens is realized at the liquid boundary. The curvature of the liquid surface changes as a result of energy minimization for the new contact angle induced by the electrowetting effect. Electrically tuning this surface provides the basis for electrowetting optical devices that alter curvature or tip-tilt with no moving parts. The circular liquid lens formed within a cylindrical cavity has an optical power estimated by using the thin lens approximation [93]:

$$D = \frac{1}{f} = \frac{1}{r}\left(\frac{n_1}{n_2} - 1\right) = \frac{-cos(\theta)}{R} \cdot \left(\frac{n_1}{n_2} - 1\right) \qquad 2.18$$

where D is optical power in diopters [1/m], f is focal length, r is radius of curvature of the conductive liquid, n_1 and n_2 are the refractive indices of the ambient fluid and the polar liquid, respectively, and R is the radius of the lens. Inspecting equation 2.20 reveals a few things about the optical parameters. The radius of curvature is directly related to the focal length, meaning that a smaller radius of curvature provides a shorter focal length. The minimum radius of curvature is equal to the radius of the lens R and occurs in the case of the maximum contact angle of 180°. Also, as the contact angle is tuned to 90° representing a flat surface, the focal length approaches infinity. Thus, the larger initial contact angle results in a larger tuning range of the focal length.

The other factor that distinctly controls the optical power of the system is the ratio of refractive indices between the two liquids within the system. It is desirable to have this ratio be as far from 1 as possible, meaning a high contrast of refractive index between the two liquids. This translates to a stronger weighting factor on the optical power of the lens for a given contact angle, and is ultimately responsible for the effective range of optical power in the variable lens system. For liquid prism systems, this ratio factor is also what determines the amount of steering the incident beam undergoes through refraction at the liquid interface.

Another important optical parameter of the liquid lenses is the transmission across a spectrum of desirable wavelengths. Transmittance of light through a material with uniform attenuation follows Beer-Lambert Law [94]:

$$T = e^{-\alpha l} \tag{2.19}$$

where T is the transmittance parameter which describes the fraction of light flux that passes through the material, α is the attenuation coefficient that depends on the material, and l is the path length through the material. So maximizing transmittance is achieved by minimizing the path length the light has to pass

through any material. This becomes an important design consideration when investigating wavelengths of operation where absorption becomes a challenge. This is particularly evident at wavelengths beyond the visible into the infrared. The vibrational modes of the small molecules in most solvents and oils cause heavy absorption, limiting device transmittance though thicker liquid path lengths [95].

2.3.4 Electrowetting thin film model

With these design constraints in mind, I developed A MATLAB model was order to optimize the dielectrics to achieve the lowest voltage electrowetting without encountering electric breakdown of the dielectric or hydrophobic layers. This model can also be used to predict the contact angle performance of an electrowetting system before the onset of contact angle saturation. Figure 2-16 shows a screenshot of the graphical user interface that accepted the input parameters for the electrowetting system.

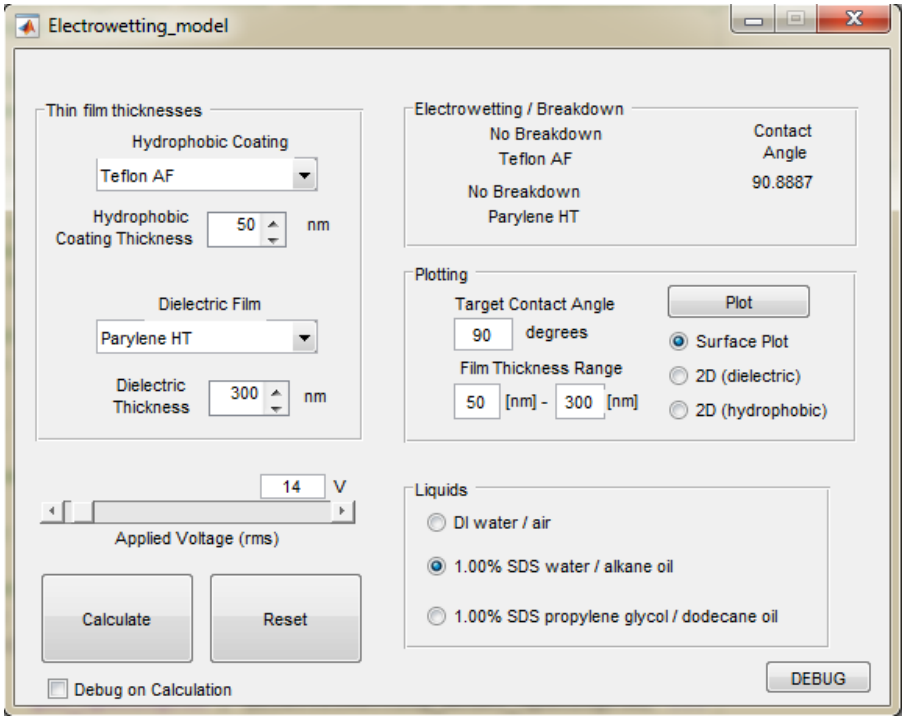

Figure 2-16 Electrowetting model GUI based in MATLAB. Input parameters include dielectric and hydrophobic coating type and thickness, applied voltage, a selection of liquids with known interfacial energy, and a target contact angle. The program outputs the optimized thicknesses for each to minimize voltage and remain above the breakdown threshold.

A more complete circuit model for the electrowetting droplet scheme is depicted in Figure 2-17.

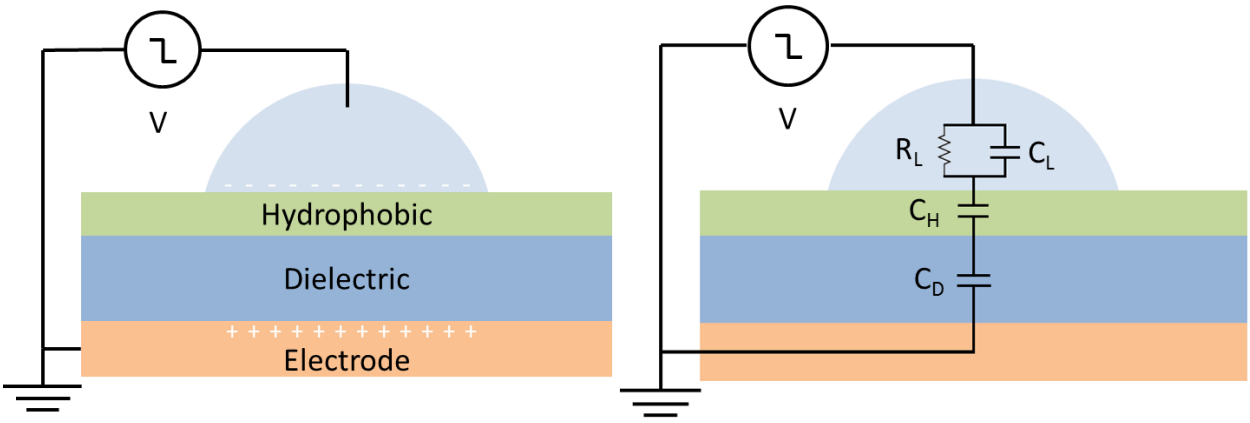

Figure 2-17 Electrowetting circuit model. Left: generic electrowetting droplet scheme. Right: circuit model depicting the basic components used when modeling electrowetting response. V is the applied AC voltage, R_L and C_L correspond to the liquid resistance and capacitance, C_H is the capacitance of the hydrophobic layer and C_D is the capacitance of the dielectric layer.

Since the two films needed for successful reversible electrowetting (i.e. dielectric and hydrophobic coating) are insulating and ideally pinhole free, they are modeled as capacitors in series. Thus, when incorporating the Young-Lippmann equation, the $\frac{\epsilon}{d}$ must be calculated as an effective specific capacitance, by adding the specific capacitances in series:

$$c_{eff} = \frac{c_H \cdot c_D}{(c_H + c_D)} \qquad 2.20$$

Where c_H and c_D are the specific capacitances of the hydrophobic coating and dielectric, respectively. The next step in modeling the stack for breakdown is to determine how much voltage drops across each capacitor with a known total voltage applied for any given thickness and dielectric material properties. Using a capacitive voltage divider the voltage drop across each thin film can be calculated as follows:

$$V_H = V \cdot \frac{c_D}{c_H + c_D} \qquad 2.21$$

$$V_D = V \cdot \frac{c_H}{c_H + c_D} \qquad 2.22$$

where V_H and V_D are the voltage drops across hydrophobic and dielectric layers, respectively, and V is the applied peak voltage. Knowing the voltage drops and the thickness of each layer, the total electric field strength can be calculated. This is used to determine whether the electric field is below the threshold of the material's dielectric strength. An example of the model output surface plot is shown in .

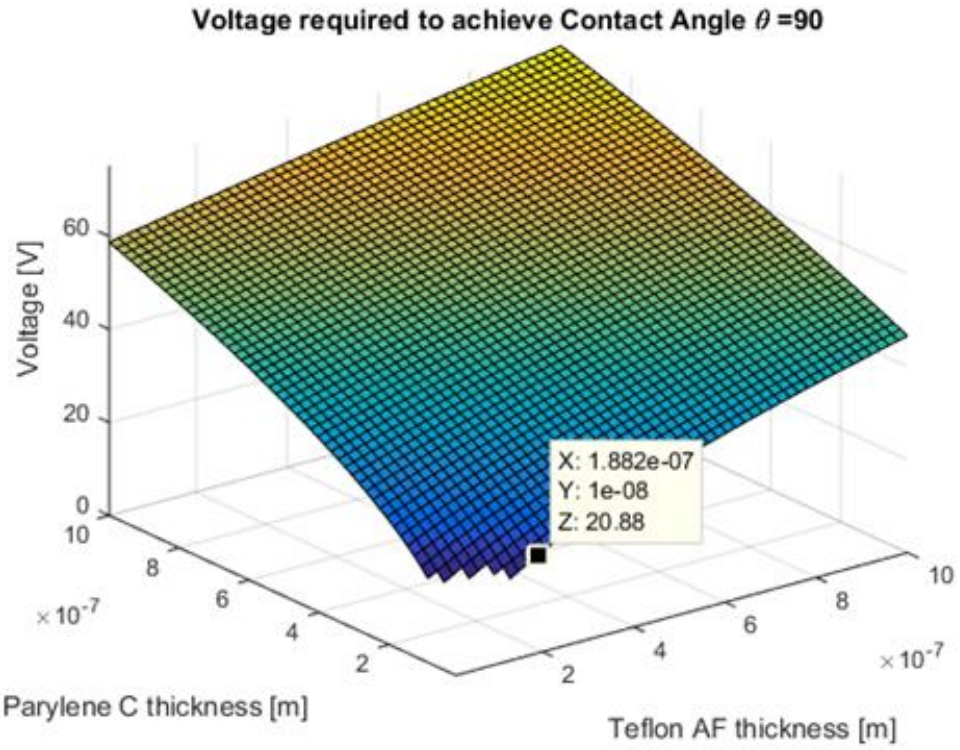

Figure 2-18 Surface plot of optimizing thin films. The x and y axis show thickness of parylene-C and Teflon AF while the z axis depicts the voltage required to change the liquid contact angle to the input threshold of 90°. The area near ultra-thin parylene-C and Teflon results in electrical breakdown, so these plot rejects these data points.

The modeling effort is important to corroborate the experimental measurements and to predict successful electrowetting. However, the limiting phenomenon of electrowetting such as charge trapping, ambient fluid ionization, leakage current, fractional dielectric strength due to thin film defects and contact angle saturation

cannot be predicted using this model, as it only accounts for the basic Young-Lippmann contact angle change and ideal dielectric breakdown in thin film stacks.

With a good understanding of the design parameters, liquid lens technology can begin to be engineered. These design considerations play a large factor in the devices developed in this dissertation. In the next chapter, I will detail the work I have done in my studies of electrowetting based liquid lenses to enable low voltage lens operation. The use of high quality thin film dielectrics and proper ion selection are keys to enabling reliable lens operation with low power consumption. Furthermore, I demonstrate liquid lenses based on non-aqueous polar liquids that can extend the wavelength of operation into the infrared, as discussed in Chapter V.

CHAPTER III – ELECTROWETTING LIQUID LENSES

This work was performed in collaboration with Robert Niederriter, in the beginning, followed by help from Soraya Terrab and Kevin Dease. The work was a collaborative effort between Professors Victor Bright, Juliet Gopinath (department of Electrical, Computer and Energy Engineering) Carol Cogswell and Robert Cormack, and resulted in publication [21], [26-27]. We are grateful to Professor Robert McLeod for his assistance with lens quality measurements and to Chris Roath with VSI Parylene for his assistance with the thin film dielectrics.

When I began working on this project in 2011, my goal was to fabricate an array of lenses to demonstrate individually addressable elements as well as study the thin film dielectrics and liquid materials to help minimize the voltage requirements for electrowetting optics. Reducing the voltage to 15 V or below was a good target, as it would be compatible with thin film transistor technology as seen in displays or other arrayed electrowetting systems [51].

This chapter details the development of the electrowetting lens array from Niederriter *et al.* [21], including the design, fabrication, characterization and application to curvature and phase tuning in Section 3.1. The remaining sections detail the work done in Watson *et al.* [27], including the lens redesign, material selection, lens fabrication, and optical characterization for water-based and non-aqueous liquid lenses.

3.1 **Liquid Lens Array for Curvature and Phase Compensation**

The initial electrowetting demonstration in the Bright MEMS group at the University of Colorado was completed by Yuan-Jen "Richard" Chang [5]. In his paper, he developed an electrowetting lens device in a thick layer of photodefinable epoxy spun coated on a glass substrate. Since the SU-8 epoxy acts as a negative resist, he was able to expose from the backside and develop a positive taper in the defined lens cavity, seen in Figure 3-1.

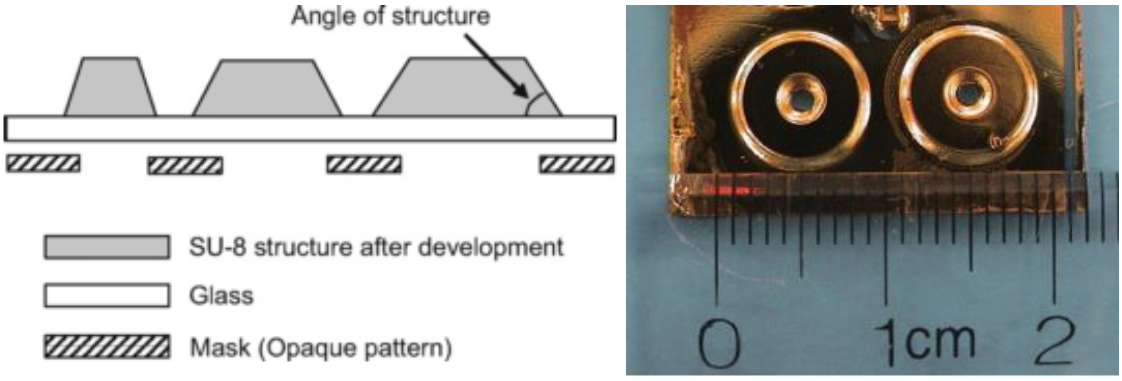

Figure 3-1 Initial electrowetting lens devices from the Colorado group. Backside exposure causes a positive taper to develop in SU-8, a normally negative tapered resist. By playing with the over exposure dose, the taper angle can be engineered. The taper can be seen as the light rings around the outside and inside of the SU-8 microlens cavities. Figure from [5].

Since absorbed UV light causes the SU-8 to cross-link and remain after development, the backside exposure means the SU-8 closest to the substrate would absorb more light and the cross-linking polymer would diffuse further around the defined pattern. With normal exposure doses typically needed for SU-8 cross-linking, this extra absorption and lateral diffusion to the top layer of resist would amount to ~µm scale pattern swelling. However, Richard Chang purposely over-exposed the SU-8 to fabricate the tapered sidewall. This enabled the electrode and dielectric deposition to coat the sidewall of the lens cavity.

Continuing the lens development, Keith Cobry designed a one dimensional array. The design, seen in Figure 3-2, followed and expanded upon the device from Krogmann [13]. Instead of a single lens, an array of five individually addressable

lenses was designed. The device is made from thin film electrodes, dielectric and hydrophobic coating on silicon and glass substrates in a three-chip stack. The device is sealed together with anodic bonding.

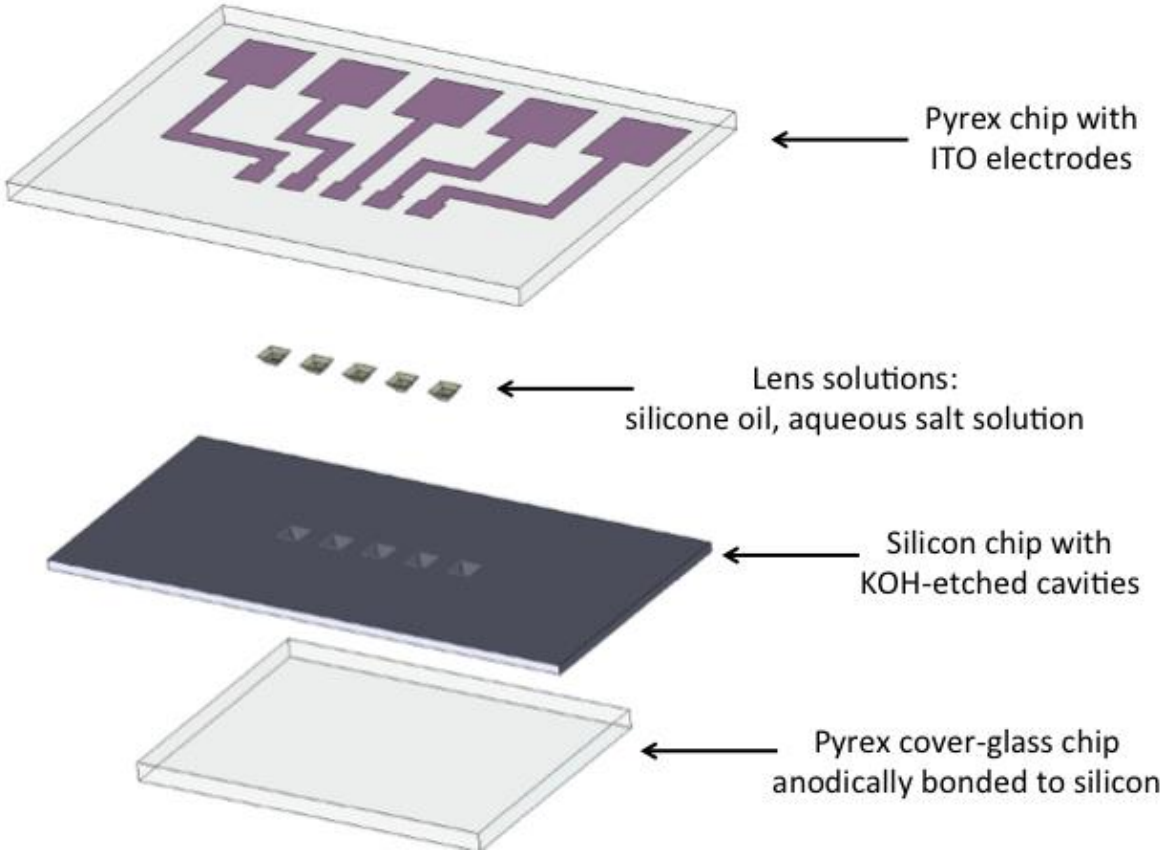

Figure 3-2 A solid model of the initial lens design. The aperture openings vary from 0.5mm to 2mm, while the pitch varies from 2.5mm to 4mm. Figure courtesy of Keith Cobry.

In fall 2011, I started on the project. The goal of the one dimensional array with separately controlled elements was to show proof-of-concept for lens arrays that are able to compensate wavefront distortion such as axial misalignment in laser diode arrays [96]. The versatility of a lens array with individually tunable lens elements provides a nice alternative to making a custom correction lens array to compensate for misalignment that may come from fabrication. A one-dimensional array can solve this problem with a straightforward fabrication layout, as the electrodes can fan out away from the array. A two-dimensional, high fill-factor array with

individually tunable elements would be a powerful optical device for adaptive optics systems and wavefront engineering. However, this device requires a very difficult fabrication process and layout in order to maintain high fill factor and electrical connection to each array element. While reported fabrication methods demonstrate array capability [10], [23], the challenge of individually addressable array elements so far has prevented this technology from maturing. For this device, the goal of demonstrating separately controllable lens elements required only a one-dimensional array.

The lens array without the cover slip on top can be seen in Figure 3-3. It is made up of a three chip stack of glass-silicon-glass with the liquids residing in cavities etched through the silicon layer. The silicon is doped and acts as the common electrode between each lens cavity while the separate electrodes made from patterned indium tin oxide (ITO) on the glass can be seen fanned out from the center of the device to allow for electrical access via probe or wires. The fabrication process for this lens array device is detailed in the Section 3.1.1.

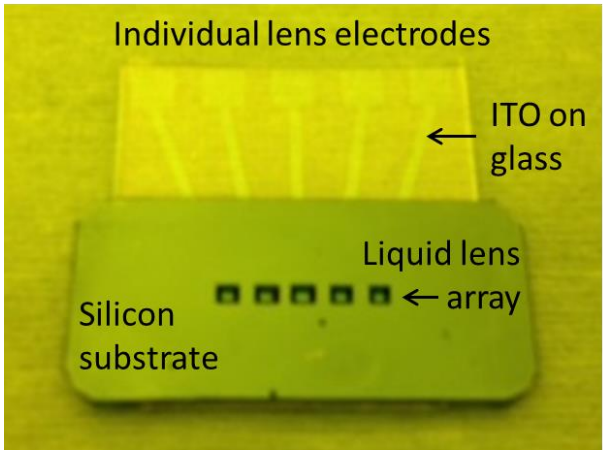

Figure 3-3 The initial liquid lens array developed in 2011. This image was taken before the top cover slip was bonded onto the array. The 5 individual electrodes can be seen addressing each lenslet, while the silicon itself acts as the reference electrode. Figure from [21].

3.1.1 ***Lens array fabrication methods***

The array of lenses is formed within a three chip stack consisting of a bottom glass slide with patterned ITO electrodes, a silicon middle layer with cavity walls defined by potassium hydroxide (KOH) through etch, and a top cover glass to contain the liquids, as shown in Figure 3-4. KOH etches silicon in atomically smooth planes, which is crucial to electrowetting as surface roughness can cause hysteresis in droplet edge movement and ultimately lens performance [70]. However, one drawback to the KOH etched (100)-cut silicon is that the sloped sidewalls characteristic of the anisotropic etch on silicon's diamond lattice prevents high fill-factor.

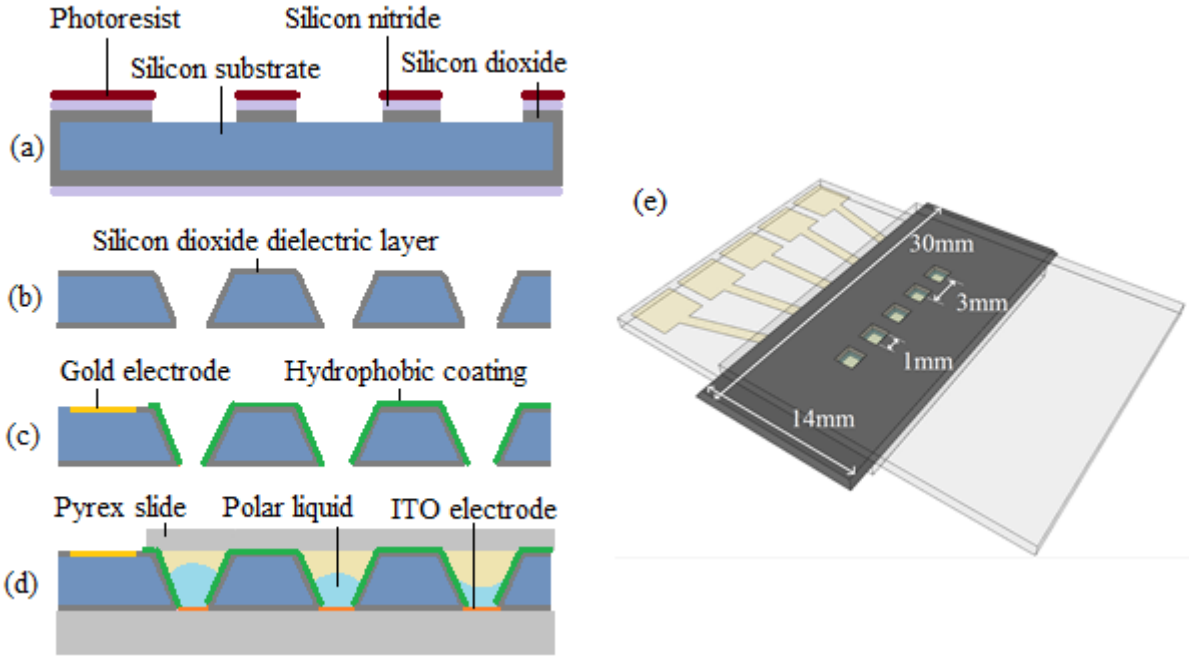

Figure 3-4 Liquid lens array fabrication process. (a) Silicon dioxide was thermally grown, silicon nitride was deposited by PECVD process, photoresist was lithographically patterned, and buffered oxide etch exposed the silicon. (b) A wet KOH etch through the silicon created the cavities to hold the liquid lenses with 1 mm^2 apertures. Thermal oxide was regrown as the dielectric layer. (c) The sample was shadow masked and exposed to reactive ion etching to make electrical contact to the substrate for Ti / Au electrode deposition. A hydrophobic fluorocarbon polymer (C_4F_8 gas precursor) was deposited on the substrate within an ICP system. (d) The arrays were then bonded onto glass slides with patterned ITO electrodes. After filling the cavities with the conducting and non-conducting liquids the device was capped with a Pyrex slide. (e) The assembled lens array device (to scale). Note that due to the anisotropic nature of the KOH etch the minimum aperture size is 1 mm^2 and occurs on the bottom side of the silicon. Figure from [21].

The fabrication process began with double side polished 500 μm thick, 76.2 mm diameter n-doped (100) silicon wafers which serve as the common electrode (10 - 30 Ω· cm resistivity). To protect the silicon through the aggressive KOH etch, 250 nm of silicon dioxide (SiO_2) was thermally grown and 550 nm of low stress silicon nitride (Si_3N_4) was deposited on both sides of the wafer using plasma enhanced chemical vapor deposition (PECVD) [97]. Photolithography was used to define the 1 mm^2 square apertures for the lens array. A 1:50 buffered hydrofluoric oxide etch was used to expose the silicon to allow the KOH to etch through the silicon. The wafer was submerged in 40% KOH at 70°C and allowed to etch until completion. This wet etch was chosen because it yields extremely smooth sidewalls, which reduce the effects of contact angle pinning and hysteresis [13]. After the KOH etch, the remaining SiO_2 and Si_3N_4 layers were removed with another buffered oxide etch.

Next, the dielectric layer of 250 nm silicon dioxide was thermally grown at 1100°C in a hydrogen and oxygen environment. Thermal oxide was chosen because it is pinhole-free down to nanometer thicknesses [98], ensuring minimal current leakage during operation. The wafers were masked and processed in a reactive ion etch to expose the bare silicon near the edge of the sample. This was immediately followed by a thermal evaporation of 15 nm titanium and 85 nm of gold to create an electrical contact to the silicon. For the final processing step with the silicon substrate, a hydrophobic layer was deposited on top of the dielectric. Two hydrophobic layers were used for different devices: the first was Teflon AF 1600 and the second was a Teflon-like fluoropolymer commonly used as the passivation layer in the Bosch process [99]. Teflon AF was dip-coated from a 10:1 solution of Fluorinert FC-77: DuPont Teflon AF 1600 and baked above its glass transition temperature at 170°C for 30 minutes. The Teflon-like fluoropolymer was deposited in an inductively coupled plasma system. A C_4F_8 precursor gas was introduced in the argon plasma to yield a 20 nm thin polymer hydrophobic layer via PECVD. This

vapor-phase deposition produced a uniform hydrophobic layer suitable for use with electrowetting systems [13].

*3.1.2 **Electrowetting lens array materials and assembly***

Each lens in the array receives a separate voltage through the patterned ITO electrodes. Tuning was achieved by applying a 5 kHz AC square wave to the electrode. AC voltage was chosen to reduce contact angle hysteresis by minimizing charging of the dielectric. For the initial experiments measuring change in focal length and lens aberrations of single lenses, a blank Pyrex glass slide was anodically bonded to the bottom of the silicon device layer with 1500 V at 300°C for approximately 6 hours. Trimethyl-siloxy-terminated poly(dimethylsiloxane) silicone oil (Gelest DMS-T11, hereafter referred to as *silicone oil*) and deionized water with 1% SDS surfactant (Alfa Aesar A11183, hereafter called *SDS solution*) were chosen as the non-polar and polar liquids, respectively. The surfactant was chosen to reduce the surface tension between the water and oil such that the voltage required to adjust the contact angle is further reduced [58]. Silicone oil was chosen for low viscosity and nearly the same density as water (density difference 0.07 g/mL). A micro-pipette was used to deposit liquids into the lens cavities. The top glass with patterned ITO electrodes was aligned and clamped onto the filled silicon chip to complete the device for lens characterization and focal length tuning.

Testing the individually addressable lens elements required bonding the electrode-patterned glass onto the bottom of the stack to avoid potential shorts between lens cavities. These shorts were being caused by the polar liquid trapped between the top glass and the silicon, creating electrically conductive liquid bridges between lens cavities. Avoiding this problem meant bonding the ITO patterned substrate to the bottom of the stack first. Since the ITO is not secured by the anodic bonding process, a different approach was implemented to secure the glass to the

substrate. Aperture holes were cut into an adhesive double-sided kapton tape, and the silicon, tape, and glass were aligned under a microscope and pressed together to bond. The conducting liquid chosen for this test was a 1:1 mixture of Cargille immersion liquids OHZB and OHGL (Cargille Labs 19580 and 19581). These were chosen for higher index contrast to clearly depict the individual focal length tuning, and for higher viscosity to mitigate liquid leakage through the porous tape bond.

*3.1.3 **Lens array characterization***

The optical characterization of the lenses was done in collaboration from Robert Niederriter, who set up the focal length measurements and the aberrations quantification. I provided the lens arrays for testing and assisted with the experimental design and measurements.

Focal length tuning was measured by passing a HeNe laser beam through the liquid lens and recording the spot size on a wavefront sensor. Using SDS solution and silicone oil as the lens liquids, optical power is tunable from -29 to -34 m^{-1} (-30 to -34 mm focal lengths) by applying up to 6 V_{rms}. Further voltage increase caused hydrolysis to occur, indicating current spikes through the device. Hydrolysis is evident by observing the formation of gas bubbles, as would occur if current passing through the water caused a separation of hydrogen and oxygen. Observation of the device during breakdown showed that these bubbles were formed exclusively at the bottom opening of the silicon, where the KOH anisotropic etch defined the lens cavity to a sharp edge. Since the silicon is acting as an electrode, charges appearing at this edge caused local electric field enhancement, as is common for sharp edge emitters [100-101]. While the 6 V_{rms} is not enough voltage to cause bulk breakdown of the 250 nm thick thermal silicon oxide dielectric, the local field enhancements was enough to cause local breakdown, enabling shorting between electrodes and causing hydrolysis at the edges and device failure at much lower voltages.

One way to mitigate this early onset of device failure due to microshorts in the device is to switch ion materials. An aqueous solution using large ion sizes has been shown to extend the working voltage range in electrowetting before these shorts occur through the dielectric [92]. Following the successful use of alternative ion sources for electrowetting from Krogmann [14], we switched to using commercially available optical liquids from Cargille, the OHZB (containing zinc and bromine) and OHGL (a polyhydric alcohol) solutions. The OHZB provided the ion source and the OHGL helped reduce the viscosity to simplify the liquid dispensing in the lens cavities.

The lens array with patterned ITO on the bottom was filled with a 1:1 mixture of OHZB and OHGL liquids. The electrodes allow separate tuning of each lens' focal length, as shown in Figure 3-5.

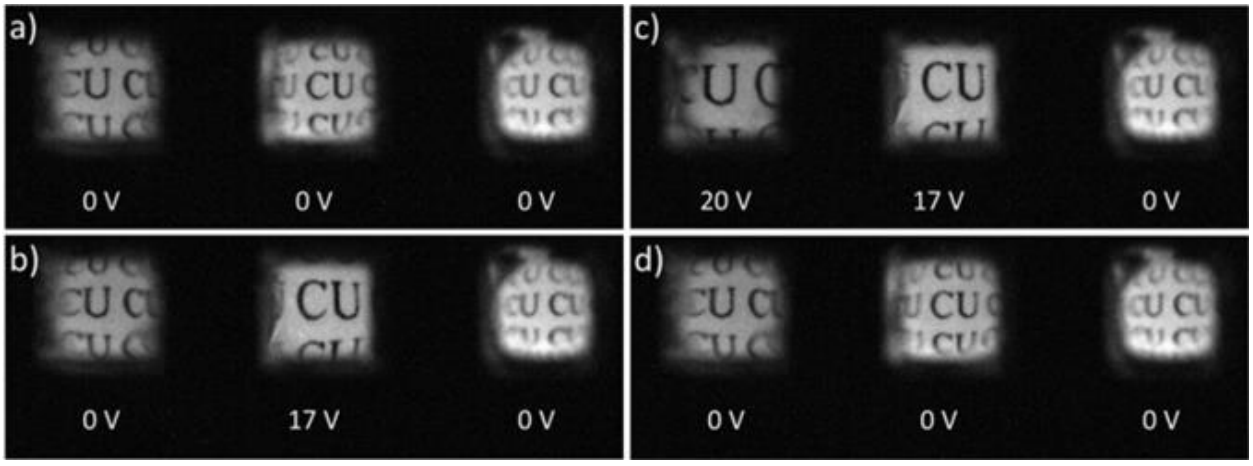

Figure 3-5 Images demonstrating separately tunable adjacent lenses. This three-lens array used Teflon AF as the hydrophobic layer and the mixture of Cargille OHZB and OHGL as the conducting liquid. Circular pinhole apertures (~1 mm diameter) were aligned beneath the lens array to reduce image distortion from the square corners. Viewed through the lens array is a printed page of the university's acronym, CU, each letter measuring 1.3 mm in height. (a) No voltage applied to any of the lenses; (b) 17 Vrms applied to the center lens; (c) 20 Vrms applied to the lens on the left, 17 Vrms applied to the center lens; (d) No voltage applied to any of the lenses, showing they return to their original focal lengths, as in (a), with little or no hysteresis. Figure from [21].

At first no voltage is applied, followed by separate tuning of the middle and left lenses with 17 V_{rms} and 20 V_{rms}, respectively. Finally, the voltage was removed and

the lenses return to their original focal lengths. The mixture of Cargille liquids successfully allowed further voltage tuning of the liquid lenses without dielectric breakdown or microshorting until about 25 V_{rms}, significantly higher than the SDS water solution, which contains the smaller sodium ion.

One direct application of a one-dimensional array of separately tunable lenses is correcting for misalignment in laser arrays. This is compatible with arrays of manually aligned fibers and the misalignment laser diode arrays undergo during packaging due to thermal mismatch between the lasers and heat sink, referred to as "smile" (Figure 3-6).

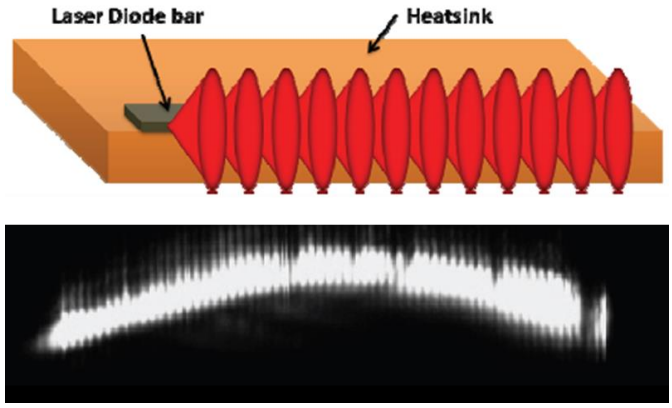

Figure 3-6 Example of "smile" seen in laser diode array. Top depicts a schematic of arrayed laser diodes emitting light, shown in red. Bottom shows the effect of misalignment that can occur in these systems (smile). Figure from [96].

A vertical distortion in the laser array results in emitters which are offset along or transverse to the optical axis, which translates into a tilt once passed through a fixed microlens array. Smile is a costly problem that reduces the usable laser power and typically requires a custom lens array or phase plate to correct the misalignment of the diode array [102-103]. Prism arrays can compensate for transverse smile and individually addressable electrowetting lens arrays can correct the axial component.

We have used our lens array for preliminary demonstrations of the axial misalignment compensation. Laser light at 980 nm was coupled into an array of 4

single-mode fibers mounted in a v-groove array to imitate an array of laser sources, with ~1 mm misalignment along the optical axis. A lens array was positioned about 2 mm from the end of the fiber array, and a CCD camera was used to collect the focused light. We tuned the lens focal lengths to alter the beam widths from as large as 1.9 mm to match a 1.1 mm reference diameter, correcting for millimeter-scale axial misalignment of the individual fibers. Figure 3-7 shows a cross section of irradiance as a function of position.

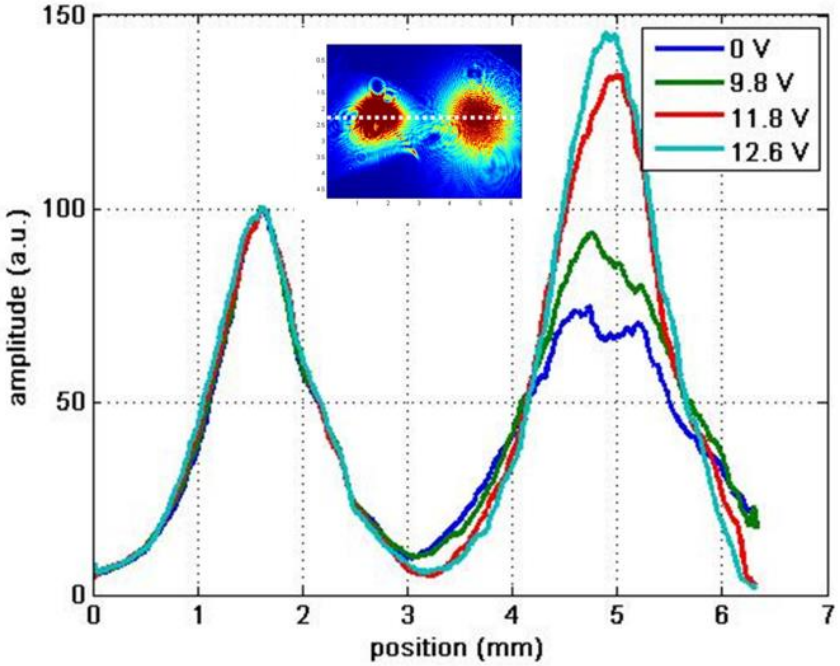

Figure 3-7 Laser spot size tuning. Plot shows measurement of laser intensity as a function of position on CCD camera along a reference axis shown as the dotted white line. The first peak represents the left laser source and the second represents the source on the right. The two laser fiber sources were axially misaligned by ~1 mm. By adjusting the focus of the lens on the right, the corresponding spot size was corrected. For this particular pair of misaligned laser sources, ~11 V was applied to the right liquid lens to match the spot sizes. The inset shows the two spots with no applied voltage, with a line indicating the cross section plotted. Figure from [21].

As the focal length of the lens on the right was adjusted, the spot size and therefore irradiance pattern along the reference line were altered. These particular fibers were misaligned by ~1 mm but the spot sizes from the fiber array were matched by applying ~11 V to one of the lenses. The inset shows the two spots with

no applied voltage, slightly distorted by the imperfections in the circular apertures used to avoid the square edges of the lenses. Using lower numerical aperture fibers would reduce diffraction effects from the edges of the lens array and improve the beam quality.

Lens quality is vital for many applications. To measure the lens aberration, a spatially-filtered 532 nm laser beam was passed through the 1 mm^2 lens aperture and expanded 2.5 times to fill the input of a Wavefront Sciences μ-eye Shack-Hartmann wavefront sensor, loaned by Dr. Robert McLeod. The lens used to test aberrations was filled with silicone oil and SDS solution and utilized the vapor-phase fluoropolymer coating as a hydrophobic layer. The wavefront emerging from the lens was measured to have 550 nm rms deviation from a spherical wavefront. Much of this error is due to the square corners of the lens, where the liquid surface is not expected to be spherical. By including a 1 mm diameter circular aperture matching the lens size, the rms wavefront deviation is reduced to 80 nm. This compares favorably to the literature where, for comparison, a 1 mm diameter solid microlens was shown to have 79.25 nm rms wavefront error [79], and a similar square liquid lens was measured to have 211.16 nm rms deviation (using a similar circular aperture) [14]. To quantify the lens quality, the wavefront was fitted to Zernike polynomials [104] with Zernike coefficients listed in Table 3.1.

Table 3.1. Measured Zernike coefficients of microlens.

Aberration	Zernike coefficient (μm)
Astigmatism 90°	0.445
Astigmatism 45°	0.4997
Coma x	-0.0439
Coma y	0.0282
Spherical aberration	-0.0324

In particular, we measured an order of magnitude less spherical aberration, but approximately twice as much astigmatism than [14], a similar square

electrowetting microlens. These aberrations lead to rms wavefront variation of λ/12 over the 100 μm diameter center of the lens, sufficiently small enough to justify using the lens array for applications where the phase of light is important, as discussed and demonstrated in the following section. While we have measured the lens quality without applied voltage, we do not expect a significant change in quality during tuning. The change in spherical aberration with lens tuning was modeled numerically based on the methods of [18]. We calculated the spherical aberration to be small in every tuning condition, increasing from -0.017 λ in the resting state to -0.011 λ with 5 V_{rms} applied.

3.1.4 ***Phase control***

Phase control in optical systems (piston control) is a powerful tool for applications like coherent combining, pulse synthesis and wavefront control. The tunable liquid lenses described in this paper can be used to control phase independently from curvature [7]. Piston control can be achieved when the varifocal lens array is placed at the focal point of a fixed lens array telescope with the same pitch. Figure 3-8(a) illustrates the scheme.

By placing the liquid lens at the focal point of a fixed lens telescope, the spot size on the lens is minimized and phase can be adjusted with minimal effect on the wavefront curvature. Because the liquids within the cavity are constrained by constant volume, the center position of the oil-water boundary shifts as the lens is tuned. Passing through more oil increases the optical path length (OPL) and therefore changes the phase of the light exiting the liquid lens. In this way, the electrowetting lens element can double as a voltage-actuated phase control device.

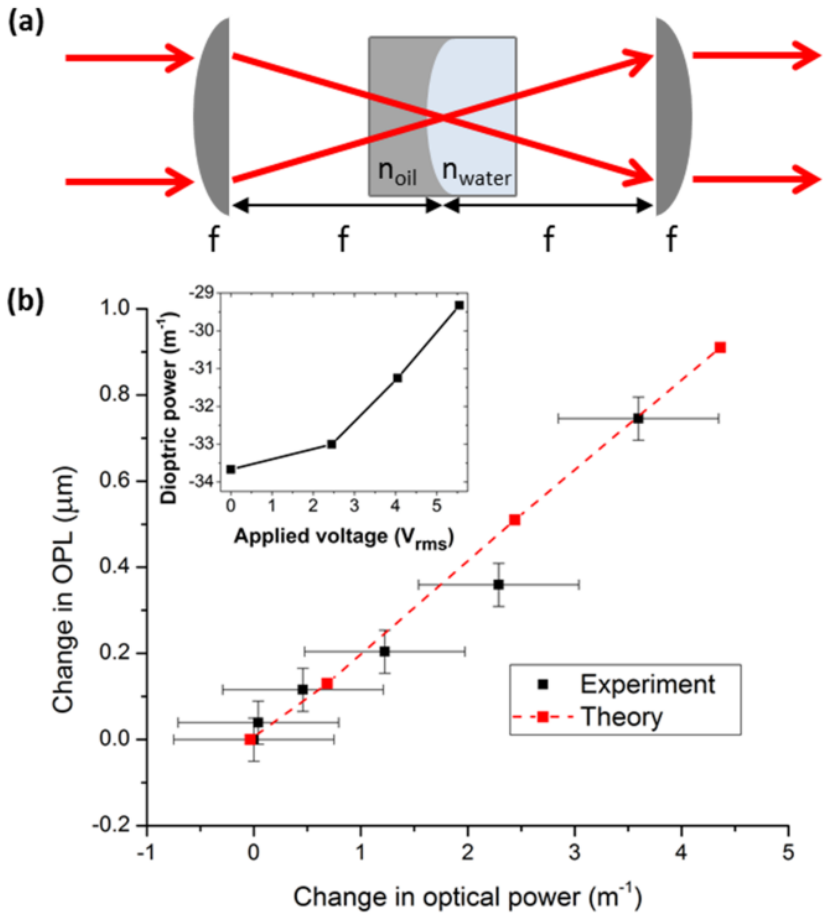

Figure 3-8 Piston control of electrowetting lens element. (a) Schematic for piston control using a tunable lens at the focus of a telescope (not to scale). (b) Measured change in optical path length through the liquid lens with AC voltage applied. Measured change is compared to that predicted by a Zemax model of the lens, using independent measurements of the optical power (theory), inset. This lens used a Teflon AF hydrophobic layer, with silicone oil and SDS solution as the lens liquids. Figure from [21].

While the wavefront curvature is unchanged due to a tight focus at the interface of the liquid lens, the tip/tilt could be affected if the optical axis of the electrowetting lens is unstable. The main cause of axis instability in electrowetting lenses is gravitational pull causing deformation of the spherical lens shape due to slightly mismatched liquid densities. Gravitational deflection shifts the liquid lens optical axis away from the center. Simulations have shown that gravity plays a negligible role in the lens shape for lens diameters smaller than 2 mm, taking into account the density difference between the silicone oil and SDS solution used in this

work [7]. Thus, lens design produces the optical axis stability necessary for the demonstrated piston adjustment technique.

We have verified experimentally that a tunable liquid lens placed at the focus of two fixed-focus lenses can be used to manipulate the phase of light passing through the device. We used a HeNe laser (633 nm) in a Mach-Zehnder interferometer with the fixed/tunable/fixed lens combination shown in Figure 3-8(a) occupying one arm. The fixed-focus lenses were chosen with focal length of 50 mm such that the Rayleigh range was greater than the thickness of the liquid lens (0.5 mm), ensuring a narrow beam passing through the tunable lens.

To summarize, I fabricated an array of liquid lenses and demonstrated both curvature tuning and phase tuning. Robert Niederriter and I demonstrated a basic application of individually addressable lens arrays for compensating axial misalignment in laser diode arrays, and successfully corrected for 1 mm misalignment, more displacement than typically seen in laser diode manufacturing misalignment. Furthermore, we demonstrated for the first time that a closed volume electrowetting device can act as a phase modulator, if the electrowetting device is placed at the focal point of a telescope lens set-up, thereby decoupling the focusing effect of the electrowetting element.

The challenges faced were in operating this design at voltages. AC voltages beyond 10 V_{rms} for water and 25 V_{rms} for the Cargille zinc bromide solution. These values would cause dielectric breakdown and allow charges to flow, causing hydrolysis and catastrophic failure of the device. The reasons for this are twofold: (1) the KOH etched silicon left a very sharp corner on the bottom of the device that was close in proximity to the ITO counter-electrodes. Sharp corners on a conductor cause high electric fields due to local electric field enhancement [100-101]. This would prevent higher voltages that might normally be below the threshold of dielectric breakdown on a flat surface. (2) Electrowetting systems that draw small

ions toward a thin film dielectric see larger leakage currents from these ions infiltrating through the dielectric compared to systems that use large ions. This is a function of both ion size and the quality of the dielectric.

The next generation of liquid lenses discussed in the next section addresses the first point with a new design, inspired by Kuiper and Hendriks [15]. To address the second point, I investigated utilizing large ions with higher quality thin film dielectrics to enable very low leakage current and low operating voltage.

3.2 **Glass Tube Liquid Lens Device Design**

The next generation of lenses is based on a glass capillary tube, rather than silicon. Without a deep reactive ion etch, a KOH silicon through etch will yield square apertures and the unfavorable sharp corner at the bottom of the device. The best solution is to start with circular apertures and use a transparent medium to create the lens, enabling visual examination of the lens curvature vs. tuning. The second liquid lens scheme is designed, as shown below in Figure 3-9 [27]. The lens is formed within a glass cylinder that has thin film sidewall electrode, dielectric and hydrophobic layers. The bottom substrate is an ITO coated glass slide to electrically address the electrowetting liquid and maintain optical transparency.

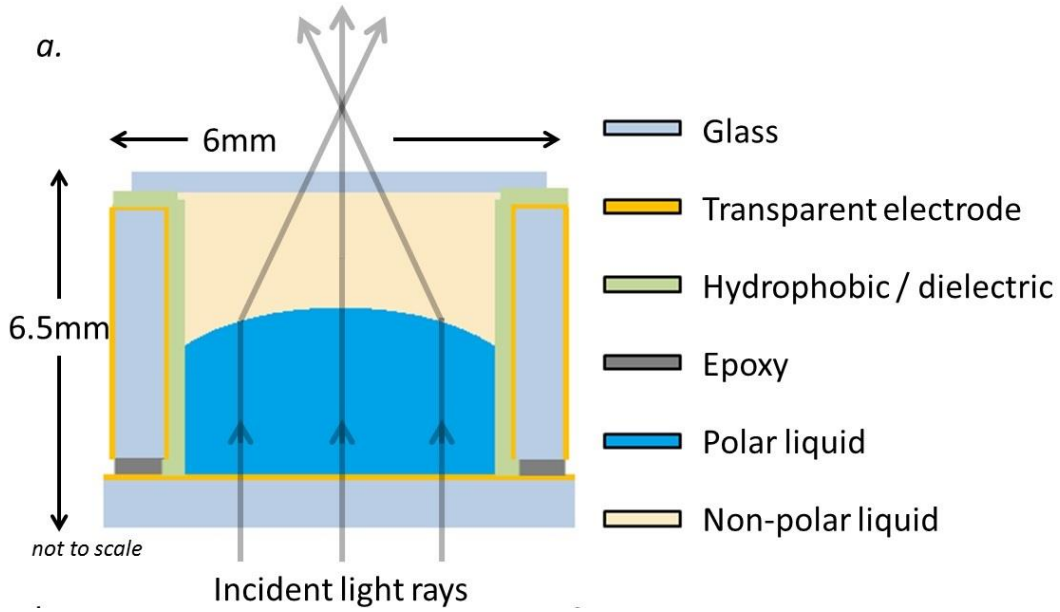

Figure 3-9 Cross-sectional schematic of revised liquid lens design. The inner diameter of the glass tube containing the liquids is 2.7mm while the outer diameter of the cylinder is 6mm. The height is 6.1mm in total. The converging or diverging nature of the lens depends on the refractive index of the polar liquid and non-polar liquid. When $n_{polar} > n_{nonpolar}$ we achieve a converging lens as depicted in the schematic. Alternatively, when $n_{polar} < n_{nonpolar}$, a diverging lens is realized and the rays will bend away from the normal. Figure from [27].

The goals of this new lens design are as follows:

1) Achieve high focal length change (from initial f to ∞) with low voltage (<15 V)
2) Allow for converging and diverging lens operation while testing new polar material in lens setup
3) Demonstrate microscope and microendoscope applications

The lens device requires a redesign to achieve these goals. Aside from the differences in the lens design and layout, the biggest changes from the initial lens array device that affects electrowetting performance comes from switching to a better materials system.

3.3 **Materials Selection**

Moving away from a silicon substrate alleviates the challenge of square apertures and sharp edges, but introduces new requirements for thin film deposition. A conductive electrode must be deposited over the glass and into the interior of the cylinder. To maintain visual transparency through the side of the liquid lens, a transparent conductive oxide, Indium Zinc Oxide (IZO) is selected for the sidewall electrode, as its deposition can be done with a simple sputter step. A commercially available ITO coated glass substrate is used for the counter electrode, addressing the liquid on the bottom of the device.

As for the dielectric, while thermally grown silicon dioxide is conformal and pinhole free [98], it requires a silicon substrate. The new glass lens design requires conformal deposition of the thin film dielectric over the glass tube and electrode. This presents the challenge of finding a deposition technique and material that can be coated in the vapor phase and eliminate pinholes at low thicknesses. Parylene-N and -C are polymer variants of poly(para-xylxylene) that have long been standard dielectric for electrowetting, due to good dielectric strength and vapor phase conformal coating. However, these configurations of parylene suffer from charge trapping [105] and poor resistance to ion leakage [87]. These are indications that reducing the dielectric thickness in order to reduce the electrowetting voltage will introduce challenges in reliable operation. However, a relatively new configuration of the polymer called parylene-AF4 or parylene-HT has shown promise as a dependable dielectric with reduced charge injection effects [87]. Figure 3-10 illustrates the differences between various types of parylene.

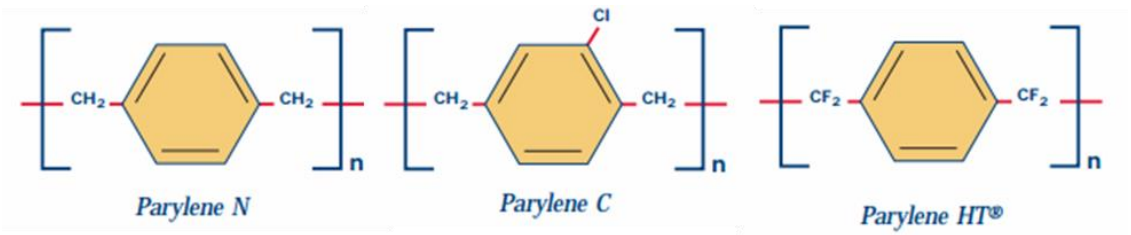

Figure 3-10 Comparison of parylene variants. Parylene-N is the standard form of poly(para-xylxylene), parylene-C includes a dangling chlorine bond, and parylene-HT replaces the hydrogen with fluorine. Figure from [106].

The alpha hydrogen is replaced by fluorine which allows increased penetrating power of the vapor phase coating [106]. Parylene-HT is fluorinated, whereas parylene-C contains a Cl atom attached to the benzene ring. Due to its dipole moment, the chlorinated parylene-C monomer readily condenses onto substrates in the vacuum chamber while the parylene-HT monomer requires more surface energy change for condensation. This allows it to conform to complex geometries more readily than parylene-C. The high surface conformity of parylene-HT allows it to form films with fewer pinholes at than parylene-C [107]. This characteristic of parylene-HT is what makes it more resistant to charge injection, particularly at submicron film thickness.

In conjunction with a higher quality dielectric, it is important to take care in selecting a polar material and ion source that will not infiltrate the dielectric. A vast majority of the electrowetting optical devices have used water as the polar liquid in the device, simply because it is a universal solvent for the ion sources needed in electrowetting. However, it may not be the best polar liquid to use since it is a small molecule and can penetrate any pinholes or defects within a thin film dielectric. Water begins to permeate though polymers and eventually leads to device failure. The rates at which this happen vary greatly depending on the polymer, yet the rate of permeation through polymers is inversely dependent on the permeate size [108].

Furthermore, the ion source used in the polar liquid also plays a part in the dielectric's resistance to ion leakage. Raj and Dhindsa *et al.* investigated the effects of ion size and liquid material, the main results of which can be seen in Figure 3-11.

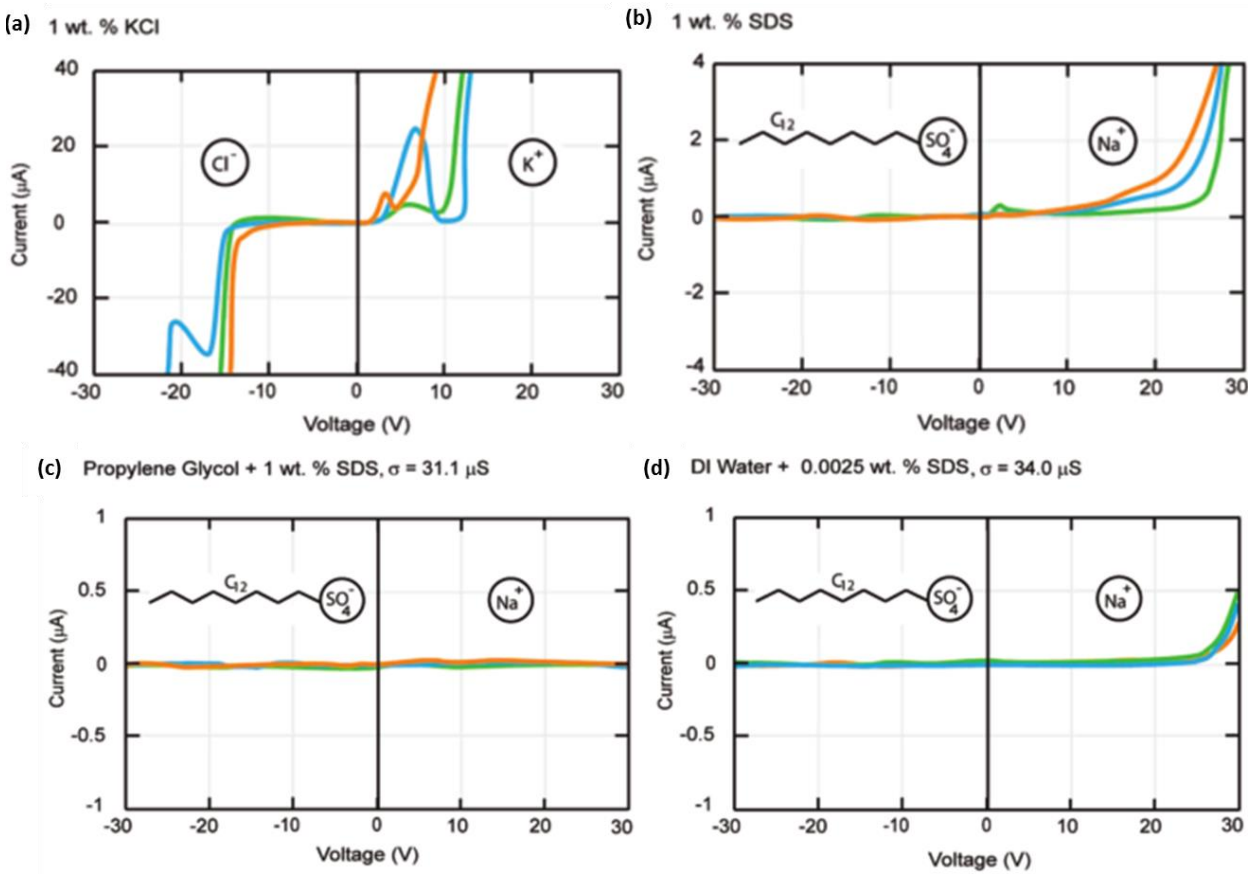

Figure 3-11 Study on ion size and liquid material. I-V curves of the electrowetting system with various ion sources. (a) 1 wt. % KCl in water and shows clear indications of shorting occurring where both cations and anions leak through the dielectric and spike the current. (b) Shows 1 wt. % sodium dodecyl sulfate (SDS) which has a rather large anion including a chain of 12 carbons compared to the much smaller cation of sodium. The I-V curve shows low leakage current through -30 V where the positive side depicts current spikes associated with ion leakage. (c) Shows 1 wt. % SDS in propylene glycol and (d) shows 0.0025 wt. % SDS in water. Propylene glycol shows minimal current leakage with 1 wt. % SDS from -30 to +30 V while DI water begins to show spikes in current from the Na^+ ion, even with a much lower concentration of 0.0025 wt. % SDS. Figures from [92].

It is clear that the polar material affects the leakage of ions through the dielectric, as the propylene glycol has 400 times the concentration of ions dispersed within it yet still shows no sign of high leakage current associated with ion penetration through the dielectric. Another reason to search for alternative

electrowetting liquids is to increase the range of wavelengths for the lens devices, but this will be explored more completely in Chapter V.

As for the ion sources described in Figure 3-11, the SDS surfactant molecule used in the SDS solution is shown below in Figure 3-12.

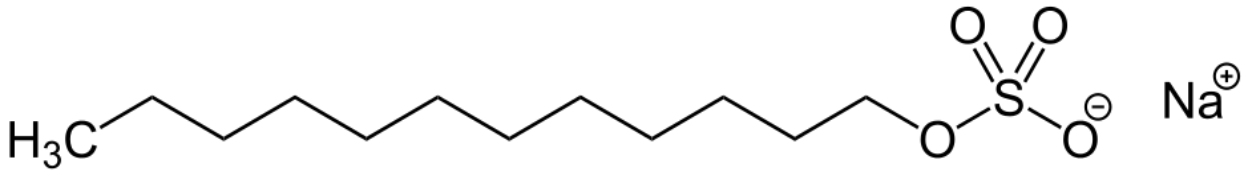

Figure 3-12 Sodium Dodecyl Sulfate (SDS). SDS is a commonly used surfactant and ion source for electrowetting systems. It greatly reduces the liquid/liquid surface tension between polar and non-polar liquids, thus reducing the required electric force needed to alter the contact angle at the liquid interface. The negatively charged dodecyl sulfate ion is also very large, making it a preferred ion to attract toward the thin film dielectric stack, as it has less chance of leaking through as voltage is applied. Figure from [109].

The SDS is a common surfactant and it serves two purposes in the system: (1) it significantly reduces the surface tension between the polar liquids and the oil (down to 6 $\mathrm{mN \cdot m^{-1}}$ with water [87]), and (2) it gives provides a large ion source to be transported during electrowetting. SDS breaks down into two ionic structures, Na^+ and dodecyl sulfate with a negative charge as shown above Figure 3-12. Thus it is best to apply a negative DC voltage to the polar liquid when using SDS, as this will attract the small sodium ion to the electrode and the much larger dodecyl sulfate ion to the liquid-dielectric surface. The SDS ionic molecule has a total radius of 1.75 nm, with the sodium ion accounting for 0.227 nm [110]. Using the larger ion at the dielectric interface is beneficial as it reduces the chance that the ion will penetrate the inherent pinholes and defects in the thin film [92]. This reduces overall leakage current, as well as contact angle hysteresis due to trapped charge.

3.4 **Glass Tube Liquid Lens Fabrication**

As seen in Figure 3-9, the liquid lens is contained within a glass tube with inner diameter of 2.7 mm and outer diameter of 6 mm. The tube is cut down to 5 mm in

height and cleaned in an ultrasonic bath with acetone then isopropyl. The sidewall electrode IZO is deposited by DC magnetron sputter. The samples are fixed within the sputter chamber sitting upright using adhesive double sided Kapton tape, known for its very low outgassing potential. To ensure minimal defects and good conductivity of the film, the sputter chamber is pumped to a base pressure of 1 μTorr. The sputter is performed in an Argon environment at an operating pressure of 8 mTorr to reduce the mean free path within the chamber to lengths much shorter than the distance between target and sample. This helps to produce a continuous, conformal coating that covers the outer sidewall, inner sidewall and top of the cylindrical cavity [99] and enables the electrical addressing of the inner sidewall electrode from the outside of the device. The IZO deposition is run at 120 W for 12 minutes, producing a ~200 nm thin film. A multimeter is used to confirm electrical connection from inside to outside of the lens device.

Next, the dielectric and hydrophobic films are applied. Since electrical access to the outer sidewall must be maintained, Kapton tape is wrapped around the outside of the lens device to mask it for the subsequent dielectric and hydrophobic coating depositions. A 300 nm thick parylene-HT film is deposited commercially by VSI Parylene, a company that specializes in parylene coatings. The parylene deposition follows the Gorham process [111]. The Kapton tape is left in place for the hydrophobic coating. The hydrophobic layer is added by dip coating a 1:20 solution of Dupont's Teflon AF1600 : Fluorinert FC-40 and cured at 125 °C for 10 minutes then 170 °C for 25 minutes to yield a 100 nm thick coating. The thickness is measured on a flat companion piece with a profilometer to confirm. The adhesion of the cured Teflon to the parylene-HT is tested by tape exfoliation and resulted in no delamination. The Kapton tape is then carefully removed so as to not lift off the Teflon and parylene-HT from the top and inside of the device. This exposes the

outer IZO electrode for an electrical connection for the inner sidewall. The cylinder glass tube part of the device is now ready to bond onto the substrate.

The substrate is a commercial grade ITO coated glass substrate, with a 4-10 Ω· cm film on one side that acts as the counter electrode of the lens. The electrode directly addresses the polar liquid and is therefore in the optical axis, so high transparency is desired. The ITO glass substrate is 1.1mm thick and is cut down to 8mm x 8mm squares to allow for electrical connection once the lens tube is bonded onto the substrate.

The bonding is done with Masterbond's two part epoxy system EP30-2 to ensure a leak proof enclosure that resists water permeation and electrically isolates the substrate electrode from the cylinder sidewall electrode. The two parts are mixed in a 1:10 ratio of Part A : Part B and applied to the bottom of the glass tube by using a fine tip paint brush under a magnifying glass. The glass substrate is then carefully placed onto the epoxy-covered cylinder using tweezers. The freshly sealed device is cured at room temperature for 48 hours, and then cured at 95°C for 2 hours to solidify the bond.

With the bond completed, the device fabrication is finished. The lenses are filled by using a micro-pipette, capable of dispensing 0.5μL - 10μL of liquid. The polar liquid is dispensed in the bottom of the device first, and the non-polar oil is dispensed on top. The liquids are contained by placing a 0.17mm thin glass coverslip on top of the lens. The slip is scribed down to the size of the lens top and the surface tension of the oil on top holds the cover slip in place. The force is great enough to keep the cover slip in place even when holding the lens device upside down or sideways, as is necessary for some of the optical measurements. While it is not a permanent solution to sealing the liquids within the device, it makes for a good solution while troubleshooting the lenses and allows for easy switching of the

liquid components. The cover slip can easily be permanently fixed into place with epoxy.

3.5 **Optical Characterization**

The liquid lens device is tested using two different liquid combinations and two different dielectric films. In both liquid combinations, the non-polar ambient liquid is dodecane oil, which is a typical liquid used with electrowetting systems [23]. The polar liquids used are a solution of 1% by weight sodium dodecyl sulfate (SDS) and 99% by weight deionized water and a solution of 1% by weight SDS and 99% by weight propylene glycol. The refractive index of the dodecane oil is 1.420 [112]. The refractive index of the water is lower, at 1.333, and the refractive index of propylene glycol is higher, at 1.432 [112]. This means that given the high contact angle and subsequent convex curvature of the polar liquid in the device, the water-based system forms a diverging lens while the glycol-based system forms a converging lens. The values of these refractive indices are corroborated with measurements at the d-line (588 nm) by Abbe refractometer, loaned by Dr. Robert McLeod.

3.5.1 ***Water and dodecane diverging lens***

The SDS solution / dodecane oil combination was tested for lens operation. The contact angle of the liquids is measured by aligning a camera on the side view of the lens and taking images at each level of applied voltage. The images are processed with software program ImageJ and the contact angle of the liquid is measured with the DropSnake plug-in, which adds nodes along the edge of the droplet and forms a spherical cap based on the node positions. The edge of the liquid is defined and the program calculates the corresponding contact angles on the left and right side. Figure 3-13 shows a plot of the measured contact angle while tuning the lens voltage forward and back.

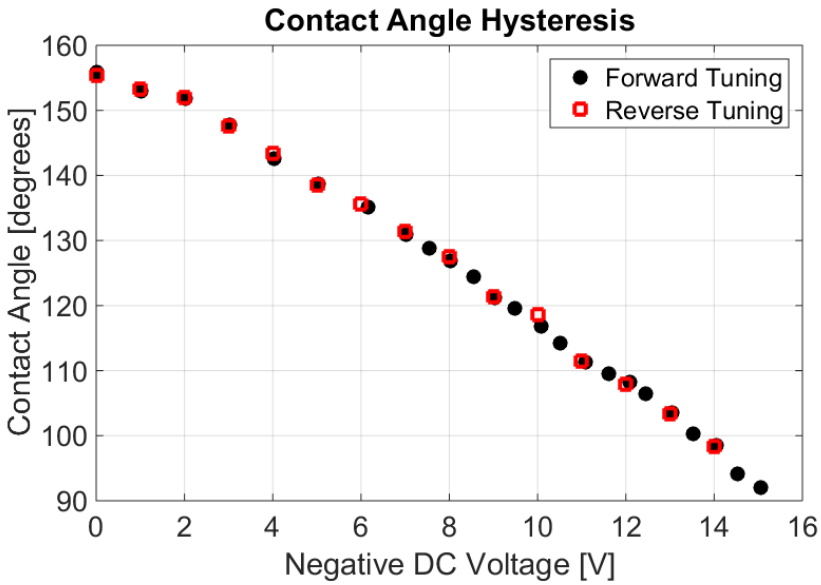

Figure 3-13 Plot of contact angle of the electrowetting liquid with respect to the sidewall over the tuning range of the diverging water-based lens. Average hysteresis of each measured data point is < 0.5° when tuning forward and back. Figure from [27].

The plotted contact angles are the average value between the two sides, giving a single contact angle value to reference when measuring hysteresis as it appears during forward and reverse voltage application. The measured contact angle has very little hysteresis when tuning the device, averaging < 0.5° when tuning from 0 V to -15 V and back. This compares favorably with reported hysteresis seen in electrowetting lens of 1-2° [19].

Images of the liquid lens at 0V and -14.5V can be seen in Figure 3-14. The bottom electrode is addressed with a clamp that is holding the lens in place while the sidewall electrode is addressed with a needle probe on a translation stage.

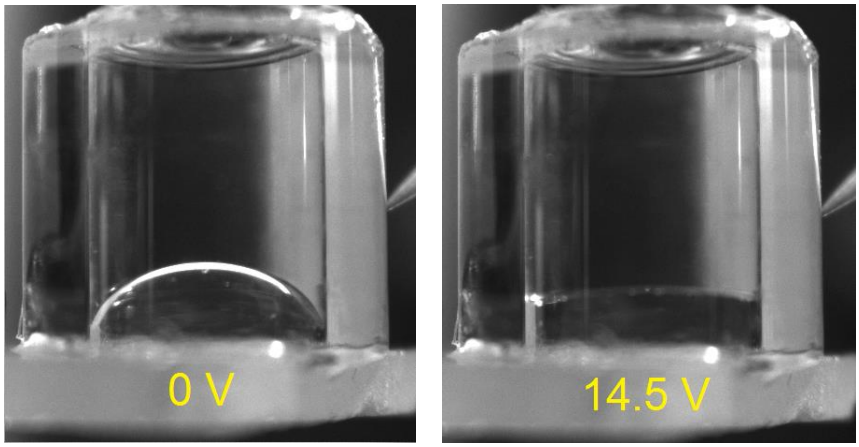

Figure 3-14 Images showing the curvature change of the lens. This lens is comprised of 1% SDS water plus dodecane oil with 300nm Parylene HT and 100 nm Teflon. The negative terminal of the DC voltage is applied to the substrate electrode which addresses the 1% SDS water solution and the positive terminal is applied to the needle probe. This builds the bulky dodecyl sulfate ions at the dielectric surface.

Next the optical power of the lens device is calculating by using the measured contact angle and diameter of the lens to determine the radius of curvature. Optical power performance of the water-based lens can be seen in Figure 3-15. By applying negative voltage to the polar liquid, we ensure that the large dodecyl sulfate ions are attracted to the sidewall with the dielectric. Application of -15 V DC tunes the liquid lens from resting power of -43 diopters to a flat liquid profile with 0 optical power. Continued voltage tuning to -30 V alters the optical power to +10 diopters, covering a focal length range of -23 mm through infinity and down to +100 mm.

Note that at -15 V the device begins the onset of contact angle saturation (CAS), which reduces and ultimately eliminates any further contact angle change with increased voltage. CAS is ubiquitous in most electrowetting experiments, and causes the contact angle response to deviate from the Lippmann-Young equation [70]. A comprehensive study by Chevalliot *et al.* [76] shows the invariance of contact angle saturation to a number of material parameters such as dielectric thickness, liquid-liquid surface tension, ion size and pH. At this time, there is no complete understanding in the electrowetting literature on what causes CAS. However, in our design, a marked difference in CAS is measured when the polar liquid in the

lens is changed from water to propylene glycol. Figure 3-16 illustrates the CAS discrepancy between the electrowetting liquids.

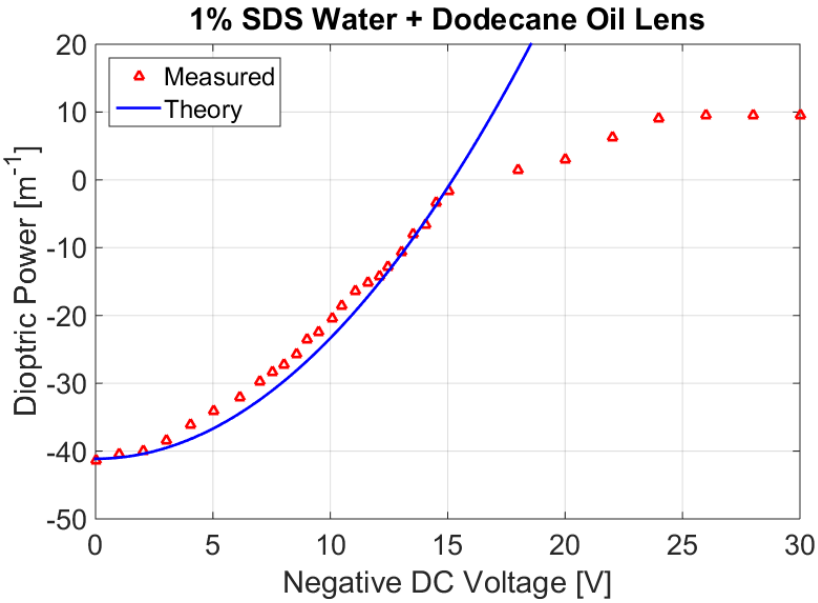

Figure 3-15 The dioptric power of the water-based lens agrees closely with theoretical values predicted by material properties and Lippmann-Young equation. The power tunes form -43 diopters to 0 diopters with the application of -15 V. Continued tuning realizes a positive lens up to +10 diopters before contact angle saturation. Figure from [27].

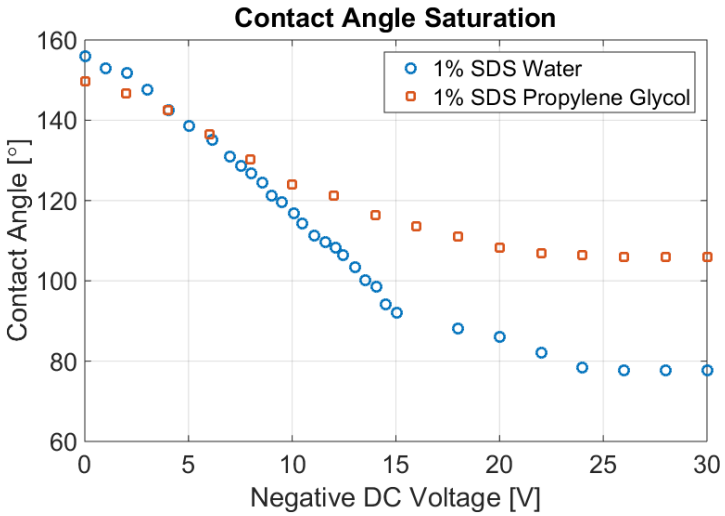

Figure 3-16 Comparison of CAS between water and propylene glycol. An approximately 30 degree difference in saturation angle is observed between water and glycol based polar liquids. Figure from [27].

The same SDS concentration is used as the ion source for both types of lenses, but we see a 30° difference in saturation angle. The differences between water and propylene glycol that could contribute to this discrepancy are: molecular weight and size, the polar component of their surface tension value, and the work of adhesion force that holds like molecules together. Since the ion source and concentration are equal and the parylene-HT dielectric resist charge injection, it seems unlikely that this drastic difference in CAS is due to trapped charge alone. The differences in material properties between water and glycol suggest that material interactions between polar liquid and non-polar liquid and/or substrate can have a large effect on CAS.

*3.5.2 **Propylene glycol and dodecane converging lens***

Despite the early onset of CAS, the glycol-based liquid lens was measured for optical power characterization. Images of the propylene glycol based lens are shown in Figure 3-17.

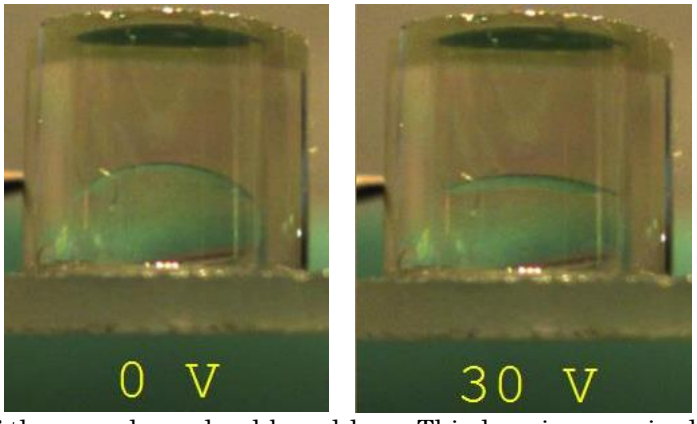

Figure 3-17 Images of the propylene glycol based lens. This lens is comprised of 1% SDS propylene glycol plus dodecane oil on 300nm Parylene HT plus 100nm Teflon.

Since the refractive index of the propylene glycol and oil is so close (only a 0.01 difference), the meniscus is hard to see. A colored post-it note is included on the backdrop to help provide contrast at the meniscus to see and measure the contact angle. CAS sets in before infinite focal length (i.e. flat liquid boundary) is achieved.

Figure 3-18 depicts the dioptric power of the converging propylene glycol and dodecane oil lens.

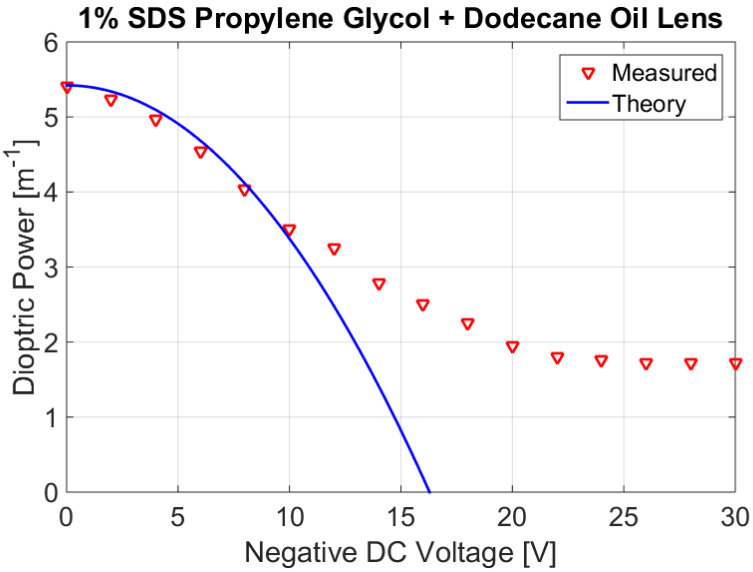

Figure 3-18 The optical power of the glycol-based converging lens agrees with theory until CAS onset at 10 V causes the response to begin to flatten out. The converging lens tunes from +5.4 diopters to +2.5 diopters with an applied voltage of -15 V. Increased tuning brings the power down to 1.7 diopters before full CAS. Figure from [27].

Due to the relatively small refractive index contrast between propylene glycol (n_d = 1.432) and dodecane oil (n_d = 1.420), the change in lens power with applied voltage is smaller than the water and oil lens. This enables finer precision control of the lens at the cost of total tuning range. The converging lens tunes from +5.4 diopters to +2.5 diopters by applying -15 V. The effect of CAS is stronger with the glycol-based device, and occurs at the lower voltage of approximately -10 V. Continued tuning up to -30 V reduces the contact angle from 150 degrees to 106 degrees before full saturation, covering a focal length range of +185 mm to +580 mm. Tuning 400 mm of focal length with -26V marks the lowest voltage to achieve such a focal length tuning range from a converging electrowetting based liquid lens reported to date.

Another important factor to consider when making these lens devices for low voltage operation is that implementing them with circuit board technology also

mandates low power consumption. The power consumption of the propylene glycol lens is measured by connecting an ammeter in series with the power supply driving the liquid lens. By measuring the current flow through the device (which, at DC is the leakage current through the dielectric) and multiplying it by the applied voltage, we achieve the total power consumption of the device. The power consumption of the propylene glycol lens device ranges linearly between 0 and 25 μW while applying 0 to -15 V. This is an order of magnitude lower than previously reported DC voltage based liquid lenses [4], [13], [14]. Low voltage and power requirements are crucial when integrating with chip scale microsystems, which is an attractive option for miniaturized variable optical devices such as electrowetting lenses, prisms and phase modulators [21]. The power consumption as a function of lens focal length is plotted below in Figure 3-19.

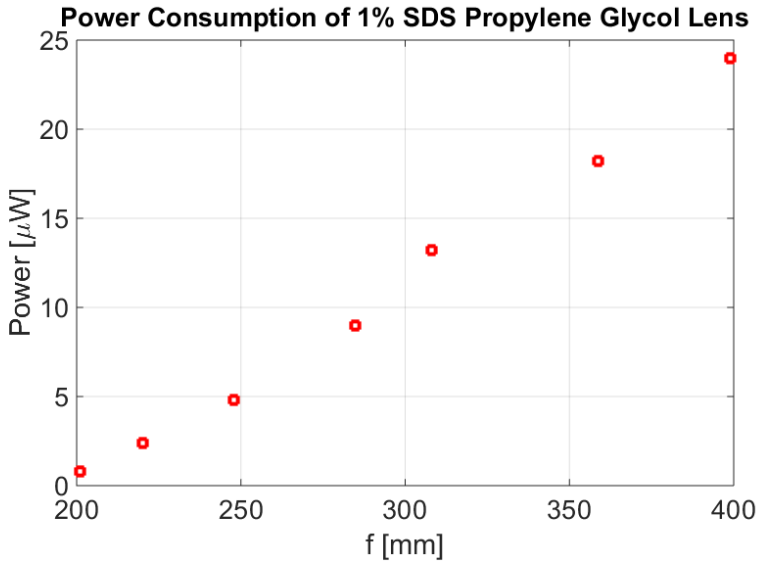

Figure 3-19 Consumed power of the liquid lens operating at DC voltage. The power is very low, due to the capacitive nature of the device. 25 μW of power dissipation is observed with continuous operation while tuning with -15 V. Figure from [27].

The devices operate with the lowest power using DC voltage actuation since the steady state power consumption is due only to leaked charge. However, at prolonged exposure to DC bias, the dielectric film will eventually take on enough charge to

affect the contact angle causing challenges with wetting reversibility and hysteresis. With our devices under DC operation near saturation at 15 V, a constant electric field has a strength on the order of 0.4 MV/cm. While this is well below the breakdown threshold of the parylene-HT (5 MV/cm) [114], it remains as a driving force to inject ions into the dielectric. To test the effects of inevitable charge injection, one glycol-based device was charged to saturation voltage of 24 V DC (0.64 MV/cm) before removing the probes that connected the power supply. After 30 minutes unconnected, the contact angle relaxed 25 degrees, marking a change in power of 2.6 diopters of the lens. Compare this rate of charge injection in parylene-HT to results from [76] with electrowetting on ITO / 1.3 μm parylene-C / 50 nm Fluoropel (hydrophobic coating). The electric field was only 0.29 MV/cm yet the same contact angle relaxation occurred within 60 seconds or less.

The advantage of using AC voltage to drive the lens actuation is that the alternating polarity of the voltage helps to eliminate charge injection that occurs from sustained DC bias. However, under AC voltage, the smaller sodium ions from the SDS are now part of the collection of ions building up at the dielectric surface during electrowetting. Thus we lose the advantage that the large dodecyl sulfate ion allowed and see bubble formation indicative of hydrolysis and device failure at 18 V_{rms}. The contact angle response of a glycol-based lens can be seen in Figure 3-20.

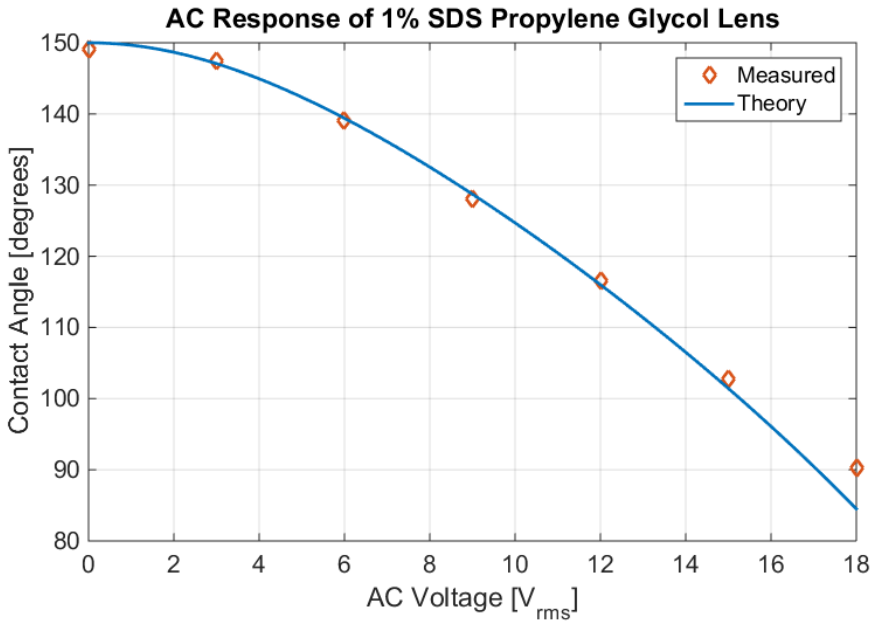

Figure 3-20 Comparison of measured and theoretical contact angle of a propylene glycol based lens operated with 100 Hz AC square wave voltage. This lens has a 370 nm thick parylene-HT layer. CAS begins to occur at 15 V_{rms}.

The contact angle measurement above can be compared to Figure 3-16 where the glycol lens was tuned with DC voltage. Note the dielectric thickness for the device in Figure 3-20 is 370 nm, compared to the 300 nm from the devices measured in Figure 3-16. Interestingly, the glycol-based lens tuned by AC voltage is able to surpass the CAS limit when tuned by DC voltage. This similar dependence on AC versus DC voltage is reported in [76], where AC voltages allow for further tuning before CAS sets in. Higher voltage tuning to experimentally investigate the CAS point for the glycol-based lens with AC tuning was not possible due to thin film breakdown and device failure. This challenge can be addressed by using ion sources where both cation and anion are large so that AC tuning can be reliable in low voltage electrowetting applications [92].

3.6 **Lens Quality**

It is important to quantify lens aberrations as a function of tuning. I worked with Kevin Dease and Robert Niederriter in the lens quality assessment, with the

former leading the data analysis and both assisting with optical setup. We characterized the lens operating in horizontal orientation (i.e. the normal to the lens parallel with the table) with a wavefront sensor on load from Dr. Robert McLeod and determined the RMS deviations from a perfect spherical wavefront and the Zernike polynomial coefficients. A spatially filtered and collimated 532 nm laser was used for the characterization. The beam has a diameter of 2.588 mm on its major axis and 2.327 mm on its minor axis, determined by a $1/e^2$ intensity threshold. The laser propagated through the glycol-based liquid lens and the resulting wavefront at the exit pupil of the lens was imaged onto a Shack-Hartmann µ-eye Wavefront Sensor (CLAS-2D with software from Lumetrics). The wavefront sensor measures the wavefront intensity and phase. To determine the RMS deviation from a sphere and Zernike coefficients, the phase data was masked with a 2.3 mm diameter circle. The mask eliminates edge effects and pixilation from the wavefront sensor. To verify the phase measurement procedure, a 200 µm pinhole was placed in the beam path and the phase of the wavefront was found to agree with theoretical predictions.

The RMS deviation from a spherical wavefront was calculated from the aberration function determined by subtracting a best fit sphere. The average values of the RMS deviation ranged from 88.98 nm at 0 V to 217.49 nm at 20 V. This result is comparable to previously reported values for RMS wavefront errors in electrowetting lens systems of 80 nm [21] and 211 nm [14] and in elastomeric lenses of 400 nm [115]. Berge et al. report wavefront error values of the similarly sized, commercially available Varioptic lens A316 of 30 nm to 90 nm over the full tuning range, disregarding tilt and focus Zernike modes [84].

The Zernike polynomial coefficients for third order spherical aberration were measured for two devices. The best-fit sphere was subtracted from the phase data and the resulting aberration function was fit to the Zernike polynomials. The third

order spherical aberration used for fitting is $6\rho^4$ - $6\rho^2$ + 1, where ρ is the radial distance normalized to the Zernike circle [104]. Figure 3-21 illustrates the normalized spherical aberration Zernike coefficient for each device as the lenses are tuned from a small radius of curvature toward an infinite (flat) radius of curvature. The average measured spherical aberrations range from -92.21 nm at 0 V to -17.68 nm at 20 V.

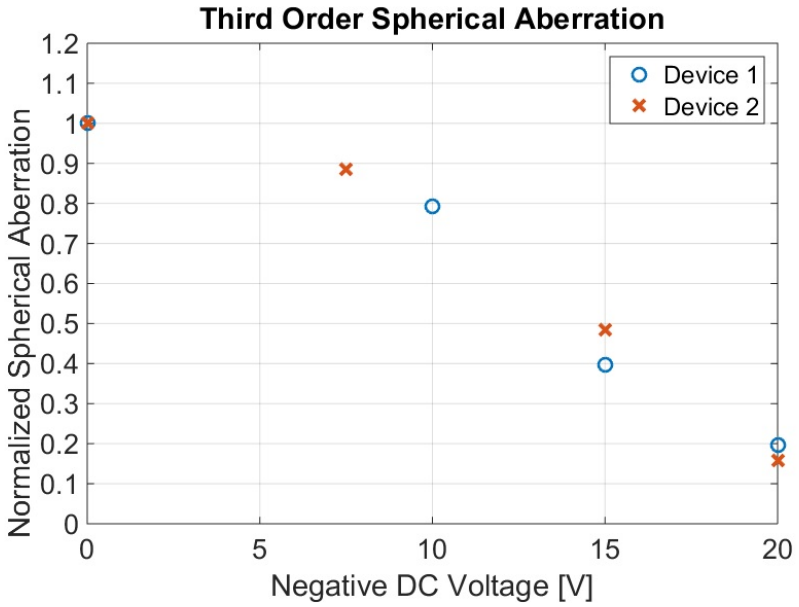

Figure 3-21 The spherical aberration Zernike coefficients values are determined by fitting the wavefront to the third order spherical aberration polynomial $6\rho^4 - 6\rho^2 + 1$. The wavefront is measured at various points while tuning the lens devices in the operating range between 0 V and -20 V. Both devices depict the trend of decreasing spherical aberration magnitude as the lens is tuned from maximum curvature toward flat.

The spherical aberrations grow smaller in magnitude as the lens is tuned from its highest curvature at 0 V toward a flatter lens profile as voltage is increased. This agrees with the general trend that lenses with shorter focal lengths have more pronounced effects from spherical aberration due to the higher lens curvature.

By taking advantage of the exceptional insulating properties of parylene-HT and the large ion size of SDS, we can enable reliable DC electrowetting on 300 nm thin films with low voltage tuning. The 15 V lens tuning is compatible with low cost voltage drivers and does not require a voltage transformer to integrate with

microsystems. Furthermore, the power consumption due to the leakage current during operation is reduced to tens of μW. These are important steps for integrating electrowetting lenses into microsystems that require low voltage such as endoscopy and low power draw such as battery powered mobile optical systems. Replacing water with propylene glycol as the polar liquid changes the sign of the lens power and alters the contact angle saturation point. A difference in 30 degrees in saturation angle is significant considering the only change in the system is that the polar molecule solvent carrying the ions is H_2O in one case and $C_3H_8O_2$ in the other. This indicates that contact angle saturation is influenced by interactions involving the polar material and not simply the ions within the material system. Further investigation of CAS for propylene glycol under AC voltage actuation experimentally confirmed a dependence on driving voltage type and saturation angle.

With an electrowetting lens operating in converging or diverging modes, we can now look at some of the applications of such a tunable lens. Chapter IV will investigate the variable focus lens for microscopy and microendoscopy.

CHAPTER IV – MICROSCOPY AND MICROENDOSCOPY APPLICATIONS OF ELECTROWETTING OPTICAL DEVICES

Variable focus optics were applied to microscopy, endoscopy and an optical shutter or switch. This chapter details the applications explored with electrowetting devices. The optical shutter uses a slightly different device and is still an ongoing study, so it is included in the Appendix. The microscope analysis was completed in collaboration with Kevin Dease, who calculated the magnification of the system and assisted with the optical setup. The work with the microendoscope was part of a much larger collaboration with the wonderful group from the University of Colorado Denver with students from the Center for NeuroScience and the Department of Bioengineering including Baris Ozbay, Greg Futia and Justin Losacco. Baris and Justin focused on the microendoscope design while my work was centered on integrating the variable liquid lens. The project is an ongoing collaboration between Professors Juliet Gopinath, Victor Bright, Emily Gibson and Diego Restrepo, with Robert Cormack leading the optical design.

4.1 **Electrowetting Microscope Demonstration**

The converging electrowetting lens with propylene glycol was used as an eyepiece in a basic, two-lens compound microscope setup. The resting focal length of this lens is 175 mm. We paired it with an objective lens with short focal length of 17 mm to greatly enlarge the image. The electrowetting lens is then tuned around the image point to bring the object into focus, as well as alter the total magnification of the system. A diagram showing the compound microscope setup is shown in Figure

4-1. The compound microscope with electrowetting eyepiece was used to image diatoms, which are single cell algae organisms on the scale of 10 to 100 μm.

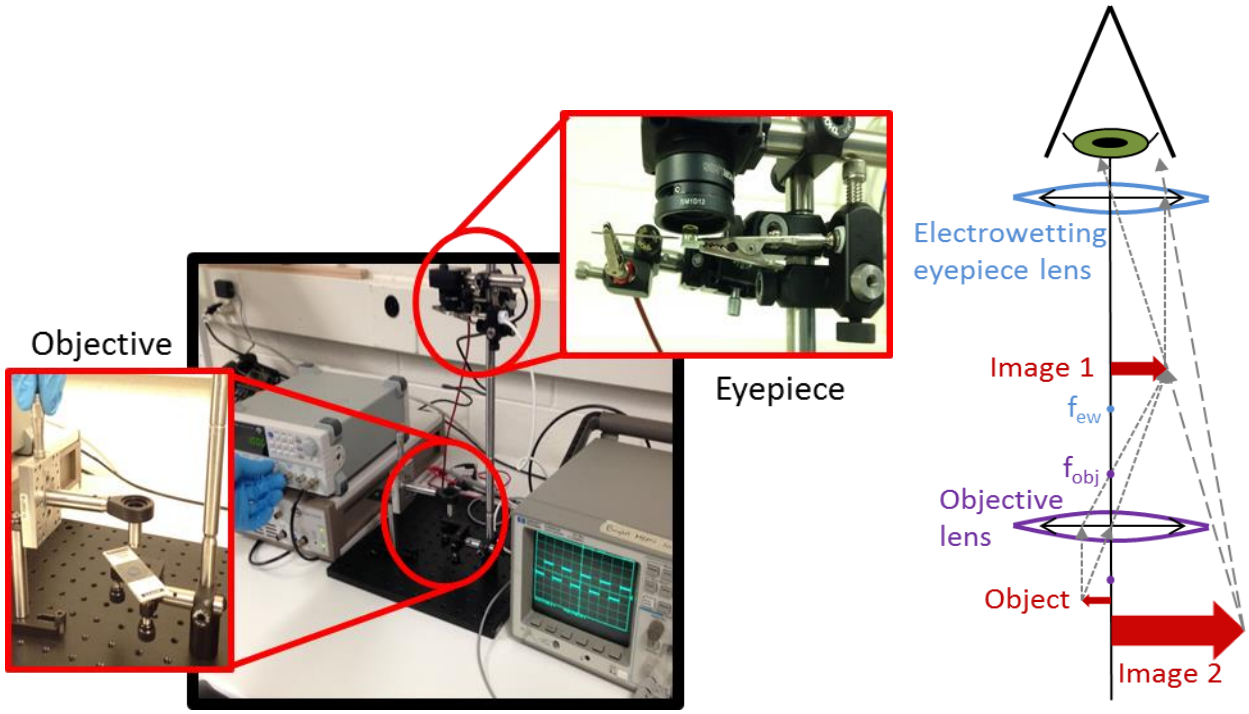

Figure 4-1 Electrowetting optical microscope setup. Left: Image of the microscope setup, showing the electrowetting lens replacing the eyepiece and the objective lens imaging the diatoms. Right: Diagram of a basic compound microscope setup used. A shorter objective focal length creates a larger image. The electrowetting lens focal length is tuned to change the overall magnification of the object.

The microscope's magnification change due to the electrowetting lens was measured and calculated by using both a ruler and an objective mask of known reference dimensions. First, the digital magnification of the camera is determined by photographing a ruler, counting the pixel width between millimeter line pairs and normalizing by the pixel pitch on the photodetector. An inherent magnification factor of 1.431 is calculated in this manner. Next, the microscope is used to image the reference target while keeping the electrowetting lens at 0 V. The number of pixels between known line pairs is again used to determine the magnification of the microscope. Without any applied voltage, the magnification of the system is 6.92. After applying 20 volts to the electrowetting lens, the image grows in size,

indicating an increased magnification. The new magnification is determined to be 8.19, an increase of 18.35% from 0 to 20 V applied.

Images taken by the camera in the microscope setup show the magnification increase while imaging the diatom samples, seen below in Figure 4-2. The lens used in this demonstration was slightly different, having a 1 μm thick parylene-C coating. Thus, the required voltage for lens tuning is increased, along with the acceptable voltage range for device operation.

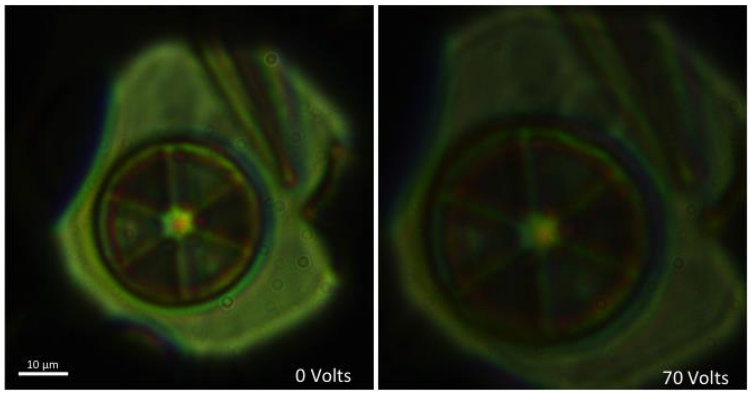

Figure 4-2 Diatoms imaged under microscope with electrowetting eyepiece. The electrowetting lens used in this example has the thicker, Parylene C based dielectric requiring higher voltage actuation.

The demonstration of an electrowetting lens within a microscope shows the potential for including variable, miniature optics in microscopy. Yet, the area where this technology shines is at smaller dimensions. With narrower diameters, it becomes difficult to use conventional mechanical systems for variable focus optics for close-up images. The added bulk of mechanical systems poses a challenge in both the axial and lateral dimensions. With a mechanical system, a large displacement length is needed to cover the focal depth seen in endoscope. Kuiper calculated that an imaging system based with a 4 mm focal length has to move a lens 0.17 mm to focus on objects at 10 cm, but an additional 20 mm to focus on objects at 0.5 cm [16]. These dimension restrictions and displacement requirements

create challenges for mechanical variable focus scopes for endoscopy. In Section 4.2, the integration of electrowetting lenses with a microendoscope is summarized.

4.2 **Microendoscope with Electrowetting Variable Lens**

The electrowetting group at CU Boulder is collaborating with Dr. Emily Gibson's microscopy group and Dr. Diego Restrepo's neuroscience group. Students on the project are Baris Ozbay and Justin Losacco. The goal is to integrate an electrowetting variable focus lens into a microendoscope device to enable axial scanning in a deep brain tissue imaging system. The microendoscope will be tested with mice for a proof of concept with the hope of extending to future clinical trials. One particular area of study is in examining hyper-excitable neural networks, such as those that fire during an epileptic seizure. Epilepsy has a high prevalence in society, affecting about 1% of the total population. The standard techniques to study neuron firing during seizures in living animals are electrodes implanted deep into the brain [116] as seen in Figure 4-3

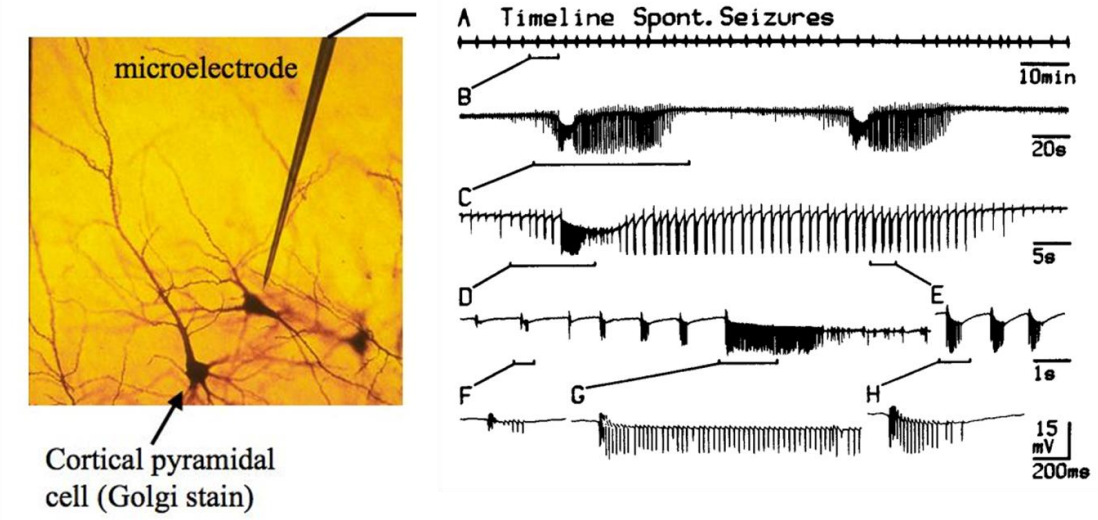

Figure 4-3 Electrode measurement of neural network. Left: Microelectrode implanted into the hippocampal slice of a rat brain. Right: electrical signals measuring hyperactivity over time. Figure from [116].

Electrical recordings cannot accurately determine which neuron is sending out the information, due to the size of the probes and uncertainty in placement. The probes gather all electrical signals in any neural activity that touches them, giving poor spatial resolution. Since neurons are extremely complex, electrical recordings do not give much information about what parts of the neuron are activating. As such, there is a push to optically examine the neurons during hyperactivity. Optical probing greatly increases the spatial resolution and can record many neurons at once [117], but cannot access deep into the brain due to light scattering of surface.

Studying deep brain activity is an important feature of optogenetics. Optogenetics is a technique that uses light interactions with neuron cell that have been genetically modified to express light sensitivity for regulating and monitoring neural activity [118]. However, the scattering of brain tissue and the bulky microscopy lenses limit imaging to the surface of the brain [22]. To study these deep brain areas, microendoscopes that penetrate into this deep brain tissue can be utilized. One obvious design requirement for microendoscopes is to minimize the size of the implantable optics in order to create the most minimally invasive procedure.

A solution is offered by optically probing the neurons through an implanted fiber-coupled endoscope, enabling deep brain imaging. The most promising systems use fibers and connections to head-mounted optics that allow the animal subjects to freely move around and not be head-fixed under a microscope. To image neural activity, fluorescent indicators are introduced in the brain of the specimen. GCaMP3 is a genetically encoded calcium indicator commonly used to image neural activity in animals [119]. See Figure 4-4 for an example of a head-mounted optical system for microendoscopy.

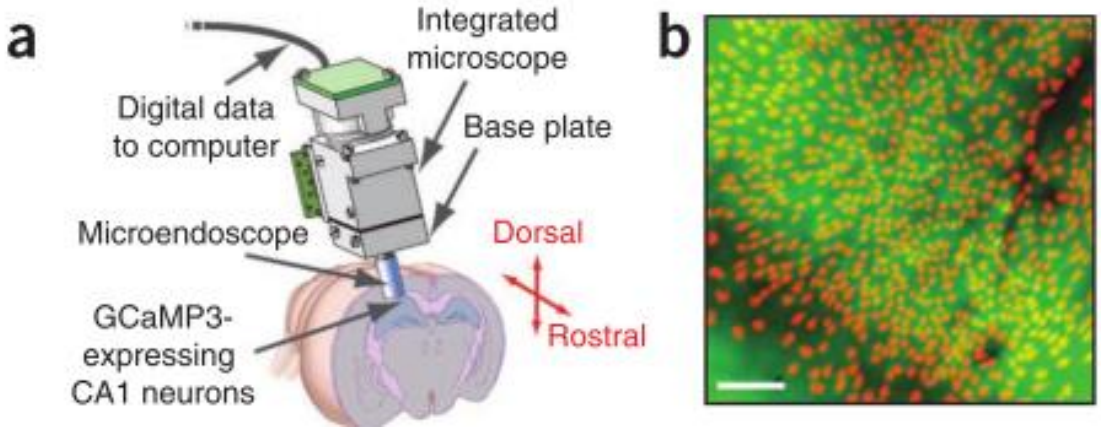

Figure 4-4 Optical endoscope targeting biomarker GCaMP3 expression in neural cells. The whole setup is head mounted for freedom of movement for the animal. The microendoscope is fiber coupled and implanted to image the calcium based fluorescent indicators within the neurons. Figure from [120].

The ideal implementation uses multiphoton imaging with a scanned laser to view brain tissue. Mechanical systems for scanning require large amounts of power, generate magnetic fields, and are not easy to miniaturize or integrate in a microendoscope. This presents a unique opportunity for electrowetting optics. With the low power consumption and compact footprint, electrowetting optics are a very good match for integration with a microendoscope. This allows researchers to gather information from larger volumes of the brain and precisely target specific subcellular structures like synapses.

The initial electrowetting microendoscope was developed by the group at CU Denver and uses a commercially available electrowetting lens integrated with solid lenses on either side and encapsulated with a fiber bundle within a 3D printed case [22]. The device can be seen in Figure 4-5.

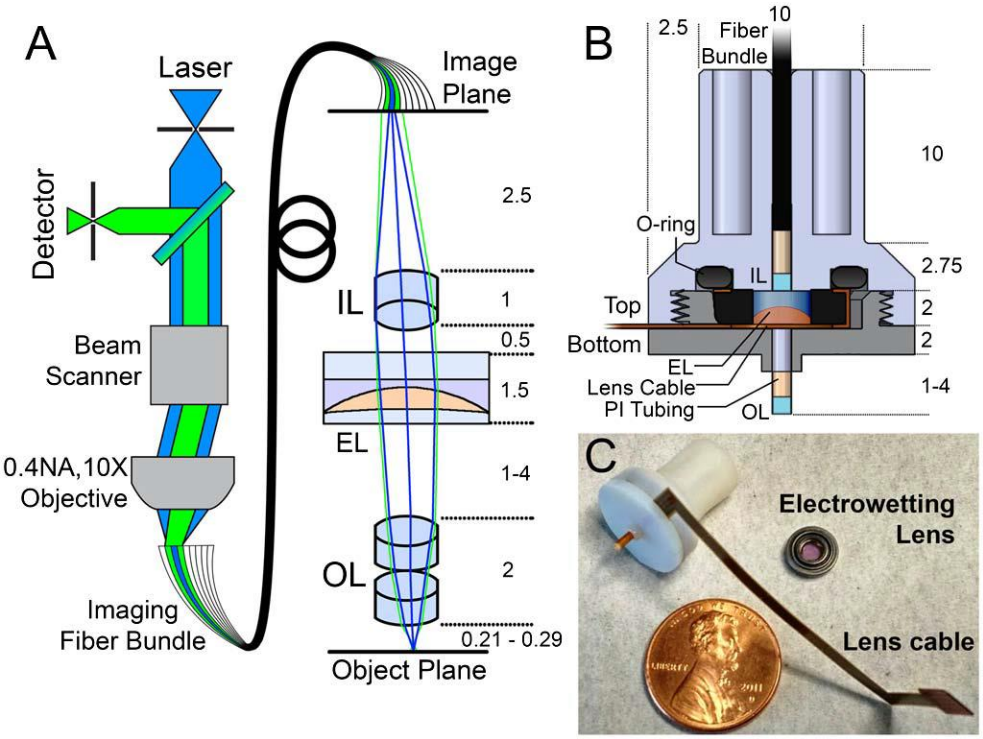

Figure 4-5 The prototype electrowetting based microendoscope. The device consists of an objective lens (OL), an electrowetting lens (EL) Arctic 316 from Varioptic, an imaging lens (IL), and fiber bundle coupled to a laser scanning confocal microscope. The fiber bundle and glass microlenses are aligned within a polyimide (PI) tube. Dimensions are in millimeters. Figure from [22].

This device was used to with a laser-scanning confocal microscope to optically section *ex vivo* mouse olfactory nerve fibers. The prototype has enabled optical depth scanning of deep brain tissue with variable focus liquid lenses for the first time [22]. The future clinical applications for this technology have enormous implications. Groups of neurons can be monitored for seizure initiation and the same optical system can be used to excite genetic proteins to precisely regulate neurons to stop the seizure before it happens. Alternatively, the optical system can be used for precision deep brain stimulation, which is already performed with electrodes for Parkinson's disease [121], depression [122], epilepsy [123], and others pathologies of the brain.

To integrate the custom electrowetting lens into their endoscope system, a slight redesign of the prototype is necessary. Firstly, given the size of the electrowetting

lenses, an optical relay has to be used such that the variable lens optics remains outside of the brain. To do this, a narrow, cylindrical shaped gradient refractive index lens (GRIN) lens is used to relay the imaging plane beyond the end of the bulkier variable optical component. The redesigned endoscope device schematic can be seen below in Figure 4-6.

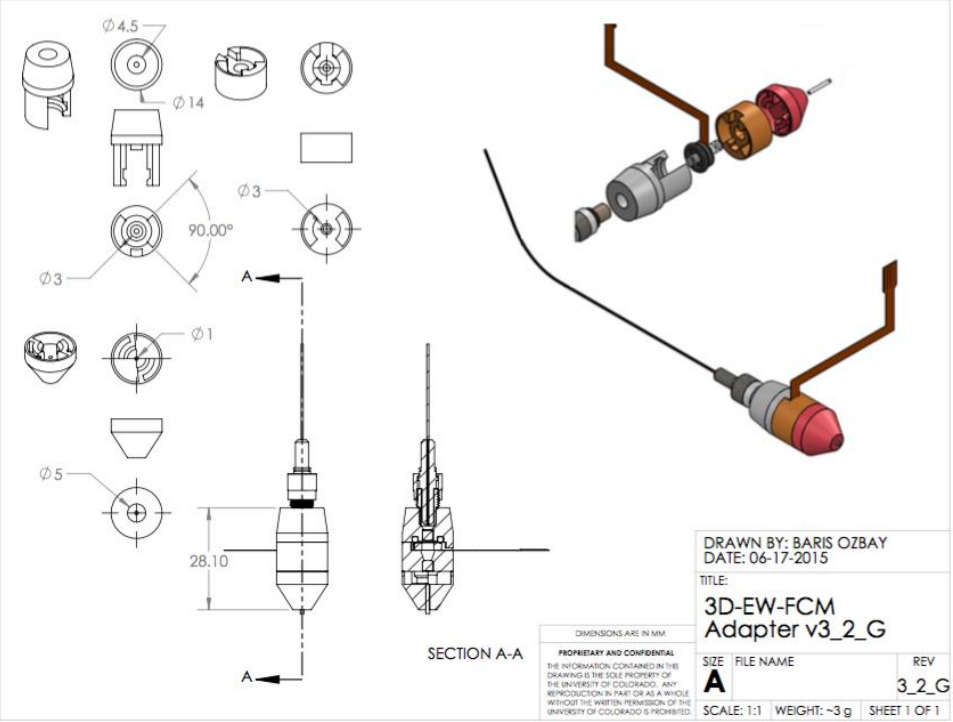

Figure 4-6 Schematic of the microendoscope design including GRIN lens. This lens redesign includes the electrowetting lens developed at CU fixed between two solid microlenses within a 3D printed capsule. A GRIN lens is used to relay the image from the endoscope tip. Figure courtesy of Baris Ozbay.

The three piece microendoscope is refitted to accept the electrowetting lenses developed in this work. Images of the electrowetting lens fitting into the 3D printed microendoscope including electrodes, solid lenses and fiber optic cable coupling can be seen below in Figure 4-7.

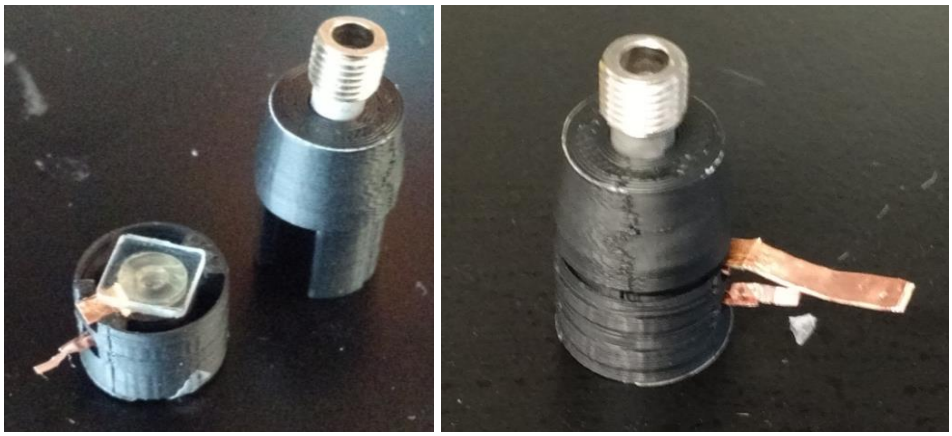

Figure 4-7 The 3D printed microendoscope design. The capsule includes two fixed glass lenses and the electrowetting lens encased with copper electrodes and the fiber optic coupler.

The microendoscope device is designed for imaging through a fiber bundle that is aligned and coupled to the solid and electrowetting optics via the packaging. The endoscope is tested with the fiber bundle, imaging a fluorescent source illuminated by a separate source behind a reference mask. The liquid lens is comprised of 1 wt% SDS water and dodecane oil. Images of the fluorescene through fiber optic bundle can be seen in Figure 4-8.

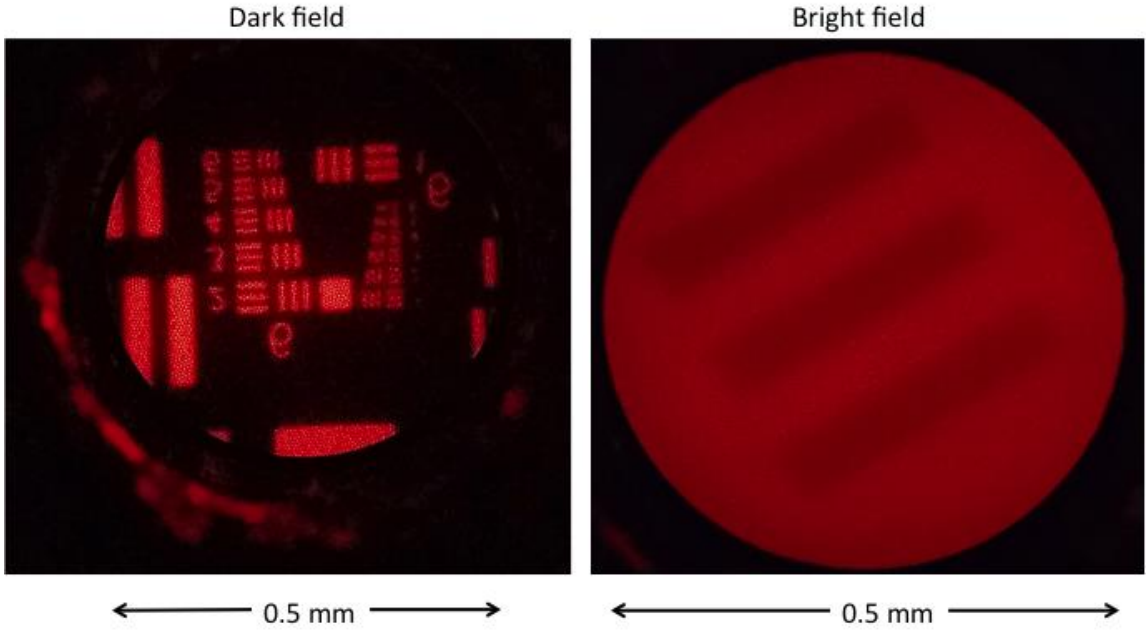

Figure 4-8 Images of a reference target through microendoscope. Single photon image data is taken by imaging a fluorescent target through a mask pattern with the electrowetting microendoscope device.

Visual inspection shows no significant image distortion. More rigorous study can quantify the aberration of the total system (see Section 3.1.3 and Section 3.6). Next, the electrowetting lens was tuned to alter the depth of focus while looking at one feature on the reference mask. Figure 4-9 shows screen captures taken from a video taken through the eyepiece of the fiber coupled system.

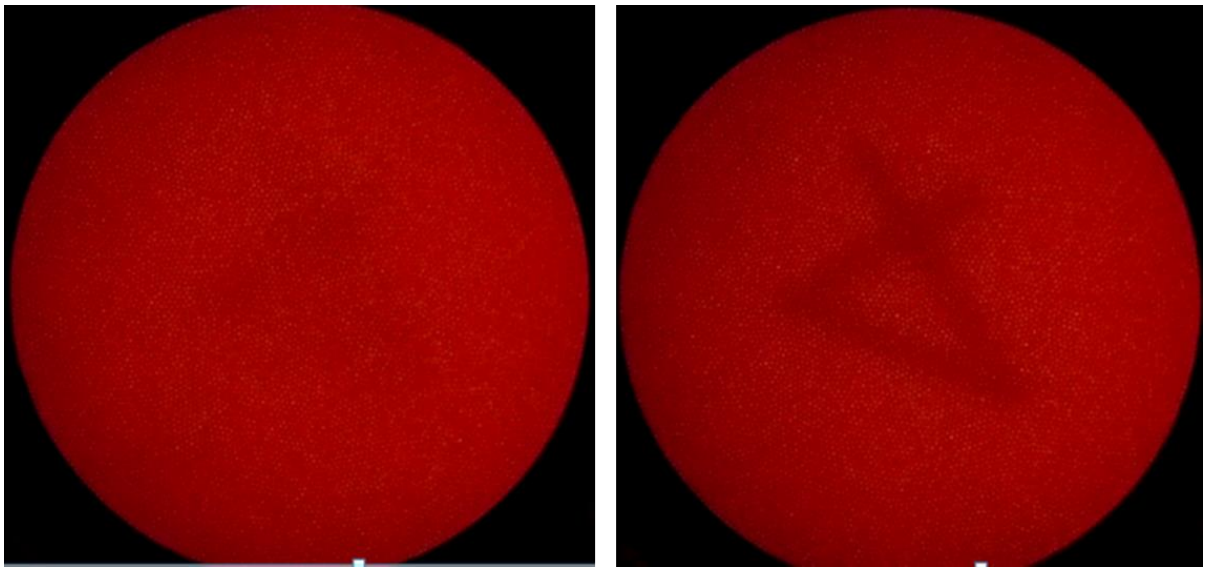

Figure 4-9 Images electrowetting tuning of reference target. The number "4" appears out of focus on the left, until 8 V are applied to the liquid lens device within the microendoscope. The lens changes its focal length to capture the feature in focus.

These images demonstrate the successful integration of the custom electrowetting lenses from Chapter III. The image quality remains high while tuning the electrowetting lens through optical powers of -43 m^{-1} to 0 m^{-1}. Electrowetting variable optics have been demonstrated to show great promise in the field of miniature microscopy and microendoscopy. Their miniaturization compatibility, high lens quality, and large focal length tuning range make for versatile and compact imaging solutions. Work in this collaboration is still ongoing, and the details of the next steps are included in Chapter VI.

CHAPTER V – ELECTROWETTING OPTICS IN THE INFRARED

This chapter investigates electrowetting variable optics in the infrared wavelengths at 1.5 μm, 3 μm and for thermal imaging between 8 – 14 μm. Robert Niederriter was integral in setting up the knife edge measurements. Soraya Terrab fabricated the prisms used for the infrared beam steering study and Omkar Supekar assisted with the beam steering measurements.

Recent advancements in infrared imaging systems have provided many applications in the defense, scientific, and consumer markets. Infrared imaging is valuable for persistent surveillance applications that cover the wavebands from visible to near-infrared (NIR, 0.7 – 1.0 μm), to shortwave infrared (SWIR, 1.0 – 3 μm) and midwave infrared (MWIR, 3 – 5 μm) [124-125]. Furthermore, there is interest in developing infrared optics for dual-band applications to improve imaging within dirty battlefield environments [126] and for maritime wide-angle / panoramic surveillance [127-128], as well as hyperspectral imaging to learn more details about a target [129].

5.1 **Infrared Spectrum and Ionic Liquids**

We have demonstrated electrowetting adaptive optical devices that have the potential to fit the needs of optical systems from the visible to the MWIR. This is a major advancement for adaptive optic technology based on liquid components, which are traditionally limited by O-H stretch vibrational resonances in the MWIR. Our technology is enabled by ionic liquids (provided by Solvionic), with transmission

from the visible through the MWIR. The devices demonstrated may have an impact on a broad range of application spanning thermal imagery to telecommunications. In addition, adaptive optical components can enhance automated machine vision and security systems, enabling versatility without moving parts in a compact footprint. The simple voltage control can be used with a feedback system to assist the precision active alignment of fiber coupling in communications systems. Free-space communication requires MWIR operation to avoid atmospheric distortion, and is vital for defense surveillance and communication where fiber optic cables aren't available. Furthermore, variable focus liquid lenses in the infrared waveband provide a nice alternative to emerging adaptive optics solutions such as polymer based spatial light modulators [130] which are polarization sensitive, and flat lenses, based on surface plasmon excitation that requires very high temperatures (900 °C) [131].

Electrowetting have become available commercially [84]. However, these optical devices have been limited to the visible and near infrared wavelength due to the predominance of aqueous liquids that absorb heavily beyond 1.4 μm due to vibrational resonance. For long wavelength operation, a change of materials is required. Room temperature ionic liquids (RTIL) are synthesized pairs of large, ionically bonded molecules that exist in liquid state due to asymmetrical loose packing of the molecules [132]. The bulky size of these ion pairs shifts the vibrational resonance away from the infrared waveband that is vital for communication and thermal imaging [95]. Ionic liquids have very good qualities for electrowetting applications, including transparency to the infrared spectrum, good conductivity, low vapor pressure that mitigates evaporation, and large ion size that can reduce charge trapping or leaking [92].

RTILs have been studied as a new type of soft material and solvent due to their ionic conductivity, extremely low vapor pressure and electrochemical stability [133].

Study of electric field actuation through electrowetting has proven that ionic liquids are a good alternative to typical aqueous liquids as the material properties of the ionic liquids alleviate the challenges of evaporation and degradation due to electrolysis [134]. Recently, ionic liquids have been demonstrated in electrowetting-based variable focus liquid lenses [12], but the devices were not characterized in the infrared. In contrast, this section demonstrates ionic liquid based electrowetting variable lenses and prisms at wavelengths of 0.54 µm, 1.55 µm, and 3 – 5 µm. The devices have the potential to cover the entire visible to MWIR spectrum, a major advancement for broadband liquid-based adaptive optical components.

It is important to identify the transmittance of the ionic liquid for the infrared wavelengths. An ATR scan of the ionic liquid transmittance as provided by the manufacturer is shown in Figure 5-1 [135].

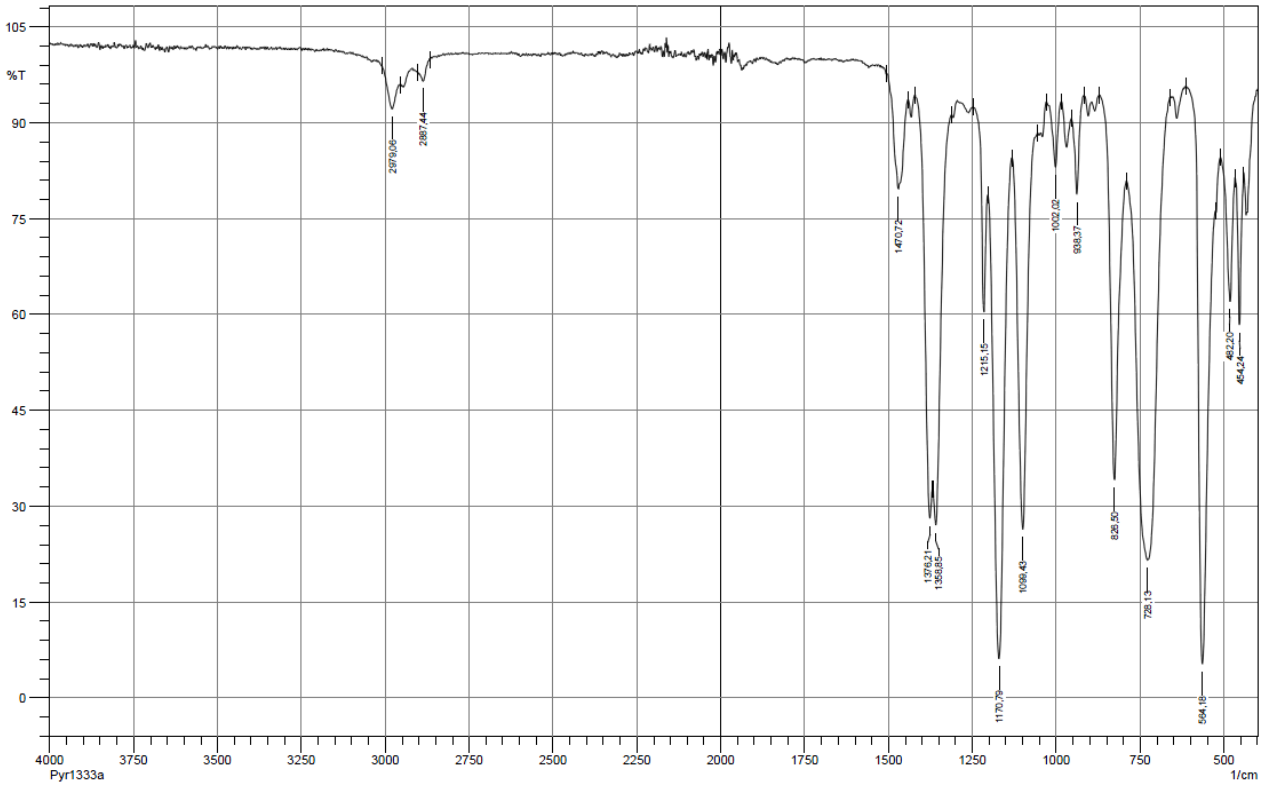

Figure 5-1 Transmittance of the ionic liquid in the IR lenses and prisms. Plot of N-Propyl-N-methylpyrrolidinium bis(fluorosulfonyl)imide provided by Solvionic [136].

The ionic liquid used in these experiments is N-Propyl-N-methylpyrrolidinium bis(fluorosulfonyl)imide from Solvionic (pry1333a).

5.2 Infrared Liquid Lens and Prism Fabrication

The electrowetting lenses and prisms are contained in glass tubes. Thin film electrodes, dielectric and hydrophobic coatings are deposited onto the inner sidewall of the cylinder in that order, respectively. These cylinders are then bonded to the substrate most appropriate for the waveband of operation. Finally, the lenses and prisms are filled with ionic liquid and dodecane oil via micro pipette. This basic electrowetting lens design is simple, compatible with standard microfabrication techniques and has been proven successful [15], [27].

Three electrowetting based optical devices were fabricated and tested to demonstrate curvature and tip-tilt tuning for wavelengths from visible through the infrared spectrum. Figure 5-2 shows schematics of the two lens designs and the prism design. In Figure 5-2(a), the visible / SWIR lens device is contained within a glass tube of 2.7 mm inner diameter and 4 mm in height. Figure 5-2(b) depicts the MWIR lens device with the same lens diameter, but with a shorter height of 1.5 mm in order to reduce the amount of liquid the infrared light passes through, which helps to reduce absorption loss. The prism depicted in Figure 5-2(c) has an inner diameter of 6 mm, a height of 10 mm and two separate electrodes on the inner sidewall to enable tilt control.

The common components for each design include a glass tube to contain the liquids and act as the sidewall substrate for the subsequent thin film depositions. The sidewall electrodes are sputter coated indium zinc oxide (IZO), deposited by DC sputter at an operating argon pressure of 8 mTorr. This pressure is chosen to create a mean free path in the argon of about 5.5 mm, a much shorter length scale than

the distance between target and substrate of approximately 15 cm. This enables a conformal coating of the thin film electrode such that it remains electrically continuous from the inside to the outside of the glass cylinders [99]. For the prism device, strips of Kapton tape are placed within the cylinder to mask the deposition and create two separate electrodes [26].

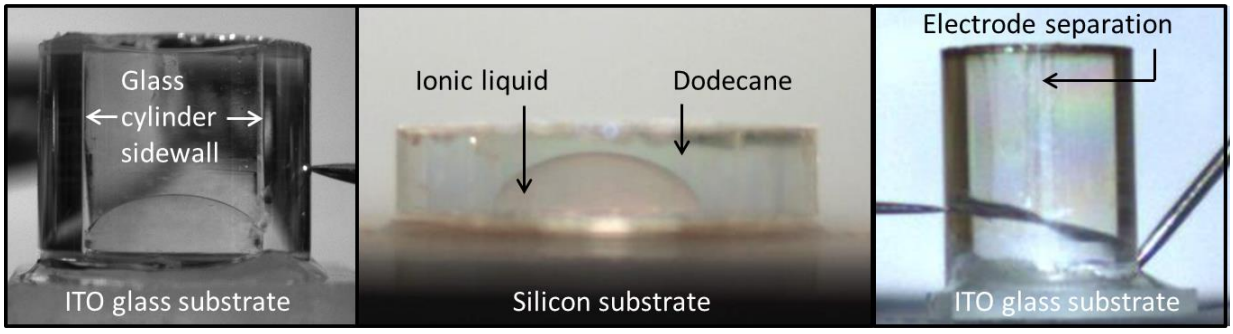

Figure 5-2 Images of the three devices fabricated and tested. (a) A 6 mm tall lens cavity with indium tin oxide (ITO) coated glass as the substrate can be used for visible through SWIR applications. (b) A 1.5 mm tall lens cavity with silicon substrate can be used for MWIR applications. (c) A 10 mm tall prism device with separate interior sidewall electrodes to enable selective tuning. Since light passes through the substrate and not sidewalls, the ITO glass substrate allows transmission for visible through SWIR wavelengths, while the silicon substrate allows transmission for the MWIR wavelengths.

Next, the devices are masked on the outer sidewall with Kapton tape and sent to VSI Parylene for the vapor phase dielectric parylene coatings. The lenses are coated with 300 nm of Parylene AF-4 while the prisms are coated with 1 µm of Parylene C. The devices are dip coated in a 1:20 solution of Dupont's Teflon AF1600 : Fluorinert FC-40 and cured at 125° C for 10 min, followed by a cure at 170° C for 25 min. The tape is removed to allow electrical connection to the sidewall electrodes.

The glass devices are bonded to appropriate bottom substrates for the respective operation wavelengths. The visible / SWIR lenses and prisms are bonded onto commercial indium tin oxide (ITO) coated glass with 4-10 Ω· cm film to electrically address the ionic liquid. The glass cylinders are placed upside down and Masterbond EP30-2 adhesive is applied on the bottom surface of the glass cylinders

before the ITO glass is aligned and pressed together with lens cavity, where it remains untouched to cure for 48 hours.

For the MWIR lenses, a different substrate is required since borosilicate glass does not transmit beyond the SWIR. A double side polished, undoped silicon wafer is used as the bottom substrate and infrared window, and is bonded to the glass, using SU-8 epoxy. Before the bond, electrical contacts must be made that will address the ionic liquid within the cylinder from the outside of the device. A 300 nm copper film is deposited onto the silicon by DC sputter and patterned by a lift-off process. The pattern creates a contact pad outside of the cylinder and traces a lead to the inner diameter of the cylinder, such that electrical connection is made to the ionic liquid without obstructing the optical window of the bare silicon substrate.

Since the silicon substrate is visibly opaque, the previous bonding technique with Masterbond becomes challenging to align. A new bonding process was developed to secure the cylinder to the substrate with photo curable SU-8 epoxy. First, a ring with dimensions that match the cylinders bottom surface is lithographically patterned over the bare silicon window. SU-8 2010 is spin coated at 3000 rpm, soft baked at 65° C for 3 minutes and 95° C for 3 minutes before an exposure of 150 $mJ \cdot cm^{-2}$. A post exposure bake is done at 95° C for 3 minutes before developing, resulting in a 10 µm thick film. The silicon substrate with the SU-8 ring is then exposed to oxygen plasma for 30 seconds in order to open reaction sites on the SU-8. Finally, a very thin layer of SU-8 2000.5 is brushed on the bottom of the cylinder before it is aligned over the ring on the silicon substrate. The two pieces are pressed together and hard baked at 150° C for 15 minutes to create a permanent bond between the glass and silicon substrate.

A micro-pipette is used to fill the lenses and prisms with ionic liquid (N-Propyl-N-methylpyrrolidinium Bis(fluorosulfonyl)imide, pyr1333a from Solvionic) and the non-polar oil (dodecane, Sigma Aldrich). The liquids are filled to the top of the

cylindrical cavity and a 170 µm glass cover slip is placed on top to prevent evaporation of the dodecane oil.

5.3 **Experimental Setup for Infrared Characterization**

The optical setup used to measure the focal length performance of the lenses is depicted in Figure 5-3. We measured the beam size and divergence angle after the electrowetting lens using a scanning knife-edge technique.

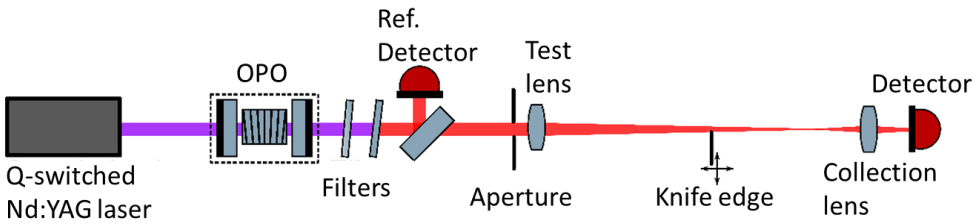

Figure 5-3 Lens focal length measurement schematic. SWIR and MWIR light was generated using a periodically poled lithium niobate (PPLN) optical parametric oscillator (OPO) pumped by a Q-switched Nd:YAG laser. Filters after the OPO isolated the beam at either 1.5 or 3 µm. The lens under test was placed in the beam and photodetector measured the power transmitted after a scanning knife edge. A reference detector was used to compensate for OPO power fluctuations. An aperture placed directly before the lens under test restricted the laser beam to the lens diameter.

The near- and mid-wave infrared light is generated using a periodically poled lithium niobate (PPLN) optical parametric oscillator (OPO; Mg-doped lithium niobate crystal with fan-out poling periods between 27.5 µm and 32.5 µm; HC Photonics), pumped by a Q-switched Nd:YAG laser (400 ps pulse duration, 500 Hz repetition rate; Teem Photonics PNP-M10005-130, PowerChip NanoPulse). The OPO is adjusted to resonate at the near-infrared signal wavelength of 1.5 µm and the mid-infrared wavelength of 3.0 µm, but can be tuned by adjusting the position of the fan-out PPLN crystal. Filters are used to isolate either the 1.5 micron signal, or 3 micron idler.

The light is passed through a beam splitter where a small portion is sent to a reference photodetector based on lead selenide (DSS-PSE020T from Horiba

Scientific). The reference detector is used to monitor fluctuations in the laser power in order to compensate for these drifts. The remaining infrared light is sent toward the electrowetting lens. An iris is placed before the liquid lens to match the incident beam to the lens aperture of 2.7 mm.

To measure the focal length of the infrared lens, the beam width at the lens and the divergence angle of the light after the lens are measured. A razor blade is mounted to precision motorized translation stages configured for two axis scanning. At an initial position along the axis of light propagation (z-axis), the razor is scanned across the beam width (x-axis) in 200 μm increments. At each interval, the fraction of the light that is not blocked by the razor is collected on a photodetector (lead selenide). After the razor is scanned across the entire beam width, we plot the ratio of the photodetectors' power data as a function of knife edge position on the x-axis, as seen in Figure 5-4(a). The data are fit with an error function: $y = P_0 + a * erf((x-x_0) / w)$ by the method of nonlinear least squares, where y is the fit function, P_0 is the baseline power, a is an arbitrary amplitude constant, erf is the error function, x is the knife position, x_0 is the initial knife position, and w is the beam width. The data is averaged to reduce noise.

The fit provides the beam width at a specific point on the z axis. After multiple measurements at different values of z, the beam width versus position can be plotted and line fitted, yielding the divergence angle of the beam, as seen in Fig. 4.4(b). To further reduce noise, the entire procedure of measurement and fit extraction at each knife position in x- and z-axis is repeated six times and averaged. With this knife edge method, the focal length performance of the tunable lenses is measured at 1.55 μm and 3 μm wavelengths.

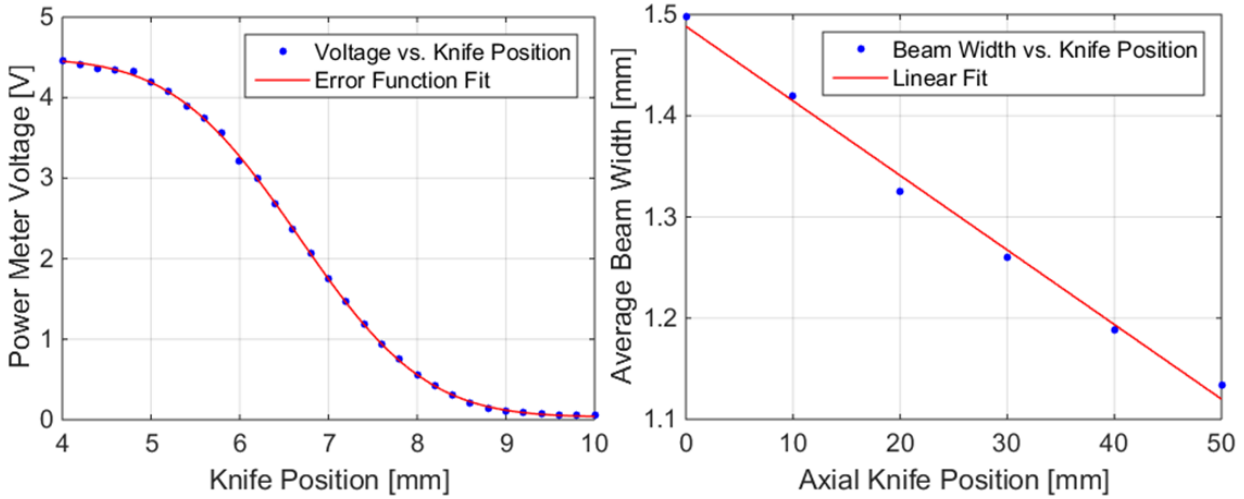

Figure 5-4 Knife edge measurement and fit data. (a) A representative of the data acquired directly from the knife edge power measurements. Detector voltage is plotted against knife position across the width of the beam. Fitting the integral of a Gaussian (an error function) to the data allows for the extraction of the beam width. In this example, the measured beam width is 1.358 mm and is one of the six measurements averaged to produce the beam width at knife axial position of 20 mm in the adjacent plot. (b) The extracted beam widths for each axial knife position is then fit to a line to determine the beam divergence. The slope of the linear fit gives a measurement of the divergence in radians. In this case, the beam divergence is measured to be .0074 rad.

The experimental setup for measuring the prism steering performance can be seen in Figure 5-5. Infrared light from a 1.55 μm laser diode is collimated and passed through the electrowetting prism. An indium gallium arsenide detector is attached to two motorized translations stages stacked in an x-y configuration directly below the laser diode and electrowetting prism. The detector is positioned such that the incident optical power on the detector reaches its peak value. This initial x- and y-position is recorded as the baseline from which all other steering positions are derived. As the liquid prism interface tunes with applied voltage, the infrared light starts to refract from the liquid interface at an angle governed by Snell's Law. The detector is then repositioned to peak out the signal once more, and the total x- and y-position displacement is recorded. This value of the displacement and the vertical distance between the prism interface and the detector are used to calculate the total steering angle with trigonometry. A camera images the liquid interface in order to measure the apex angle of the prism while it is actuated.

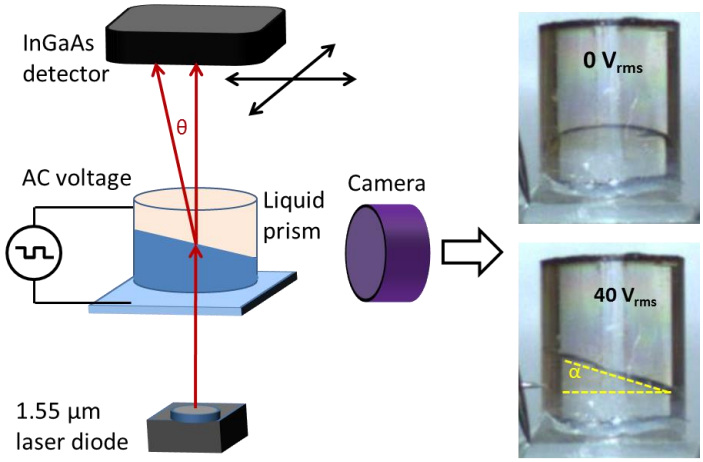

Figure 5-5 Infrared beam steering setup. 1.55 µm laser diode light is sent through the ionic liquid prism and measured by an InGaAs photodetector. The detector is mounted on two axis precision translation stages that move the detector to track the beam deflection. As the voltage is applied, a camera images the side perspective of the prism and the liquid apex angle is measured with imaging software.

5.4 **Lens and Prism Performance in Infrared**

The knife edge setup seen in Fig. 4.3 is first tested without any lens in order to determine the inherent beam divergence of 7.4 +/- 0.3 mrad. Next, a lens with a fixed focal length of 75 mm is used as the test lens, in order to check the procedure. The experimental procedure found the focal length of this lens to be 73.66 +/- 1.89 mm at 1.55 µm wavelength. Next, the lenses for visible through MWIR were measured by the scanning knife edge technique, making sure that data points were collected outside the Rayleigh range. The dioptric power results of the liquid lenses for visible, SWIR and MWIR wavelengths are shown in Figure 5-6. The liquid interface radius of curvature tunes from 1.68 mm to approximately 12.5 mm with 32 V DC before contact angle saturation halts all further tuning. Contact angle saturation is pervasive in almost all electrowetting experiments and acts as a limiting phenomenon that prevents the liquid contact angle from further tuning, regardless of increased applied voltage [76].

Another interesting observation is that the lens power increases with the wavelength. This signifies that the refractive index contrast between the two liquids increases with wavelength, creating a lens with higher optical power. The liquids have different dispersion characteristics. As the liquids' refractive indices change as a function of wavelength, different lens behavior is expected. Interestingly, the measured drift in the ratio of refractive index (as determined from the measured lens performance) from visible to infrared is relatively small, from 1.016 at 588 nm to 1.0371 +/- 0.0023 at 3000 nm. This refractive index contrast changes of about 2% is enough to change the starting lens optical power from 9.5 diopters to 22 diopters between visible and SWIR, respectively.

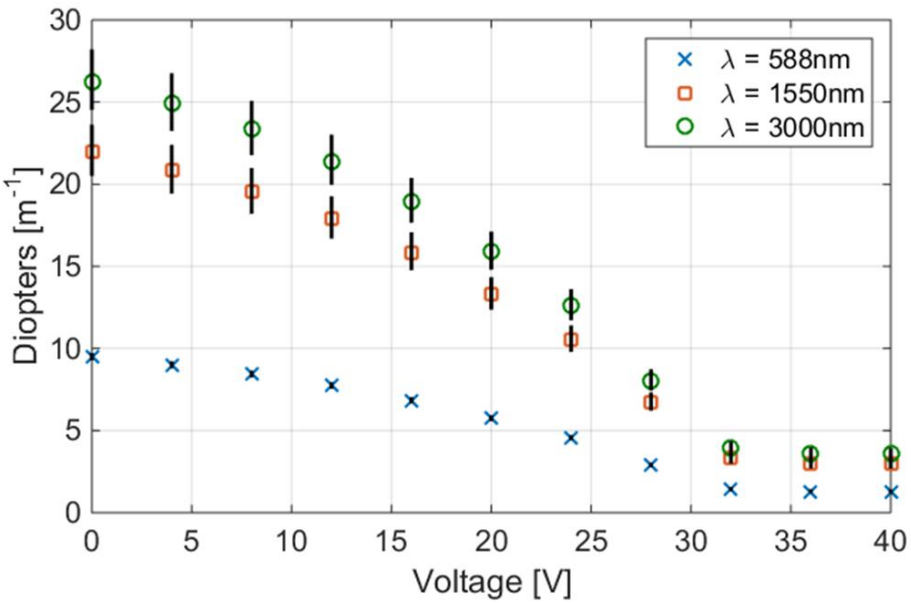

Figure 5-6 Lens power of the ionic liquid based lenses vs DC applied voltage. Contact angle saturation occurs at approximately 30 V. Error bars accommodating the propagated error from the knife edge measurement are included as the black vertical lines.

The refractive index contrast between liquids also determines the total steering in the prism device. Figure 5-7 shows the results of beam steering with the prism device from Figure 5-2(c) for both sidewall electrodes. The steering angle of light

passing through the prism reaches 0.58° with 40 V_{rms}. While this range is modest, it can be improved with a liquid pair with higher refractive index contrast and additional optics after the prisms.

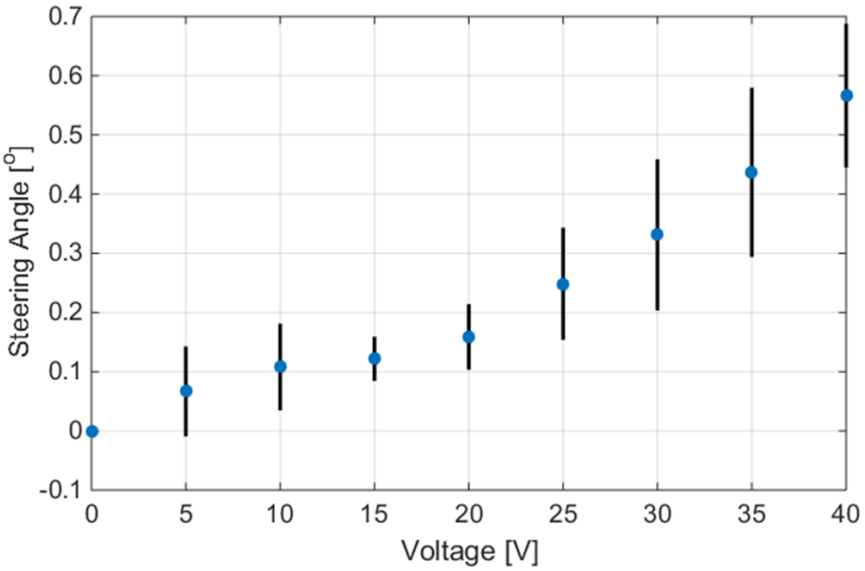

Figure 5-7 Measured steering angle from the ionic liquid prism for 1.55 μm light. The black lines represent the 95% confidence interval determined from the six repeated measurements. The steering angle was determined from the distance traveled by the detector and the vertical distance between detector and prism liquid interface.

5.5 **Long Wave Infrared Applications**

Transmission for the thermal imaging camera is less important at any particular frequency, but more so for the total waveband of light for which the detector is sensitive. While the transmittance levels of the ionic liquids are poor for this length of lens, they do show potential transmission at this waveband. With microfabricated lenses and arrays with thinner lens path lengths like 300 μm [23], the transmittance for the pyr0411c is above 50%.

A bolometer based thermal imaging camera from DRS Technology (Tamarisk 320) is enclosed in a pinhole box, with an aperture the size of the liquid lens diameter. The lens from Figure 5-2(b) is filled with the ionic liquid and dodecane and placed over the pinhole. The distance from the electrowetting lens to the

camera's fixed germanium lens is selected using the thin lens equation for two positive lenses. The two lens imaging system captures pictures of a soldering iron object. A demonstration of changing focal depth in the thermal image can be seen in Figure 5-8.

The quality of the thermal images appears grainy because the size of the microbolometer array is larger than the diameter of the lens, so the light only strikes a small portion of the bolometer pixel elements. This imaging set up is not optimized for quality, yet the unprecedented ionic liquid based variable lenses for thermal imaging applications is demonstrated from 8 – 14 μm. With further engineering, the prospect of using variable ionic liquid lenses to replace conventional and expensive LWIR optics has far reaching implications as these type of thermal imaging systems become smaller and more prevalent.

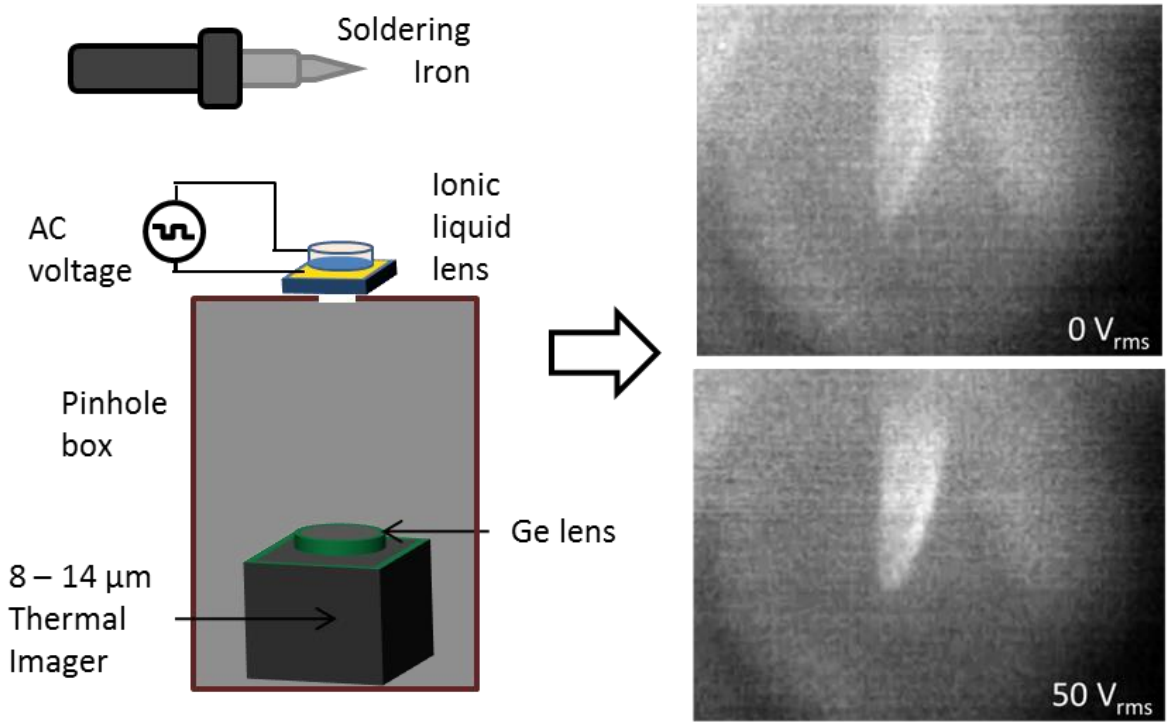

Figure 5-8 Images of the tip of a soldering iron through the ionic liquid based lens. Images were taken by a bolometer based thermal imager. Post processing was used to adjust the contrast in order to make the focusing effect easier to see.

In conclusion, we have demonstrated the potential for ionic liquid based electrowetting variable optical components to be used from the visible to mid wave infrared. Moving the proven technology of electrowetting optics into the infrared waveband opens the door to a vast number of applications ranging from surveillance to security and consumer imaging systems and telecommunications, both in the SWIR and MWIR ranges. It is important to continue developing cost effective optical components to make this technology more accessible to developers and consumers. This work represents a proof of concept for using ionic liquids for variable liquid optics over an infrared range of wavelengths.

CHAPTER VI – CONCLUSION AND FUTURE WORK

This research on electrowetting variable optics has covered many areas of applied electrowetting by developing liquid lens and prism devices. The success of these devices comes from careful design consideration including high quality dielectric material, thickness optimization, large ion selection, and non-traditional electrowetting liquids. Careful study of these factors enables beneficial developments in electrowetting lenses including low voltage and low power lens tuning and new wavelengths of operation.

6.1 **Contributions to Electrowetting Optics**

This dissertation presents several unique contributions to electrowetting variable optics research by expanding lens operation through use of new applications and judicious lens design. Section 3.1.4 describes for the first time how electrowetting lenses can be used for phase modulation, as modeled by [7]. Demonstration of this piston control shows over one full wavelength of phase delay, showing a proof of concept for electrowetting variable optics to be utilized for phased array elements [21]. Section 3.5.2 demonstrates successful implementation of non-aqueous electrowetting liquid lenses, enabling a converging lens mode based on material selection [27]. Chapter IV shows a proof of concept for variable liquid optics to be integrated into miniature optical systems for microscopy and microendoscopy. Finally, Chapter V describes the development and optical characterization of liquid lenses and prisms [26] in the infrared wavelengths. This

extension of operation into longer wavelengths is unprecedented in electrowetting optics, and shows great promise for this technology to be further integrated into all kinds of imaging systems from the visible through the infrared.

6.2 Future Research in Electrowetting Optics

The work presented in this dissertation has opened to door to many possible options for future exploration in this area of study. On the applications side, more work is needed to fully integrate the electrowetting lens into microscopy and microendoscopy devices. On the fundamentals side, further study is needed for dielectric properties and ion transport through thin films during electrowetting. This is the number one limiting challenge for electrowetting optics – device lifetime and tuning reliability are directly related to how well the dielectric can resist charge infiltration over constant cycling. Better modeling and more experimentation for this challenge are both worthy areas of investigation. The subsections below detail some of the future research in electrowetting optics that can follow from this thesis.

6.2.1 Continued integration for microendoscopy

One obvious segment of future work is in finalizing the integration of the electrowetting lenses into the microendoscope device from Section 4.2. A basic proof of concept imaging a fluorescent sample does not provide a full demonstration of the potential for electrowetting optics in microendoscopy. The ideal system design includes multiphoton imaging and laser scanning in the depth and lateral dimensions, made possible by an integrated lens and prism element [26]. The packaging and solid / liquid lens integration with fiber bundle is equipped to handle more enhanced imaging and live mice specimens expressing GCaMP3, yet the test of the device should go in increments. The next step includes adding a gradient refractive index (GRIN) lens to the distal end of the lens system (as shown in the

design in Figure 4-6) which becomes the implantable portion of the optical system. The GRIN lens acts as an optical relay, sending the imaging plane into the deeper part of the brain. The next step after GRIN lens integration is to image GCaMP3 expression in live tissue samples to determine resolution and further understand any limitations to the optical device. Finally, the device can be mounted onto a live animal for imaging over an extended period of time, typically weeks. To study brain response to hyper-excitability, a seizure can be induced in the mouse and the GCaMP3 can be tracked to further understand neural activity at a cellular and subcellular level.

6.2.2 Expanded modeling for optics

The electrowetting model presented in Section 2.3.4 provides a basic simulation of electrowetting on thin film dielectric and hydrophobic coating, with limited selection of liquids and no optical analysis. This model is a good groundwork for electrowetting design, yet can be improved to help predict optical performance and include more complete modeling for material properties. Below is a list of improvements:

1) Expand the selection of liquid materials by using the interfacial energy data from the electrowetting literature.
2) Calculating the expected optical power of a lens formed by these liquids. This requires data about the refractive index of each liquid material.
3) Include transmittance through the lens over various wavelengths.
4) Include empirically determined saturation points for liquids from the literature.
5) Add in calculations for electrowetting prism angle and steering.

These improvements to the model would increase its utility as a tool for liquid lens optical design. Including many more liquids and their optical properties would give a much better representation of the design space, allowing further engineering of these variable liquid lenses and prisms.

6.2.3 Study of ALD for ionic barrier

The primary challenge of applied electrowetting devices is to increase the reliability and lifetime of the devices. While hundreds of thousands of cycles have been demonstrated in lifetime analysis without degradation [137-138], a constant applied voltage even on the high quality parylene-HT results in charge trapping and device hysteresis after 6.5 hours [87]. This is attributed to both thin film quality as well as ion size [90], [92].

ALD has been shown to be successful as an electrowetting dielectric [51], yet its slow deposition time caters to ultra-thin films. Films on the order of a few nanometers are typical, yet will have a very large capacitance, which affects the RC charging time of the electrowetting system, thereby decreasing the response time. Perhaps an ultra-thin ALD layer can be used as an ionic barrier on a more standard dielectric like parylene. To test the capability of ALD acting as an ionic barrier on a porous dielectric, a brief study and experiment was performed. Figure 6-1 shows the basic experimental setup for testing leakage current through SU-8.

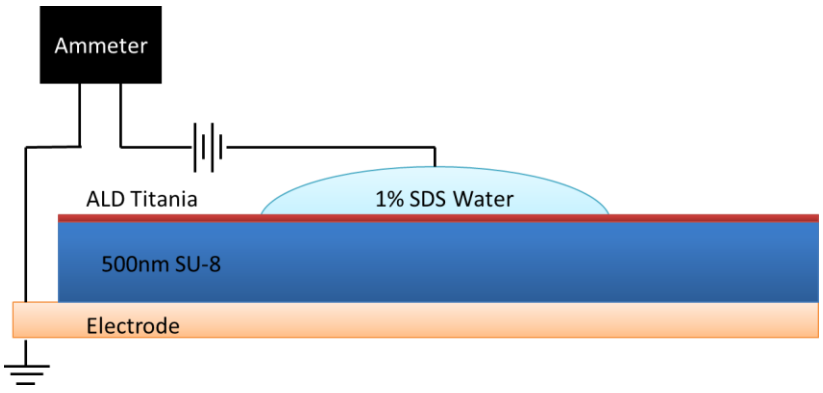

Figure 6-1 Experimental setup for ALD ionic barrier test. Various thicknesses of ALD Ti_2O_3 were deposited onto 500 nm film of SU-8 and tested for leakage current.

The experiment was to see if barrier layers of ALD titania helped prevent ionic leakage current through the SU-8. Being a cross-linked polymer, SU-8 is a porous material and water containing the ions easily penetrates the dielectric. When ALD barrier layers are added, the voltage potential required to get current spikes increases.

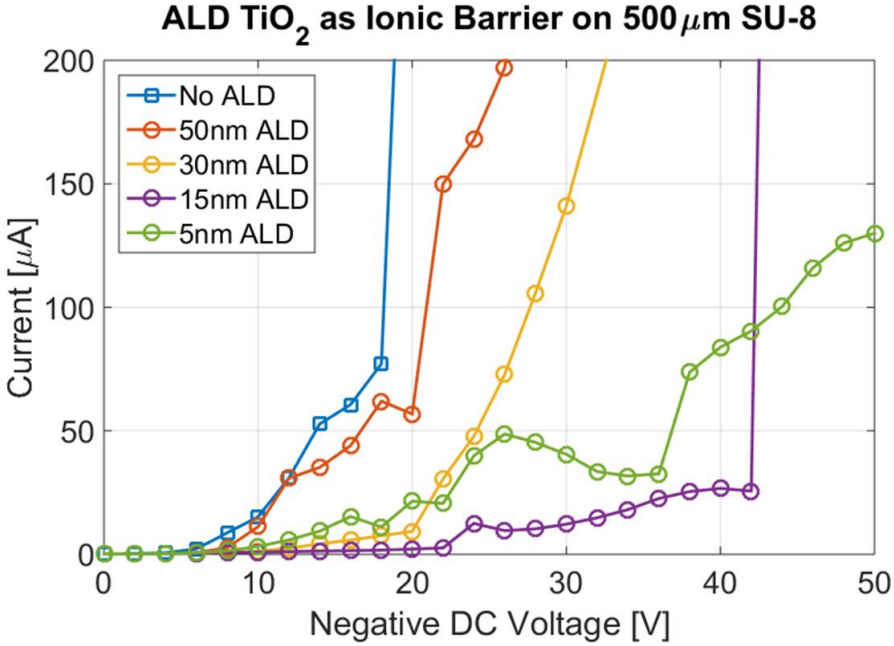

Figure 6-2 Preliminary data for ALD as an ionic barrier. The I-V curve shows the current spikes at particular voltage potentials, indicating ion penetration though the dielectric and microshorting. This represents a single data set and is not conclusive.

The data plotted above comes from a single data set and therefore is not conclusive in any rigorous scientific sense. Yet it does show that maybe there is trend associated with the ALD barrier layer and leakage current. Interestingly, the *thinner* ALD layers provided the better protection for this sample set. This is enough in incite my curiosity and invite future study into this area, as dielectric quality and charge infiltration remain the most challenging areas of practical electrowetting.

6.2.4 Investigation of non-aqueous liquids

The success of room temperature ionic liquids with electrowetting optics presented in this dissertation certainly warrants further study in this area. Proper optical characterization of the transmittance of various ionic liquids and nonpolar oils through the entire waveband from 0.350 – 15 μm would really provide the necessary data to design for applications which might combine visible and infrared for hyperspectral imaging. The ionic liquids have the additional benefit of having large molecule sizes which relates to large ion sizes. This can help prevent ion permeation through the dielectrics, helping to increase reliability and possibly lifetime of devices which use ionic liquids. Finding an optimal ionic liquid material for long wave infrared would truly be a great innovation, as the solid optics made from silicon, germanium, and chalcogenides are expensive.

Looking back at the experiment on CAS from Chapter III, propylene glycol and water exhibited drastically different CAS points. Interestingly, the exact same lens device with different electrowetting liquids causes contact angle saturation to occur at a much earlier angle – 110° for propylene glycol versus 78° for water. Dodecane is used in both trials. Since the same ions in the same concentration are used for both liquid systems, this indicates either that at least one driving force of CAS is independent of trapped charge, or that the solvent plays a role in injecting charges into the dielectric.

Some differences between water and propylene glycol that could contribute to this discrepancy are: conductivity, ion mobility, molecular weight, the polar component of their surface tension value, and the work of adhesion force that holds like molecules together. Since the ion source and concentration are equal and the parylene-HT dielectric resist charge injection, it seems unlikely that this drastic difference in CAS is due to trapped charge alone. The differences in material properties suggest that material interactions between polar liquid and non-polar

liquid can have a large effect on CAS. These observations support theories that attribute CAS to displacement of charged polar material into the non-polar medium, such as micro-droplet ejection or Taylor cone formation at the three phase contact line that could cause a screening effect on the electrowetting response [76]. It is interesting to note the power consumption of both liquids, as seen below in Figure 6-3.

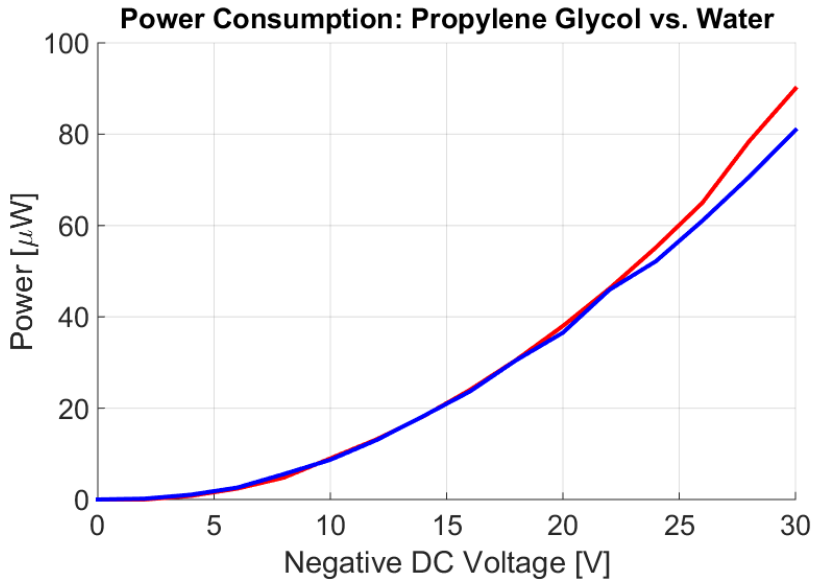

Figure 6-3 Comparison of power consumption of both liquid systems. Minimal leakage current is seen when using Parylene HT, evidence of the high quality of the dielectric.

The only difference in the two systems is the conductivity of the polar liquid. 1% SDS water has a reported conductivity of 877 μS/cm and 1% SDS propylene glycol has a reported conductivity of 31.1 μS/cm [92]. This would seem to indicate that conductivity, or rather, ion mobility, within the polar liquid play a role in the onset of CAS. Perhaps CAS is a function of rate of charge building up at the surface of the polar liquid compared to rate of charge leaking through the dielectric. Again, more analysis needs to be done here.

Suppose the current density through the liquid does affect CAS. The rate at which charges from the electrode in the polar liquid reach the contact line begins to

lag behind the rate at which charges leak through the dielectric, or are ejected from the contact line. The rate of charges flowing to the contact line (i.e. the current density through the polar liquid) is a linear dependence on the applied voltage, as the conductivity and mobility of the polar liquids remain constant. However, the rate of charges leaking through the dielectric (or being expelled in microdroplets or Taylor cone) could be exponentially related to the applied voltage. The total leakage current density through the dielectric is limited to the current incident on the surface of the polar liquid. Thus, the exponential nature of the leakage current is limited to equal the linear current incident on the surface. As such, once the exponential leakage current begins to match the current incident on the surface, the number of charges building up on the liquid surface would begin to taper off until the leakage current matches the incident current, allowing no more charge to build. This is consistent with the onset of CAS and full CAS.

These experimental observations certainly motivate additional study into the effects that liquid materials have on contact angle saturation points. This is a non-trivial problem to solve, as evidenced by the lack of a formal theory accepted by the electrowetting community as of June 2014 [75]. The community as a whole would greatly benefit from a thorough explanation of the phenomenon, as it would allow much better design and modeling of electrowetting systems.

REFERENCES

[1] G. Lippmann, "Relations entre les ph´ enom` enes ´ electriques et capillaires," *Ann. Chim. Phys.,* vol. 5, p. 494, 1875.

[2] F. Scholz, Electroanalytical Methods: Guide to Experiments and Applications, Springer, 2010.

[3] B. Berge, "Electrocapillarite et mouillage de films isolants par l'eau," *C. R. Acad. Sci. II,* vol. 317, p. 157, 1993.

[4] B. Berge and J. Peseux, "Variable focal lens controlled by an external voltage: An application of electrowetting," *Eur. Phys. J.,* vol. 3, pp. 159-163, 2000.

[5] Y.-J. Chang, K. Mohseni and V. M. Bright, "Fabrication of tapered SU-8 structure and effect of sidewall angle for a variable focus microlens using EWOD," *Sensors and Actuators A,* vol. 136, pp. 546-553, 2007.

[6] J. Cheng and C.-L. Chen, "Adaptive beam tracking and steering via electrowetting-controlled liquid prism," *Applied Physics Letters,* vol. 99, p. 191108, 2011.

[7] J. T. Gopinath, V. M. Bright, C. C. Cogswell, R. D. Niederriter, A. Watson, R. Zahreddine and R. H. Cormack, "Simulation of electrowetting lens and prism

arrays for wavefront compensation," *Appl. Opt.,* vol. 51, p. 6618, 2012.

[8] W. Han, J. W. Haus, P. McManamon, J. Heikenfeld, N. Smith and J. Yang, "Transmissive beam steering through electrowetting microprism arrays," *Optics Communications,* vol. 283, pp. 1174-1181, 2010.

[9] Y. Hongbin, Z. Guangya, C. F. Siong and L. Feiwen, "Optofluidic Variable Aperture," *Optics Letters,* vol. 33, p. 548, 2008.

[10] L. Hou, J. Zhang, N. Smith, J. Yang and J. Heikenfeld, "A full description of a scalable microfabrication process for arrayed electrowetting microprisms," *Journal of Micromechanics and Microengineering,* vol. 20, p. 12, 2010.

[11] L. Hou, N. R. Smith and J. Heikenfeld, "Electrowetting Micro-prisms and Micro-mirrors," in *LEOS 2007 - IEEE Lasers and Electro-Optics Society Annual Meeting Conference Proceedings*, 2007.

[12] X. Hu, S. Zhang, C. Qu, Q. Zhang, L. Lu, X. Ma, X. Zhang and Y. Deng, "Ionic liquid based variable focus lenses," *Soft Matter,* vol. 7, pp. 5941-5943, 2011.

[13] F. Krogmann, W. Moench and H. Zappe, "A MEMS-Based Variable Micro-Lens System," *Journal of Optics A: Pure and Applied Optics,* vol. 8, p. 330, 2006.

[14] F. Krogmann, W. Mönch and H. Zappe, "Electrowetting for Tunable Microoptics," *J. of Microelectromech. Syst.,* vol. 17, p. 1501, 2008.

[15] S. Kuiper and B. H. Hendriks, "Variable-Focus Liquid Lens For Miniature Cameras," *Applied Physics Letters,* vol. 85, pp. 1128-1130, 2004.

[16] S. Kuiper, "Electrowetting-based liquid lenses for endoscopy," *Proc. of SPIE,*

vol. 7930, pp. 793008-1, 2011.

[17] Y. Kwon, Y. Choi, K. Choi, Y. Kim, S. Choi, J. Lee and J. Bae, "Development of Micro Variable Optics Array," in *IEEE MEMS*, San Francisco, 2014.

[18] S.-L. Lee and C.-F. Yang, "Numerical simulation for meniscus shape and optical performance of a MEMS-based liquid micro-lens," *Opt. Express,* vol. 16, p. 19995, 2008.

[19] C. U. Murade, D. van den Ende and F. Mugele, "High Speed Adaptive Microlens Array," *Optics Express,* vol. 20, pp. 1128-1130, 2011.

[20] C. Murade, J. Oh, D. van den Ende and F. Mugele, "Electrowetting driven optical switch and tunable aperture," *Optics Express,* vol. 19, no. 16, pp. 15525-15531, 2011.

[21] R. D. Niederriter, A. M. Watson, R. N. Zahreddine, C. J. Cogswell, R. H. Cormack, M. V. Bright and J. T. Gopinath, "Electrowetting Lenses For Compensating Phase And Curvature Distortion In Arrayed Laser Systems," *Applied Optics,* vol. 52, p. 3172, 2013.

[22] B. Ozbay, J. Losacco, R. Cormack, R. Weir, V. Bright, J. Gopinath, D. Restrepo and E. Gibson, "Miniaturized fiber-coupled confocal fluorescence microscope with an electrowetting variable focus lens using no moving parts," *Optics Letters,* vol. 40, no. 11, pp. 2553-2556, 2015.

[23] N. R. Smith, L. Zhou, J. Zhang and J. Heikenfeld, "Fabrication And Demonstration Of Electrowetting Liquid Lens Arrays," *Journal of Display Technology,* vol. 5, p. 411, 2009.

[24] N. R. Smith, "Investigation of the Performance Potential for Arrayed Electrowetting Microprisms," University of Cincinnati, Cincinnati, 2009.

[25] N. R. Smith, D. C. Abeysinghe, J. W. Haus and J. Heikenfeld, "Agile wide-angle beam steering with electrowetting microprisms," *Optics Express,* vol. 14, p. 6557, 2006.

[26] S. Terrab, A. Watson, K. Dease, J. Gopinath and V. Bright, "Electrowetting-Based Variable Tuning Prism," in *OSA*, Proceedings of IEEE Conference on Lasers and Electro-optics, 2015.

[27] A. M. Watson, K. Dease, S. Terrab, C. Roath, J. T. Gopinath and V. M. and Bright, "Focus tunable low power electrowetting lens on thin parylene films," 2015.

[28] K. Zhou, J. Heikenfeld, K. Dean, E. Howard and M. Johnson, "A full description of a simple and scalable fabrication process for electrowetting displays," *Journal of Micromechanics and Microengineering,* vol. 19, 2009.

[29] J. Jackel, S. Hackwood, J. Veselka and G. Beni, "Electrowetting switch for multimode optical fibers," *Applied Optics,* vol. 11, p. 1765, 1983.

[30] C. Liu and L. W. Q.-H. Li, "Bidirectional optical switch based on electrowetting," *Journal of Applied Physics,* vol. 113, p. 193106, 2013.

[31] R. Fair, "Digital Microfluidics: is a true lab-on-a-chip possible?," *Microfluid Nanofluid,* vol. 3, pp. 245-281, 2007.

[32] S. K. Cho, H. Moon, and C.-J. Kim., "Creating, Transporting, Cutting, and

Merging Liquid Droplets by Electrowetting-Based Actuation for Digital Microfluidics Circuits," *J. MEMS,* vol. 12, 2003.

[33] M. Pollack, A. Shenderov and R. Fair, "Electrowetting-based actuation of droplets for integrated microfluidics," *Lab Chip,* vol. 2, pp. 96-101, 2002.

[34] A. R. Wheeler, "Putting Electrowetting to Work," *Chemistry Perspectives,* 23 October 2008.

[35] L. Malic, T. Veres and M. Tabrizian, "Biochip functionalization using electrowetting-on-dielectric digital microfluidics for surface plasmon resonance imaging detection of DNA hybridization," *Biosensors and Bioelectronics,* vol. 24, no. 7, pp. 2218-2224, 2009.

[36] M. Pollack, R. Fair and A. Shenderov, "Electrowetting-based actuation of liquid droplets for microfluidic applications," *Applied Physics Letters,* vol. 77, 2000.

[37] V. Srinivasan, V. Pamula and R. Fair, "An integrated digital microfluidic lab-on-a-chip for clinical diagnostics on human physiological fluids," *Lab Chip,* vol. 4, pp. 310-315, 2004.

[38] Y.-H. Chang, G.-B. Lee, F.-C. Huang, Y.-Y. Chen and J.-L. Lin, "Integrated polymerase chain reaction chips utilizing digital microfluidics," *Biomed Microdevices,* vol. 8, pp. 215-225, 2006.

[39] L. Luan, M. Royal, R. Evans, R. Fair and N. Jokerst, "Chip Scale Optical Microresonator Sensors Integrated With Embedded Thin Film Photodetectors on Electrowetting Digital Microfluidics Platforms," *Sensors Journal, IEEE,* vol. 12, no. 6.

[40] M. Pollack, V. Pamula, V. Srinivasan and A. Eckhardt, "Applications of electrowetting-based digital microfluidics in clinical diagnostics," *Expert Review of Molecular diagnostics,* vol. 11, 2011.

[41] R. Fair, A. Khlystov, T. Tailor, V. Ivanov, R. Evans, P. Griffin, V. Srinivasan, V. Pamula, M. Pollack and J. Zhou, "Chemical and Biological Applicatios of Digital-Microfluidic Devices," *Design & Test of Computers, I,* vol. 24, no. 1, 2007.

[42] J. Gong and C. Kim, "All-electronic droplet generation on-chip with real-time feedback control fro EWOD digital microfluidics," *Lab Chip,* vol. 8, pp. 898-906, 2008.

[43] K. Choi, A. H. Ng, R. Fobel and A. Wheeler, "Digital microfluidics," *Analytical Chemisty,* vol. 5, pp. 413-440, 2012.

[44] M. Abdelgawad and A. Wheeler, "Low-cost, rapid-prototyping of digital microfluidic devices," *Microfluid Nanofluid,* vol. 4, pp. 349-355, 2008.

[45] I. Barbulovic-Nad, H. Yang, P. Park and A. Wheeler, "Digital microfluidics for cell-based assays," *Lab Chip,* vol. 8, pp. 519-526, 2008.

[46] D. Witters, N. Vergauwe, S. Vermeir, F. Ceyssens, S. Liekens, R. Puers and J. Lammertyn, "Biofunctionalization of electrowetting-on-dielectric digital microfluidic chips for miniaturized cell-based applications," *Lab Chip,* vol. 11, pp. 279-2794, 2011.

[47] R. A. Hayes and B. J. Feenstra, "Video-speed electronic paper based on electrowetting," *Nature,* vol. 425, pp. 383-385, 2003.

[48] J. Heikenfeld, K. Zhou, E. Kreit, B. Raj, S. Yang, B. Sun, A. Milarcik, L. Clapp and R. Schwartz, "Electrofluidic displays using Young-Laplace transposition of brilliant pigment dispersion," *Nature Photonics,* vol. 3, pp. 292-296, 2009.

[49] B. Sun and J. Heikenfeld, "Observation an doptical implications of oil dewetting patterns in electrowetting displays," *Journal of Micromechanics and Microengineering,* vol. 18, no. 2, 2008.

[50] R. Hayes and B. Feenstra, "Video-speed electronic paper based on electrowetting," *Nature,* vol. 425, pp. 383-385, 2003.

[51] J. Heikenfeld, N. Smith, M. Dhindsa, K. Zhou, M. Kilaru, L. Hou, J. Zhang, E. Kreit and B. Raj, "Recent Progress in Arrayed Electrowetting Optics," *OPN,* vol. 20, pp. 20-26, 2009.

[52] K. Blankenbach, A. Schmoll, A. Bitman, F. Bartels and D. Jerosch, "Novel highly reflective and bistable electrowetting displays," *Journal of the Society for Information Display,* vol. 16, no. 2, pp. 237-244, 2008.

[53] A. Schultz, J. Heikenfeld, H. Kang and W. Cheng, "1000:1 Contrast Ration Transmissive Electrowetting Displays," *Journal of Display Technology,* vol. 7, no. 11, 2011.

[54] Y. Lao, K. Zhou and J. Heikenfeld, "Ultra-High Transmission Electrowetting Displays Enabled by Integrated Reflectors," *Journal of Display Technology,* vol. 4, no. 2, pp. 120-122, 2008.

[55] B. Feenstra, R. Hayes, R. van Dijk, R. Boom, M. Wagemans, I. G. Camps, A. Giraldo and B. Heijden, "Electrowetting-Based Displays: Bringing Microfluidics

Alive On-Screen," in *19th IEEE International Conference on MEMS*, Istanbul, 2006.

[56] R. van Dijk, B. Feenstra, R. Hayes, G. Camps, R. Boom, M. Wafemans, A. Giraldo, B. Heijden, R. Los and H. Feil, "68.3: Gray Scales for Video Applications on Electrowetting Displays," *Society for Information Display Symposium Digest of Technical Papers,* vol. 37, no. 1, pp. 1926-1929, 2006.

[57] P. Sureshkumar, M. Kim, E. Song, Y. Lim and S. Lee, "Effect of surface roughness on the fabrication of electrowetting display cells and its electro-optic switching behavior," *Surface Review and Letters,* vol. 16, 2009.

[58] S. Berry, J. Kedzierski and B. Abedian, "Low Voltage Electrowetting Usign Thin Fluoropolymer Films," *Journal of Colloidal and Interface Science,* p. 517, 2006.

[59] A. A. Kornyzheve, A. R. Kucernak, M. Marinescu, C. W. Monroe and M. Urbakh, "Ultra-Low-Voltage Electrowetting," *Journal of Physical Chemistry,* vol. 114, p. 14885, 2010.

[60] N. R. Smith, L. Hou, J. Zhang and J. Heikenfeld, "Experimental Validation Of >1 Khz Electrowetting Modulation," *University/Government/Industry Micro/Nano Symposium,* vol. 17, pp. 11-14, 2008.

[61] J. Y. Chen, A. Kutana, C. P. Collier and K. P. Giapis, "Electrowetting In Carbon Nanotubes," *Science,* vol. 310, pp. 1128-1130, 2005.

[62] G. D. Love, "Wave-Front Correction And Production Of Zernike Modes With A Liquid-Crystal Spatial Light Modulator," *Applied Optics,* vol. 36, p. 1517, 1997.

[63] C. Warde, A. D. Fisher, D. M. Cocco and M. Y. Burmawi, "Microchannel Spatial Light Modulator," *Optics Letters,* vol. 196, 1978.

[64] T. Weyrauch, M. A. Vorontsov, T. G. Bifano, A. Tuantranont, V. M. Bright, J. Karpinksy and J. Hammer, "Performance Evaluation Of Micromachined Mirror Arrays For Adaptive Optics," *SPIE,* p. 4124, 2000.

[65] L. Schatzberg, T. Bifano, S. Cornelissen, J. Stewart and Z. BLeier, "Secure Optical Communication Using Deformable MEMS Mirrors," *SPIE,* vol. 7209, p. 72090C1, 2009.

[66] M. C. Roggemann, V. M. Bright, B. M. Welsh, D. Cowan and M. Lett, "Micro-Electromechanical Deformable Mirrors For Aberration Control In Optical Systems," *Optics and Quantum Electronics,* vol. 31, p. 451, 1999.

[67] W. D. Cowan, M. K. Lee, B. M. Welsh, V. M. Bright and M. C. Roggemann, "Surface Micromachined Segmented Mirrors For Adaptive Optics," *IEEE Journal of Selected Topics in Quantum Electronics,* vol. 5, p. 90, 1999.

[68] H. Ren, D. Fox, P. A. Anderson, B. Wu and S. Wu, "Tunable-Focus Liquid Lens Controlled Using A Servo Motor," *Optics Express,* vol. 14, p. 8031, 2006.

[69] D. Zhang, N. Justis, V. Lien, Y. Berdichevsky and Y. Lo, "High-Performance Fluidic Adaptive Lenses," *Applied Optics,* vol. 43, p. 783, 2004.

[70] F. Mugele and J.-C. Baret, "Electrowetting: from basics to applications," *J. Phys.: Condens. Matter,* vol. 17, pp. R705-R774, 2005.

[71] J. Berthier, Microdrops and Digital Microfluidics, Norwich, NY: William

Andrew, 2008.

[72] T. B. Jones, "More about the electromechanics of electrowetting," *Mechanics Research Communications,* vol. 36, pp. 2-9, 2009.

[73] J. R. M. H. H. Woodson, "Part 1," in *Electromechanical Dynamics*, New York, Wiley, 1968, p. Chapter 3.

[74] S. Seely, An Introduction to Engineering Systems: Pergamon Unified Engineering Series, Elsevier Technology & Engineerin, 2013.

[75] C. A. S. Panel, Interviewee, *9th International Meeting on Electrowetting and Related Micro/Electrofluidic Science and Technology*. [Interview]. 23-25 June 2014.

[76] S. Chevalliot, S. Kuiper and J. Heikenfeld, "Experimental Validation of the Invariance of Electrowetting Contact Angle Saturation," *Journal of Adhesion Science and Technology,* vol. 26, pp. 1909-1930, 2012.

[77] A. Drygiannakis, A. Papathanasiou and A. Boudouvis, "On the Connection between Dielectric Breakdown Strength, Trapping of Charge, and Contact Angle Saturation in Electrowetting," *Langmuir,* vol. 25, p. 1470152, 2009.

[78] S. Agarwal, A. Agarwal, L. Buratto, D. Apple and J. Ali, Testbook of Ophthalmology, Jaypee, 2002.

[79] P. Nussbaum, R. Völkel, H. P. Herzig, M. Eisner and S. Haselbeck, "Design, fabrication and testing of microlens arrays for sensors and microsystems," *Pure Appl. Opt.,* vol. 6, p. 617, 1999.

[80] A. V. Jelalian, Laser Radar Systems, Boston-London: Artech House, 1992.

[81] J. L. Gibson, B. D. Duncan, E. A. Watson and J. S. Loomis, "Wide-angle decentered lens beam steering for infrared countermeasures applications," *Opt. Eng.,* vol. 43, pp. 2312-2321, 2004.

[82] P. F. McManamon, T. A. Dorschner, D. L. Corkum, L. J. Friedman, D. S. Hobbs, M. Holz, S. Liberman, H. Q. Nguyen, D. P. Resler, R. C. Sharp and E. A. Watson, "Optical Phased Array Technology," *Proc. IEEE,* vol. 84, pp. 268-298, 1996.

[83] B. Sun, K. Zhou, Y. Lao, J. Heikenfeld and W. Cheng, "Scalable fabrication of electrowetting displays with self-assembled oil dosing," *Appl. Phys. Lett.,* vol. 91, pp. 011106-1--011106-3, 2007.

[84] B. Berge, J. B. H. Gaton, G. Malet, E. Simon and F. Thieblemont, "Liquid lens based on Electrowetting: actual developments on larger aperture and multiple electrodes design for image stabilization or beam steering," in *MOEMS and Miniaturized Systems XII*, 2013.

[85] I. Guha, J. Kedzierski and B. Abedian, "Low-voltage electrowetting on a lipid bilayer formed on hafnium oxide," *Applied Physics Letters,* vol. 99, p. 024105, 2011.

[86] E. Gates, Introduction to Electronics, Cengage Learning, 2001.

[87] M. Dhindsa, S. Kuiper and J. Heikenfeld, "Reliable and low-voltage electrowetting on thin parylene films," *Thin Solid Films,* vol. 519, pp. 3346-3351, 2011.

[88] C. Lee and C. Kim, "Maximizing the Giant Liquid Slip on Superhydrophobic Microstructures by Nanostructuring Their Sidewalls," *Langmuir,* vol. 25, no. 21, pp. 12812-12818, 2009.

[89] M. Maillard, J. Legrand and B. Berge, "Two Liquids Wetting and Low Hysteresis Electrowetting on Dielectric Applications," *Langmuir,* vol. 25, no. 11, pp. 6162-6167, 2009.

[90] S. Chevalliot, J. Heikenfeld, L. Clapp, A. Milarcik and S. Vilner, "Analysis of Nonaqueous Electrowetting Fluids for Displays," *Journal of Display Technology,* vol. 7, no. 12, pp. 649-656, 2011.

[91] Handbook of Organic Solvents, Boca Raton, FL: CRC, 1995.

[92] B. Raj, M. Dhindsa, N. R. Smith, R. Laughlin and J. Heikenfeld, "Ion and Liquid Dependent Dielectric Failure in Electrowetting Systems," *Langmuir,* vol. 25, pp. 12387-92, 2009.

[93] N. Subrahmanyam, B. Lal and M. Avadhanulu, A Text Book of Optics, S. Chand, 2004.

[94] F. Miller, A. Vandome and J. McBrewster, Beer-Lambert Law, VDM Publishing, 2009.

[95] E. Wilson, J. Decius and P. Cross, Molecular Vibrations: The Theory of Infrared and Raman Vibrational Spectra, Courier Corporation, 2011.

[96] J. Wang, Z. Yuan, L. Kang, K. Yang, Y. Zhang and X. Liu, "Study of the mechanism of ‘smile’ in high power diode laser arrays and strategies in

improving near-field linearity," in *Proceedings of IEEE Electronic Components and Technology Conference*, 2009.

[97] H. Seidel, L. Csepregi, A. Heuberger and H. Baumgartel, "Anisotropic Etching of Crystalline Silicon in Alkaline Solutions," *J. Electrochem. Soc.,* vol. 137, p. 3612, 1990.

[98] A. J. Niskanen, T. Ylinen-Hinkka, S. Kulmala and S. Franssila, "Ultrathin tunnel insulator films on silicon for electrochemiluminescene studies," *Thin Solid Films,* vol. 517, p. 5779, 2009.

[99] M. J. Madou, Fundamentals of Microfabrication, CRC Press, 2002.

[100] A. V. Ermushev, B. V. Mchedlishvili, V. A. Oleĭnikov and A. V. Petukhov, "Surface enhancement of local optical fields and the lightning-rod effect," *Quantum Electronics,* vol. 23, p. 435, 1993.

[101] R. Miller, Y. Lau and J. Booske, "Electric field distribution on knife-edge field emitters," *Applied Physics Letters,* vol. 91, 2007.

[102] C. E. Hamilton, S. C. Tidwell, D. Meekhof, J. Seamans, N. Gitkind and D. D. Lowenthal, "High-power laser source with spectrally beam-combined diode laser bars," *Proc. SPIE,* vol. 5336, pp. 1-10, 2004.

[103] J. F. Monjardin, K. M. Nowak, H. J. Baker and D. R. Hall, "Correction of beam errors in high power laser diode bars and stacks," *Optics Express,* vol. 14, pp. 8178-8183, 2006.

[104] V. Mahajan, "Zernike Circle Polynomials and Optical Aberrations of Systems

with Circular Pupils," *Engineering Laboratory Notes,* vol. 17, pp. 8121-8124, 1994.

[105] H. Verheijen and M. Prins, "Reversible Electrowetting and Trapping of Charge: Model and Experiments," *Langmuir,* vol. 15, pp. 6616-6620, 1999.

[106] Specialty Coating Systems, "SCS Parylene Properties," http://scscoatings.com/what_is_parylene/parylene_properties.aspx.

[107] W. Dolbier Jr. and W. Beach, "Parylene-AF4: a polymer with exceptional dielctric and thermal properties," *Journal of Fluorine Chemisty,* vol. 41, pp. 97-104, 2003.

[108] S. Himmelein, N. Sporenberg, M. Schonhoff and B. Ravoo, "Size-selective permeation of water-soluable polymers through the bilayer membrane of cyclodextrin vesicles investigated by PFG-NMR," *Langmuir,* vol. 14, pp. 3988-3995, 2014.

[109] Wikipedia, "Sodium dodecyl sulfate," Wikipedia, 27 November 2014. [Online]. Available: http://en.wikipedia.org/wiki/Sodium_dodecyl_sulfate. [Accessed 1 December 2014].

[110] G. Duplatre, M. F. F. Marques and M. d. G. Miguel, "Size of Sodium Dodecyl Sulfate Micelles in Aqueous Solutions as Studied by Positron Annihilation Lifetime Spectroscopy," *Journal of Physical Chemistry,* vol. 100, no. 41, pp. 16608-16612, 1996.

[111] W. Gorham, "A New, General Synthetic Method for the Preparation of Linear Poly-p-xylxylenes," *Journal of Polymer Science Part A-1,* vol. 4, pp. 3027-3039,

1966.

[112] Sigma-Aldrich, "Product Specification," [Online]. Available: http://www.sigmaaldrich.com/united-states.html. [Accessed 1 Dec. 2014].

[113] J. E. Greivenkamp, Field Guide to Geometrical Optics, SPIE, 2004.

[114] S. Diaham, M. Bechara and M.-L. Locatelli, "Dielectric strength of Parylene HT," *Journal of Applied Physics,* vol. 115, p. 054102, 2014.

[115] P. Liebetraut, S. Petsch, J. Liebeskind and H. Zappe, "Elastomeric lenses with tunable astigmatism," *Light: Science & Applications,* vol. 2, 2013.

[116] S. F. Treynelis and R. Dingledine, "Potassium-induced spontaneous electrographic seizures in the rat hippocampal slice," *J. Neurophysiol,* vol. 59, pp. 259-76, 1988.

[117] D. Dombeck, C. Harvey, L. Tian, L. Looger and D. Tank, "Functional imaging of hippocampal place cells at cellular resolution during virtual navigation," *Nature Neuroscience,* vol. 13, pp. 1433-40, 2010.

[118] K. Deisseroth, "Optogenetics," *Nature Methods,* vol. 8, pp. 26-29, 2010.

[119] L. Tian, S. hires, T. Mao, D. Huber, M. Chiappe and e. al., "Imaging neural activity in works flies and mice with improved GCaMP calcium indicators," *Nature Methods,* vol. 6, pp. 875-881, 2009.

[120] Y. Ziv, L. D. Burns, E. D. Cocker, E. O. Hame, K. K. Ghosh, L. J. Kitch, A. E. Gamal and M. J. Schnitzer, "Long-term dynamics of CA1 hippocampal place

codes," *Nature Neuroscience,* vol. 16, pp. 264-266, 2013.

[121] G. Deuschl, C. Schade-Bittinger, P. Krack and ..., "A randomized trial of deep-brain stimulation for Parkinson's disease," *The New England Journal of Medicine,* vol. 355, pp. 896-908, 2006.

[122] H. Mayberg, A. Lozano, V. Voon, H. McNeely, D. Seminowicz, C. Hamani, J. Schwalb and S. Kennedy, "Deep Brain Stimulation for Treatment-Resistant Depression," *Neuron,* vol. 45, no. 5, pp. 651-660, 2005.

[123] T. Loddenkemper, A. Pan, S. Neme, K. Baker, A. Rezai, D. Dinner, E. Montgomery Jr. and H. Luders, "Deep Brain Stimulation in Epilepsy," *Journal of Clinical Neurophysiology,* vol. 18, no. 6, pp. 514-532, 2001.

[124] R. Driggers, "What's new in infrared systems," *SPIE Professional,* p. http://spie.org/x106781, April 2014.

[125] D. Reago, "Current Directions in Sensor Technologies at NVESD," Keynote Presentation:SPIE DSS IR Technology & Applications XLI Conference, 2015.

[126] Raytheon, "Next Generation EO/IR Detectors," *Raytheon Technology Today,* p. http://www.raytheon.com/news/technology_today/2014_i1/nextgen.html, 2014.

[127] K. Judd, C. Colbert, R. Smith, K. Vilardebo, J. Waterman, G. Petty and J. Kilzer, "A compact deployable mid-wave infrared imaging system for wide-area persistence surveillance in maritime environments," *Proc. SPIE,* vol. 8353, p. 83530O, 2012.

[128] J. Nichols, J. Waterman, R. Menon and J. Devitt, "Performance characteristics

of a submarine panoramic infrared imaging sensor," *Proc. SPIE,* vol. 7660, p. 766005, 2010.

[129] C.-I. Chang, Hyperspectral Imaging: Techniques for Spectral Detection and Classification, Springer Science and Business Media, 2003.

[130] F. Peng, D. Xu, H. Chen and S.-T. Wu, "Low voltage polymer network liquid crystal for infrared spatial light modulators," *Optics Express,* vol. 23, no. 3, p. 2361, 2015.

[131] J. Pugh, J. Stokes, M. Lopez-Garcia, C.-H. Gan, G. Nash, J. Rarity and M. Cryan, "Tunable Flat Lenses in the Infrared," in *Proceedings of IEEE Conference on Transparent Optical Networks*, 2014.

[132] T. Welton, "Room-Temperature Ionic Liquids. Solvents for Synthesis and Catalysis," *Chem. Rev.,* vol. 99, pp. 2071-2083, 1999.

[133] R. Rogers and K. Seddon, "Ionic Liquids -- Solvents of the Future?," *Science,* vol. 302, pp. 792-793, 2003.

[134] H. Ricks-Laskoski and A. Snow, "Synthesis and Electrical Field Actuation of an Ionic Liquid Polymer," *Journal of American Chemical Society,* vol. 128, pp. 12402-12403, 2006.

[135] Pike Technologies, "ATR - Theory and Applications," PIKE Technologies, Madison, WI, 2011.

[136] Solvionic, "IR Spectre: N-Propyl-N-methylpyrrolidinium bis(fluorosulfonyl)imide 99.9%," http://en.solvionic.com/

[137] V. Srinivasan, V. Pamula and R. Fair, "Droplet-based microfluidic lab-on-a-chip for glucose detection," *Anal. Chim. Acta,* vol. 291, 2004.

[138] M. Prins, W. Welters and J. Weekamp, "Fluid control in multichannel structures by electrocapillary pressure," *Science,* vol. 291, 2001.

[139] Wavefront Sciences, "Complete Light Analysis System User's Manual," Software v. 1.75, 2004.

[140] J. Goodman, "Introduction to Fourier Optics," New York, McGraw-Hill Companies, Inc., 1996, p. 146.

[141] J. Yota, H. Shen, R. Ramanathan, "Characterization of atomic layer deposition HfO_2, Al_2O_3, and plasma-enhanced chemical vapor deposition Si_3N_4 as metal-insulator-metal capacitor dielectric for GaAs HBT technology," *Journal of Vacuum Science Technology A*, vol. 31, 2013.

[142] L. Han and Z. Chen, "High-Quality Thin SiO_2 Films Grown by Atomic Layer Deposition Using Tris(dimethylamino)silane (TDMAS) and Ozone," *Journal of Solid State Science and Technology*, vol. 2, 2013.

[143] DuPont, "DuPont Teflon AF Amorphous Fluoroplastic Resin," http://www2.dupont.com/Teflon_Industrial/en_US/assets/downloads/h44587.pdf

[144] Cytonix, "FluoroPel A and V Polymer Uses and Properties," http://www.cytonix.com/fluorosolpoly.pdf, 2015.

[145] Cytonix, "Cytop, An Amorphous Fluoropolymer, Mechanical Properties," http://www.bellexinternational.com/products/cytop/, 2009.

APPENDIX A – ELECTROWETTING OPTICAL SHUTTER DEVICE

This project was led by Soraya Terrab with help from Kenneth Underwood, Kevin Dease, and Ryan Montoya. I was responsible for the initial design and fabrication process, as well as assisting with the fabrication. The device is a slight change in the glass tube electrowetting lens and prism devices for a new application of optical shuttering. We can utilize the changing surface angle of the liquid interface as a switching mechanism, based on total internal reflection (TIR). By tuning the interface beyond the critical angle for TIR, light entering the device can be switched between transmitted and reflected modes, enabling an optical switch that is tunable with applied voltage.

The optical shutter design is based on the principle of total internal reflection, as illustrated in Figure A-1(a). The device consists of a sealed glass cylinder to house the liquids and a coupling prism to help achieve the correct incident angle. The sidewall in the cylinder has a thin film electrode, dielectric layer and hydrophobic coating, deposited in that order, respectively. This sidewall functionalizing allows for an electrically tunable liquid surface on the interior of the cylinder. The light is incident on the water near the critical angle for total internal reflection. As the surface curvature is changed by voltage tuning, the liquid interface angle where the light strikes switches between total internal reflection and transmission states. Figure A-1(b) illustrates the angle normal to the surface (1.2-mm from the edge of the device) versus voltage for the 12-mm inner diameter devices. The shaded region indicates the region of total internal reflection for an angle of incidence of the

incident beam (relative to the vertical normal) of 48 degrees. The devices tune from a radius of 16 mm at 0 V to flat at 25 V

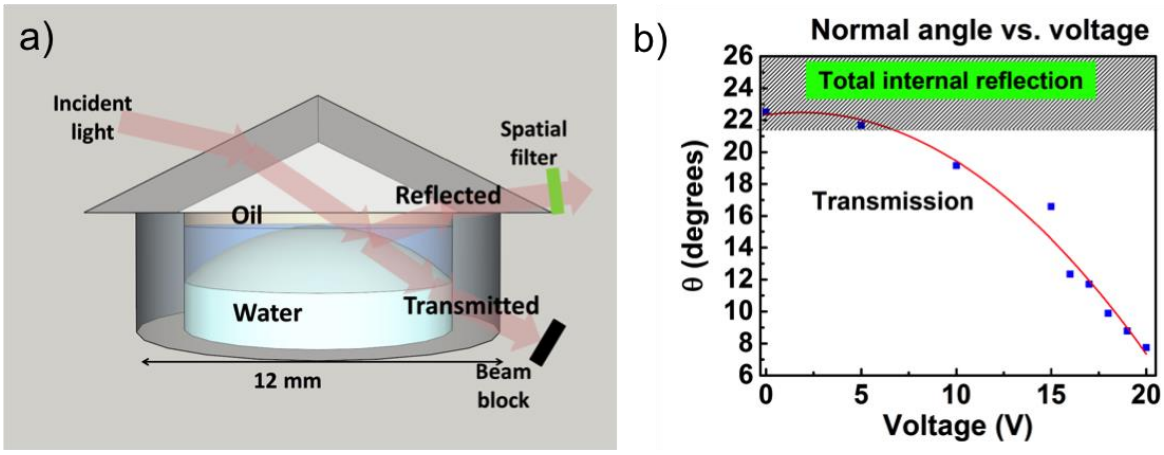

Figure A-7-1 Design for optical shutter. a) Shutter is based on electrowetting lens in glass tube. By changing the applied voltage, we can switch from a curvature of 16 mm to a flat curvature; b) Angle to the normal vs. voltage of curved interface. The shaded area indicates where total internal reflection can be achieved with our setup.

The liquid optical shutter device seen in Figure A-2(a) is formed at the boundary between a polar liquid (water) and non-polar dodecane oil. The liquids are contained within a glass tube, sealed by a glass substrate using glass frit. The sidewall electrode is indium zinc oxide (IZO), an optically transparent conductor. The dielectric layer is made of Parylene C while the hydrophobic coating is thin film Teflon.

The fabrication steps of the liquid shutter device are illustrated in **Error! Reference source not found.** A-3. The liquids are contained within a glass tube of 12 mm inner diameter. Glass frit solution is placed on the rim of the tube and baked at 400 °C (Figure A-3 a). A platinum wire is annealed and shaped in the form of a loop and serves as the base electrode that charges the water. The wire is aligned onto the glass base underneath the glass tube, with glass frit facing down toward the substrate. The tube is clamped down to the substrate and the fixture is cured at 550 °C to allow the frit to bond the glass pieces together, resulting in a hermetic seal between the tube and base (Figure A-3 c-d).

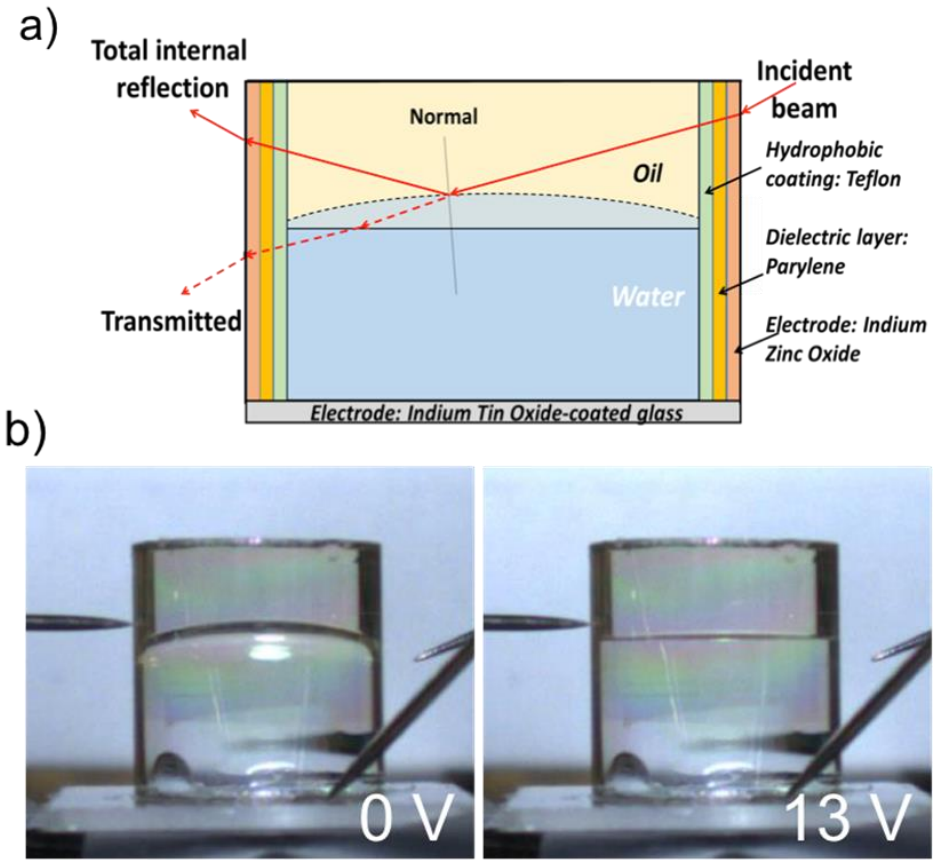

Figure A-2 Optical shutter device. a) ITO glass substrate with tube coated with IZO (300 nm), Parylene C (1um) and Teflon AF 1600 (100nm) dielectric and hydrophobic layers. The glass cavity is bonded to the substrate by glass frit; b) Shutter device at 0 V with an initial curvature of 16mm and at 13 V applied with a flat curvature.

The platinum wire and base of the tube are masked off with Kapton tape before the IZO sidewall electrode is sputter-coated to form a continuous film from the inside to the outside of the tube. IZO is sputtered onto the sample at argon pressure of 5 mTorr and power of 120 W for 15 min to achieve a deposition thickness of 300 nm. The mean free path of the sputtered IZO in the argon at this pressure is an order of magnitude shorter than the distance between target and substrate, enabling diffuse sputtering and a conformal coating from inside to outside of the tube. These process parameters result in an IZO sheet resistance of 23.4 Ω/sq.

Before depositing the thin film dielectrics, the glass tube is cleaned and the exterior masked with Kapton tape to provide electrode contact from outside the tube

after the dielectric deposition. Parylene C is deposited in a vapor-phase, low-vacuum system by VSI Parylene to a thickness of 1 µm. The samples are then dip-coated in a 1:20 solution of Dupont's Teflon AF1600 : Fluorinert FC-40 for the hydrophobic coating. To cure the Teflon above its glass transition temperature of 165°C, the samples are heated in an oven at 120 °C for 10 min and then 170 °C for 20 min. The insets in Figure A-3(e, f) shows the thin film layers on the device.

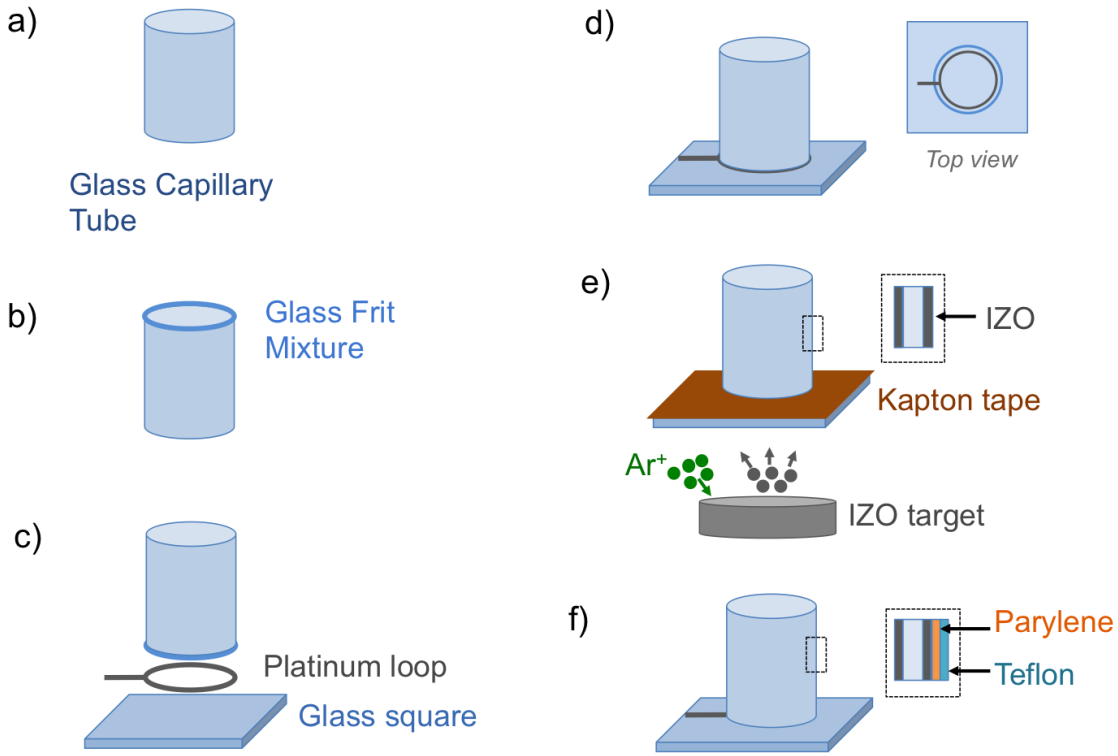

Figure A-3 Fabrication of the optical shutter devices. (a) We start with a glass tube of 12 mm diameter and 10 mm height. (b) We coat the bottom of the glass tube with a glass frit mixture. (c). We align a platinum electrode to address the polar liquid beneath the tube and (d) raise the temperature to 500 C to form the bond. (e) The tube is masked with kapton tape and coated with IZO to form the counter-electrode within cylinder. (f) The device is then coated with Parylene C and Teflon to complete the thin film processing and enable reliable tuning. Figure courtesy of Soraya Terrab.

The devices are filled with a 1% sodium dodecyl sulfate (SDS, Sigma-Aldrich) in DI water solution. In addition to reducing the surface tension between the polar liquid and oil or air, the SDS provides a large, negatively charged dodecyl sulfate

ion, which cannot easily penetrate the Parylene layer when a positive DC voltage is applied to the sidewalls. The dodecane oil is then injected into the device to form the oil/water electrowetting-tunable interface.

The optical shutter device is tested for shutter operation, measuring rejection ratio. Figure A-4 shows a diagram and photo of the experimental set up for rejection testing. The light out of the shutter is collimated with a cylindrical lens and then passed through a telescope in both the reflected and transmitted arms. Silicon detectors with 1 mm-size pinhole are used to detect the light. The output voltage from the detectors is read out with an oscilloscope. The dynamic range of the measurement set up is estimated to be 45 dB.

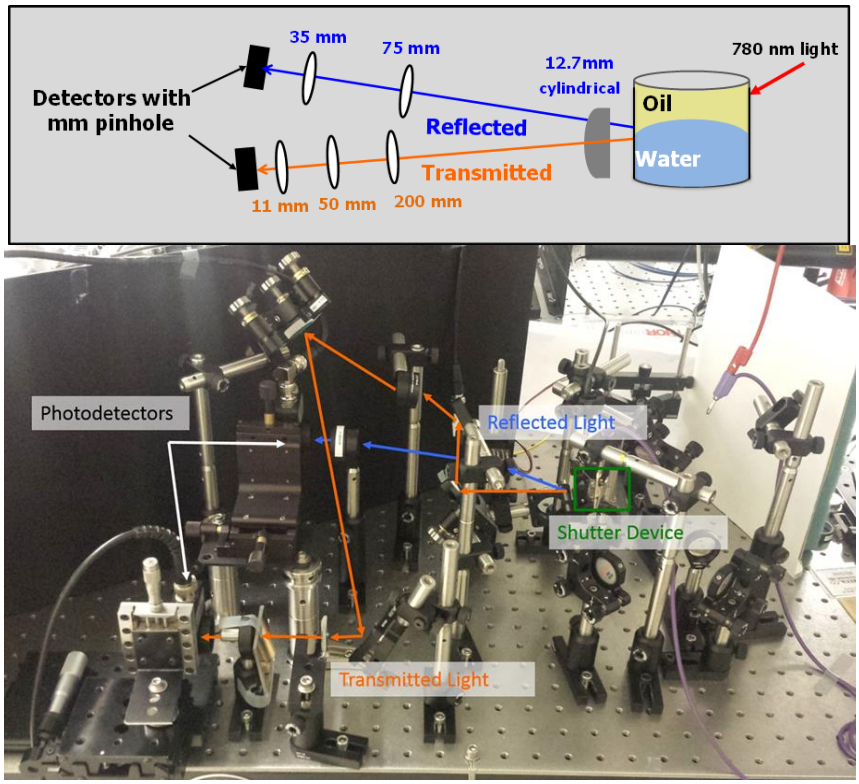

Figure A-4 Experimental setup for optical shutter device. (top) Schematic of optical shutter. Light at 780 nm is incident on the shutter and is either totally internally reflected or transmitted. Both modalities are collimated with a cylindrical lens upon exiting the device. Each arm contains a telescope and silicon detector. (bottom) Photo of experimental set up.

The dynamic range of the shutter was measured to be 30 dB in reflection (reflected power on divided by reflected power off), 22 dB in transmission (transmitted power on vs. transmitted power off), and 42.5 dB for the ratio of reflected power (off) to transmitted power (on). Figure A-5 shows the operation of the shutter versus applied voltage.

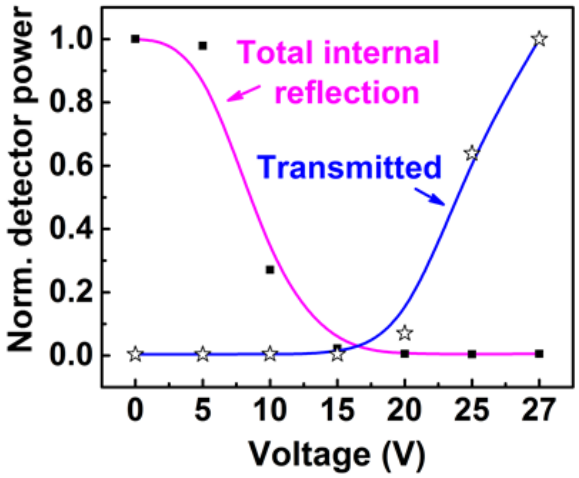

Figure A-5 Shutter rejection measurements showing switching between reflection and transmission as a function of voltage applied to the device.

The measurements fall within the dynamic range of the setup, and are most certainly limited by the following issues (1) scattered light from sidewall coatings (2) lack of spatial filtering to reduce scatter. Additionally, reducing the beam size will enable faster switching with lower voltage. Detector signal-to-noise ratio can be improved dramatically by using a lock-in amplifier and careful placement of attenuators. In summary, the rejection ratio can be improved with a few simple experimental steps including: (a) geometry that does not include sidewall transmission (use a prism on top) (b) add spatial filters to set up (c) consider absorbing layers to reduce scattering further.

APPENDIX B – ABERRATIONS MEASUREMENT

The aberrations of the lenses were measured with a wavefront sensor, and then the output post-processed with custom MATLAB code. This section first describes the operation of the wavefront sensor, and next the fitting routines. These figures and documentation are courtesy of Kevin Dease, who was a major help in driving the aberrations measurements for the lens quality.

B.1 **Shack-Hartmann Wavefront Sensor**

The Shack-Hartmann Wavefront Sensor (WFS) uses a microlens array (50 x 61 lenslets in this case) placed in front of an array of pixels (millions of pixels) to measure an incident wavefront. Each microlenslet has a dedicated array of pixels that act as that lenslet's Area of Interest (AOI). These microlenses focus incident light to somewhere within their AOIs of pixels on the detector array. This focal spot position, as depicted in Figure B-1, is dependent on the slope of the phase incident on each microlenslet, so the phase slope can be back-calculated based on the focal spot position on the detector array. One arbitrary position is set to zero optical path distance (OPD), and the relative OPD for all other positions are calculated from the phase slope. The intensity of the incident wave can also be calculated based on the amount of light in each AOI. See [127] for a more in-depth theory of operation of the Shack-Hartmann and for specific algorithms used.

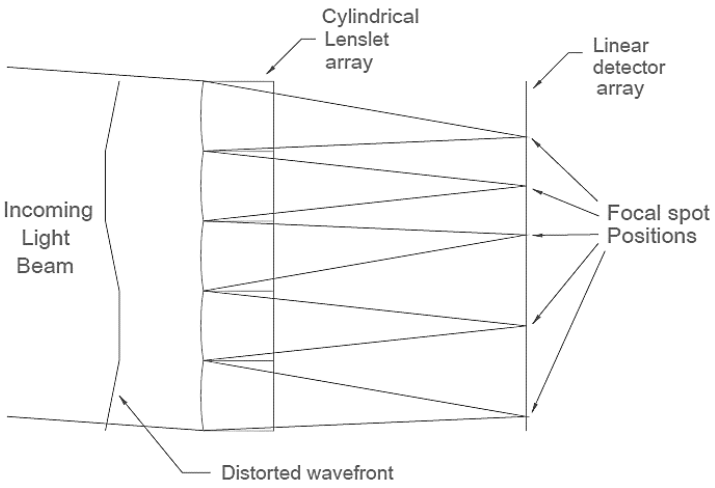

Figure B-1. Shack-Hartmann Wavefront Sensor Visual Depiction of Functionality

The WFS software formats the data into two 50 x 61 arrays of data points. These arrays, representing the AOIs (or data at each microlens), are measures of intensity and phase (or optical path distance). See [127] for more information on this output. When the optical setup is configured correctly, this phase output can be used to help determine the quality of lenses being tested.

A perfect lens creates a perfectly spherical output phase, given a flat input phase. Since real lenses are imperfect, a flat input phase to the lens will result in an output that deviates from the ideal spherical phase. An exaggerated example of this is shown in Figure B-2.

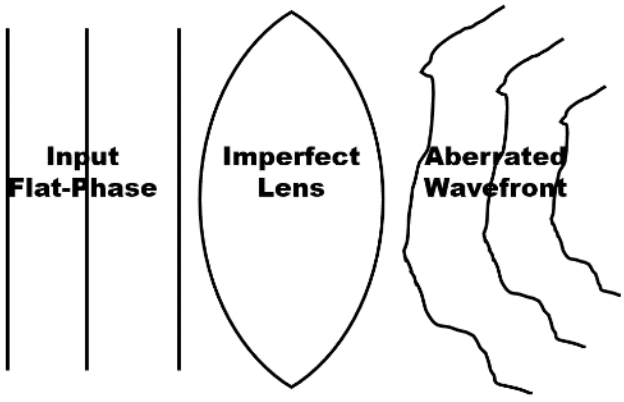

Figure B-2 Exaggerated example of aberrated wavefront generation by real-world lens.

The phase data measured from an electrowetting lens is used to find two different measurements of aberrations: the RMS Deviation from a sphere and the third order spherical aberration Zernike coefficient. Both are described in the RMS Deviation and Zernike Coefficients sections respectively.

B.2 **RMS Deviation**

The code used to determine the RMS deviation from a sphere will now be described. The RMS Deviation from a sphere code calculates the deviation of the aberrated wavefront (like that seen in Figure B-2) from a perfect sphere. This uses the masked phase data (masked to prevent usage of non-real zeros as mentioned in the Shack-Hartmann wavefront sensor section of this report) and a best fit sphere to the masked phase data. The discrete RMS Deviation equation is:

$$RMS\ Deviation = \sqrt{\frac{\sum_{t=1}^{n}(MaskedPhase_t - MaskedBestFitSphere_t)^2}{n}}$$

In the above formula, $MaskedPhase_t$ is the phase value at any point within the mask in the array, $MaskedBestFitSphere_t$ is the corresponding value for the best fit sphere, and n is the total number of data points used in the calculation (number of data points within the mask).

The general procedure is illustrated with the following steps:

1) Mask the phase data
2) Calculate the best fit sphere parameters for the masked phase data (not including the non-real zero data)
3) Generate the best fit sphere and apply the same mask to it as used in step 1

4) Apply the above RMS Deviation calculation on the masked phase and masked best fit sphere data with the total number of points equal to the total number of data points within the mask

The result of this calculation should be a single value, with papers reporting RMS deviations for electrowetting variable lenses in the range of 80 to 211 nm [77]. Again, this value is a direct correlation to the quality of the lens.

B.3 **Zernike Coefficients**

The Zernike Polynomials are an orthonormal basis in cylindrical polar coordinates. Decomposing the wavefront aberrations into the Zernike basis allows simple identification of certain types of common aberrations. The Zernike Coefficients are often used as a measure of aberration that gives more information about the wavefront shape itself than measures such as RMS Deviation from a sphere. Zernike Coefficients are scalars that indicate the weight given to orthogonal polynomials that are used to reconstruct the aberration function, geometrically defined in Figure B-3 as W(x,y) [128].

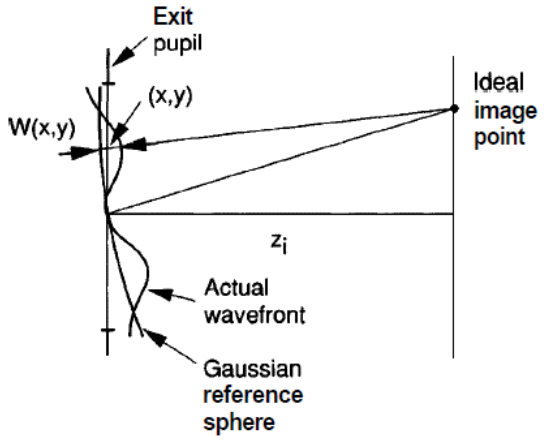

Figure B-3 Geometric definition of Aberration Function, W(x,y). Figure from [128].

The Gaussian reference sphere of Figure B-3, an ideal reference, is calculated from the best fit sphere to the masked data. This best fit sphere is calculated as described in the RMS Deviation section of this report using a mask to exclude non-real data values from the WFS software.

We are concerned with the third order spherical aberration coefficient since it cannot be reduced with alignment, though other coefficients could be relatively easily calculated with a very similar process. The third order spherical aberration in particular is fit to the Zernike polynomial $6\rho^4 - 6\rho^2 + 1$ [103]. In calculating the Zernike coefficient, the data is normalized to the Zernike circle, defined by the edge of the mask described in the RMS Deviation section of this report.

Procedure

1) Mask the phase data
2) Calculate the best fit sphere parameters for the masked phase data (not including the non-real zero data)
3) Generate the best fit sphere and apply the same mask to it as used in step 1
4) Subtract the masked best fit sphere from the masked phase data to get the aberration function (W(x,y) as seen in Figure B-3)
5) Calculate the desired Zernike coefficients using the aberration function with the Matlab code referenced later in this report, ZernikeCalc.m

B.4 **Physical Test Setup**

The physical setup uses a 4F system to image the intensity and phase of a 532 nm laser at the exit pupil of a Device Under Test (DUT) onto the WFS, as shown in Figure B-4. The exit pupil of the DUT is placed at the imaging plane of the 4F

system such that the intensity and phase are imaged onto the WFS. This has the effect of imaging the aberrated wavefront directly after exiting the lens, as depicted in Figure B-2, directly onto the WFS.

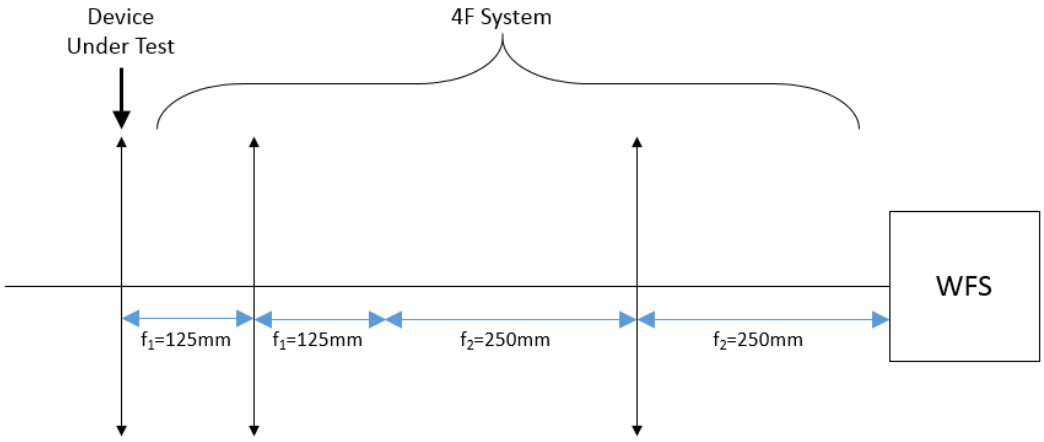

Figure B-4 Physical test setup using 4F system to image wavefront onto wavefront sensor

The telescope creates an imaging system that images the phase at the exit pupil of the lens onto the WFS itself. The $1/e^2$ beam width diameter of the laser without the imaging system was measured using the DataRay camera. The beam width diameter results are tabulated below. The beam had an ellipticity of 0.90. Screenshots of the DataRay software windows can be seen in Figure B-5. Note that there was some jitter in the value, but the data was averaged for 10 to 20 frames.

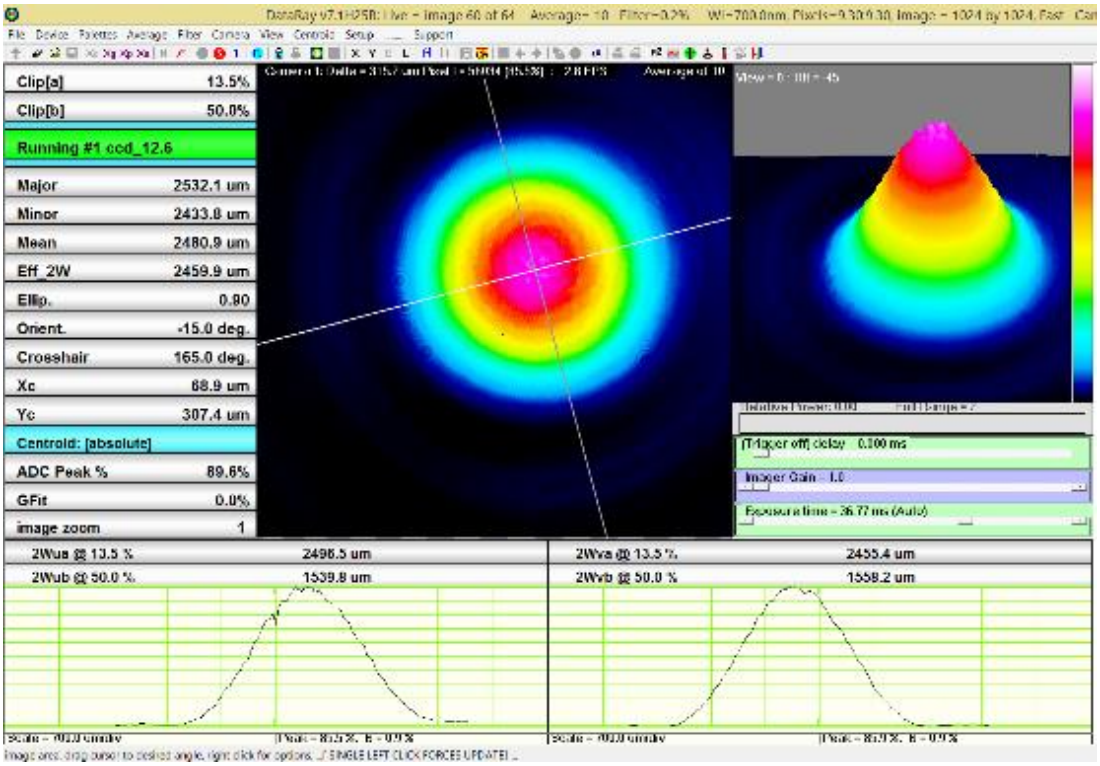

Figure B-5 Screenshot of the DataRay used to capture the beam width for the experiment.

B.5 **Examples of Raw Data Arrays**

Below in Figure B-6 are several example plots of the raw output intensity and phase data arrays (plotted against AOI indices, 61x50).

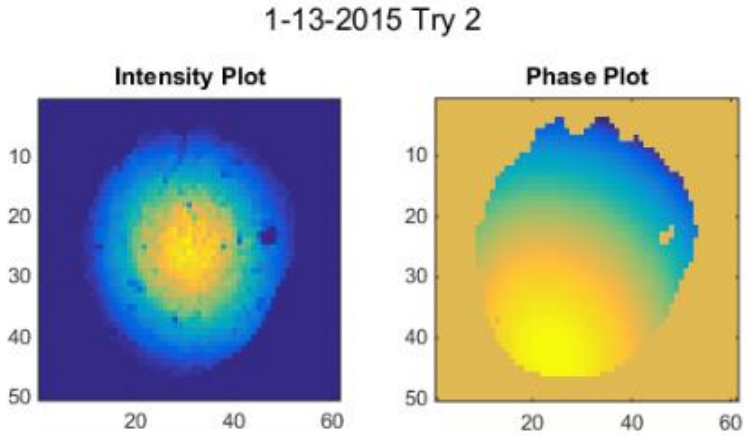

Figure B-6 AOI vs Intensity and Phase from Propylene-Glycol/Dodecane Lens with exit pupil at the imaging plane of the 4F system [77]. 0V Application to lens. Note several non-real "holes" in the data from the WFS software. Data taken from second data collection on January 13, 2015

As can be seen in Figure B-6 there are several “holes” in the phase data where the phase is discontinuous and falls to zero. This is non-real data and can be excluded by setting those points of the mask to zero. The masking process is depicted in Figure B-7.

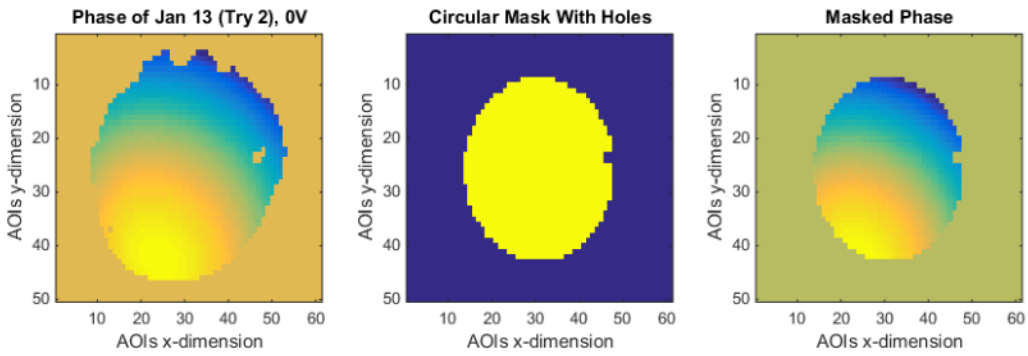

Figure B-7 Phase, mask with holes (calculated using circ_mask_w_holes.m), and combination of the two (masked phase). Only the data points included in the Boolean mask are used

As shown in Figure B-7, only the part of the phase included in the Boolean mask area will be used in the calculation. This excludes the small “hole” of zero values seen in the phase.

B.6 **Zernike Coefficients**

The Zernike coefficients were calculated using the same 2.3 mm diameter mask that excludes holes in the data, as described in the Examples of Raw Data Arrays section of this report. The third order spherical aberration of the electrowetting lens changes with applied voltage. **Error! Reference source not found.**8 shows this relationship. The sign of the data depends on whether the aberration function is calculated by subtracting the phase data from its best fit sphere or vice versa.

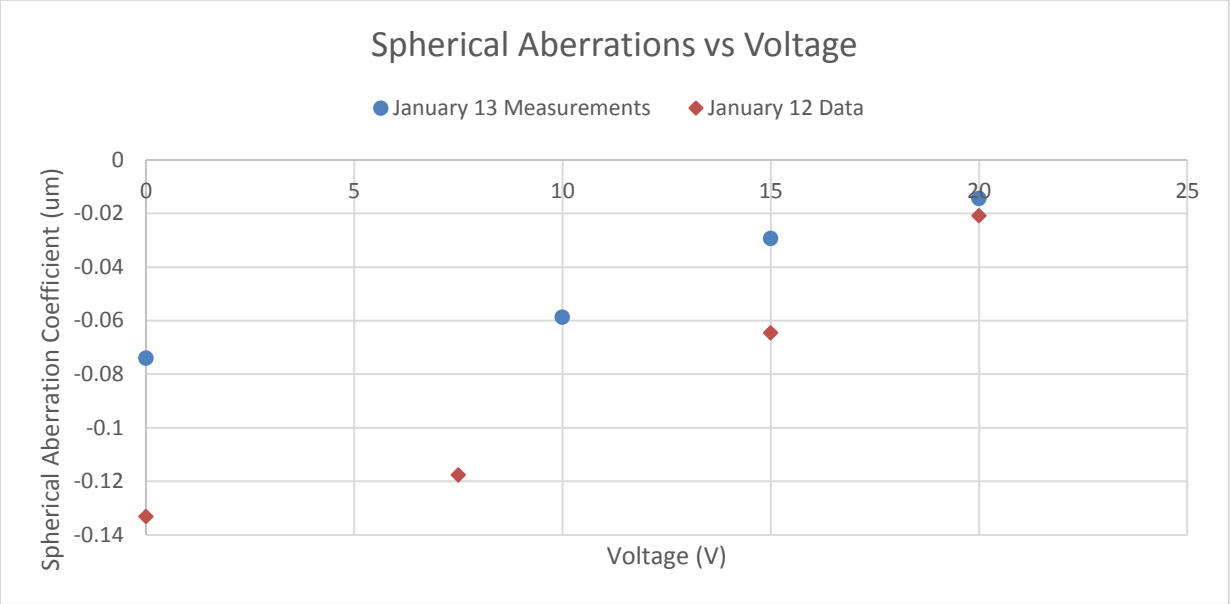

Figure B-8 Voltage vs 3rd Order Spherical Aberration of the two datasets (January 12 and January 13 measurements)

Normalizing each set of data for its 0 V aberration value, we find a similar trend for the data sets as shown in Figure B-9.

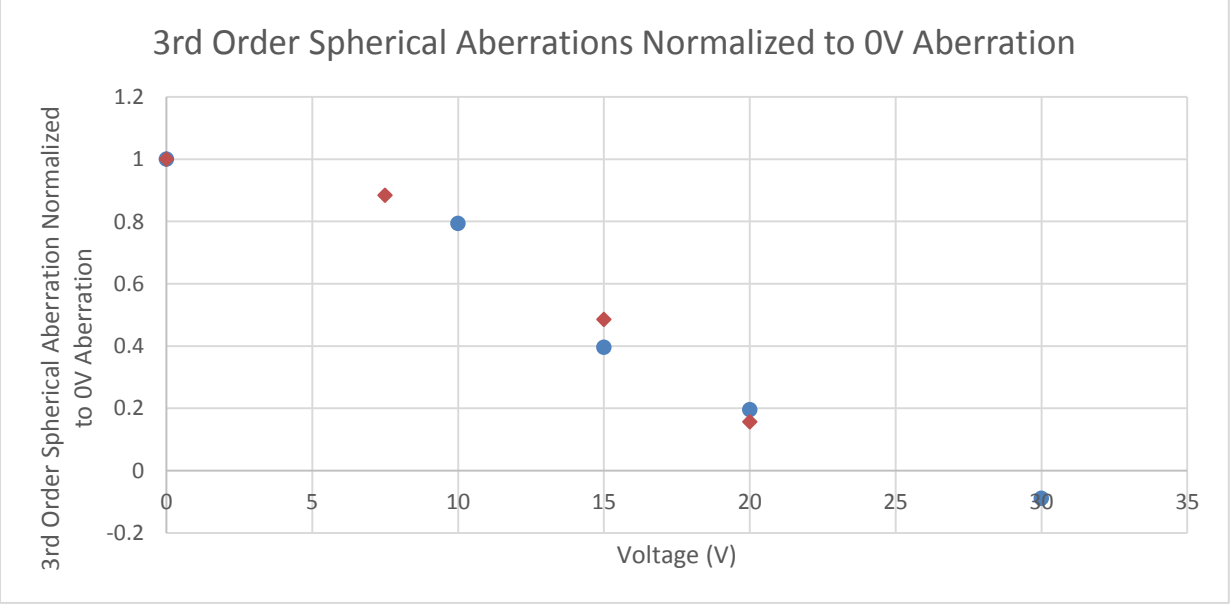

Figure B-9 Normalized Spherical Aberrations plotted against applied voltage. The two follow the same trend meaning they react the same way with applied voltage

B.7 **Validating Setup**

The exit pupil of the DUT needs to be aligned as accurately as possible with the imaging plane of the 4F system. To do this, a razor blade edge is placed in the path of the beam near the imaging plane, approximated using the focal lengths of the lenses in the system. The razor blade is then translated parallel to the laser beam axis until the razor edge comes into focus in the intensity image of the WFS software. See Figure B-10 for a diagram of this setup.

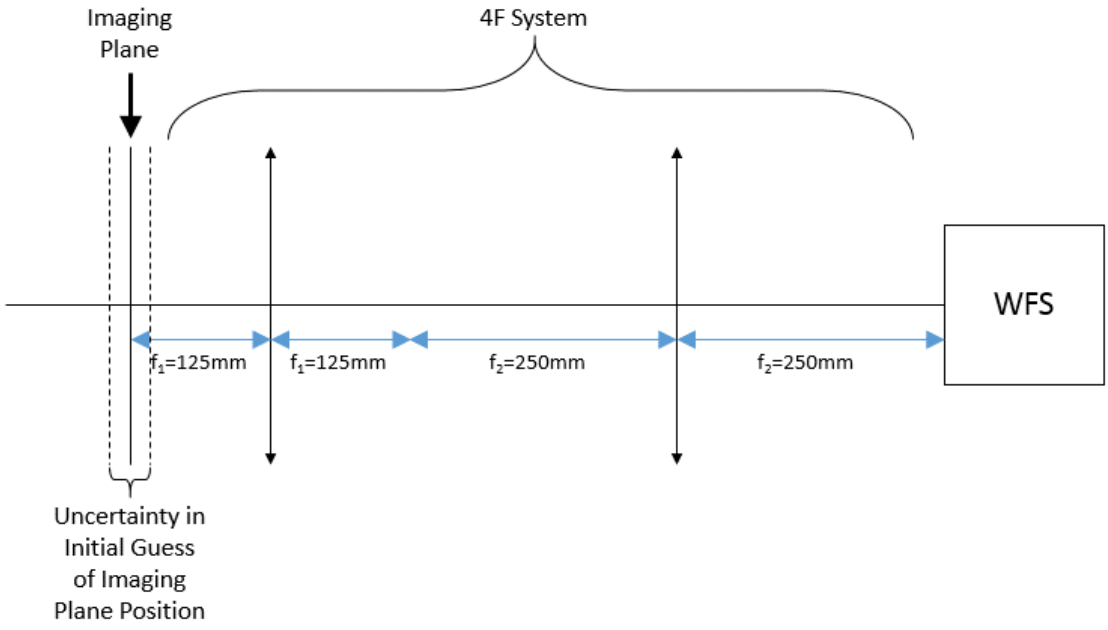

Figure B-10 Imaging plane of 4F system is found by initially guessing location of imaging plane by approximation using focal lengths of lenses, then aligning to exact imaging plane using intensity image

The point where the razor blade edge comes into focus is the imaging plane of the 4F system. Figure B-11 shows the WFS analysis window of the in-focus razor blade.

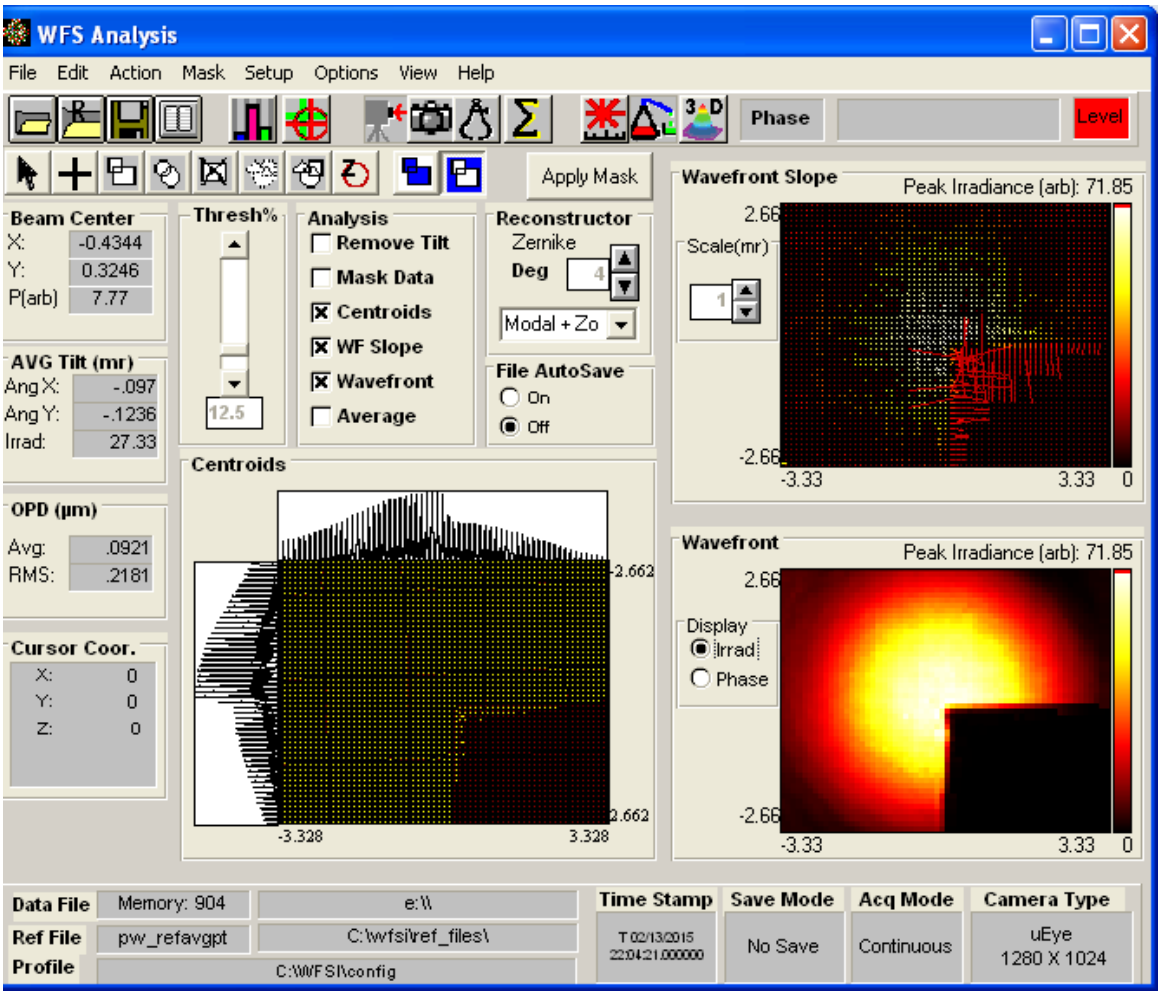

Figure B-11 Razor blade edge placed at imaging plane of the 4F system. An out-of-focus razor blade would show diffraction instead of the sharp outline of the razor blade seen here

We created a Zemax model to understand the impact of axial misalignment of the DUT from the desired imaging plane. The Zemax model describes the 4F system and lens combination and was based on the lens radius of curvature experimentally found for the EW lens at rest (0V). The measured radius of curvature is 1.478 mm, with liquid refractive indices of n=1.42 (oil) and n=1.432 (Propylene-Glycol).

Table B-1. Distance of DUT from imaging plane and subsequent third order spherical aberrations given in waves and in um (given the wavelength of light used, 0.532um)

Beam Size of 2.5mm		
Distance from Imaging Plane (mm)	Spherical abs (waves)	Spherical abs for 0.532 um wavelength (um)
0	0.287972	0.153201
0.5	0.284042	0.15111
1	0.280079	0.149002
1.5	0.276082	0.146876
2	0.272053	0.144732
2.5	0.267989	0.14257
3	0.263891	0.14039
3.5	0.259758	0.138191
4	0.25559	0.135974
4.5	0.251386	0.133737
5	0.247146	0.131482

Given a beam diameter of 2.5 mm (close to our calculated mean), Table B-1 models the third order spherical aberration with axial misalignment. The table shows that the spherical aberration value changes only 22 nm with an axial misalignment from the imaging plane of 5 mm. An axial misalignment from the imaging plane of 1 mm leads the spherical aberration value to change by only 4 nm, or 0.008 waves. The model also shows that the aberration value is unaffected by change in the magnification of the telescoping 4F system. Figure B-12 shows the ZEMAX setup in variables and ray diagram (Note the 2:3 mm offset of lens to approximate the actual lens). The file used was EW_Lens_4F_System.ZMX. These results indicate that small misalignment from the imaging plane of about 1 mm lead to negligible changes in measured aberration (around 2.6% change). The Zemax model includes the two liquids with a radius of curvature based on experimental data. For simplicity, the model did not include the glass top or bottom of the lens.

Lens Data Editor

Edit Solves View Help

	Surf:Type	Comment	Radius	Thickness	Glass	Semi-Diameter	
OBJ	Standard		Infinity	Infinity		0.000000	
1*	Standard		Infinity	2.000000	1.42,0.0	1.350000	U
2*	Standard		1.478000	3.000000	1.43,0.0	1.350000	U
3*	Standard		Infinity	5.000000		1.350000	U
4	Paraxial			10.000000		1.350000	U
5	Paraxial			5.000000		1.350000	U
STO	Standard		Infinity	0.000000		1.350000	U
IMA	Standard		Infinity	-		0.000000	U

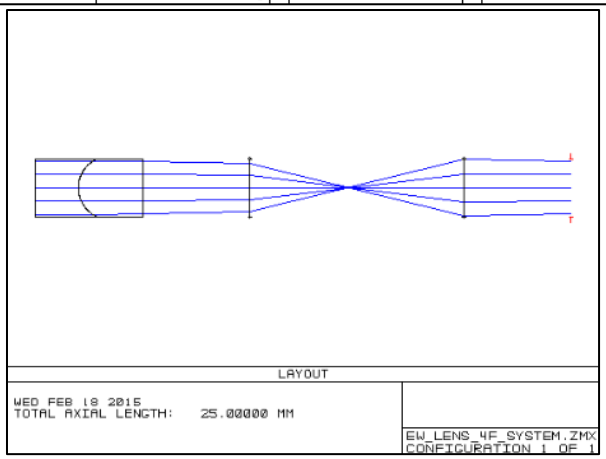

Figure B-12 Zemax setup for 4F system and electrowetting lens.

B.8 **Full Procedure for Aberration Measurements**

Equipment

1) Electrowetting (EW) Lens as device to be tested
2) Translation stages for EW lens
3) Razor blade
4) Two lenses for 4F system
5) Pinhole for verification of program (Here used 200um)
6) Test lens (optional for further verification)

Procedure

1) Align beam to rail/track using an iris, and then align the WFS to the beam as closely as possible by eye (WFS alignment mirror cover may not be in perfect alignment)
2) Start with low intensity to prevent damage to WFS, uncover WFS and Begin Acquiring Data
3) Adjust alignment of system (beam intensity profile to center of WFS) and X/Y/tip/tilt of WFS to bring OPD of phase (P-V measure) to as low a value as possible, ideally below 0.2, seen in Wavefront section of main WF analysis window.
    a. Check 'Levels' window to ensure not oversaturating or undersaturating WFS
4) Put in first lens of 4F system one focal length from WFS and align to center and to smallest point as best as possible, while being careful to limit the light intensity on the WFS
    a. Watch 'Levels' window on WFS software (keep intensity of light level at reasonable level)
    b. Program may present error and stop capturing data due to large intensity at small point. Begin acquiring until sufficiently centered/small (can realign more later with second lens in system)

5) Put in second lens of 4F system at proper location and realign beam to center of WFS with minimal OPD (assuming initial input wave had minimal OPD from step 2)
    a. Again keep an eye on 'Levels' window for proper intensity
6) Find imaging plane of 4F system using in-focus razor blade edge on the intensity plot of the WFS.
7) Check 'Origin at Beam Centroid' and 'Automatic Scale Circle' in WF Reconstructor window from main window dropdown menus.
8) Change the Magnification in the Test configuration options to magnification of 4F system
    a. To check this scaling, put ~1 mm pinhole at imaging plane and compare automatic scaled circle size (in WF Reconstructor window or Data Analysis window) with actual pinhole size
9) Verify functionality of WFS program by putting small pinhole (point source) into beam path, and checking Data Analysis, Wavefront Parameters for the calculated Radius of Curvature of phase (should be approximately same as distance from pinhole to imaging plane).
    a. Make sure light levels are sufficient for this at differing points since varying levels of light makes it to sensor at varying pinhole distances

Measuring lens wavefronts

10) Align the EW lens at imaging plane using translation stages. Align razor blade to be in focus on WFS. The position where the razor blade is in focus is

the imaging plane. Move the lens to this imaging plane. This can be done by butting lens against razor blade, recording lens position with translation stage, and moving lens away to remove razor blade. The lens can then be realigned to the imaging plane.

11) Go to Data Analysis Window, select to remove tilt
12) When ready to get data, File menu, Export as Matlab File (Data Analysis window)
    a. Alternatively, click anywhere in Expansion coefficients and choose Export selection to excel or export selection to clipboard for those values
13) Change voltage to EW lens, repeat step 12.
    a. Keep an eye on light levels in the 'Levels' window that you open from the main window. Keep around the black bar level (80%). Intensity may increase/decrease based on tuning but drastic change may be indicative of problem with the EW lens.

Analyzing data

14) Depending on desired output (RMS Deviation or Zernike Coefficients), follow algorithm of main Matlab codes listed above in this document.
    a. Calculate RMS Deviation
        i. Create mask for the phase data and mask the phase data
        ii. Calculate the best fit sphere for the masked phase data (not including the non-real zeros)

iii. Apply the same mask as from step i. to the best fit sphere

iv. Apply the RMS deviation calculation (given in the RMS Deviation section of this report) on the masked phase and masked best fit sphere data

b. Calculate Zernike Coefficients

i. Create mask for the phase data and mask the phase data

ii. Find the best fit sphere for the masked phase data (not including the non-real zeros)

iii. Apply the same mask as from step i. to the best fit sphere

iv. Subtract the masked best fit sphere from the masked phase data to get the aberration function (see Fig. 3)

v. Calculate the Zernike coefficients using the aberration function with Matlab code ZernikeCalc.m

APPENDIX C – ELECTROMECHANICAL DERIVATION OF LIPPMANN-YOUNG EQUATION

To visualize the electromechanical coupling, refer to the conservation of energy coupling figure of the input and output parameters in Figure C-1.

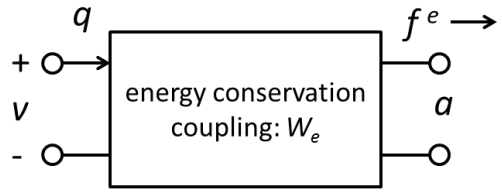

Figure C-1 Conservation of energy coupling figure that shows electrical input on the left and mechanical output on the right. A potential v delivers a charge q into the system and an energy of W_e is stored. This stored energy mechanically affects the contact line with force f^e per unit length a.

Thus, the change in energy by charging the capacitor must be balanced by the change in contact line force [72]:

$$\mathrm{d}W_e = v\mathrm{d}q - 2\pi a f^e \mathrm{d}a \qquad \text{C.1}$$

where electrical charge $q = C(a)v$ and the stored electrical energy is $W_e(q, a)$. The electrical force per length f^e acts in the direction of contact line motion, parallel to the dielectric film and radially outward.

It is desirable to express the energy as a function of voltage, a controllable independent variable for electrowetting systems. To make this change of variables, the concept of coenergy can be used [73]. Coenergy is a non-physical quantity that is described by the linear relationship between input and stored energy in conservative systems. For example, in the charge-voltage relationship of a capacitor,

seen in Figure C-2, the area under the curve represents the energy stored in the capacitor while the area above the curve represents the corresponding coenergy.

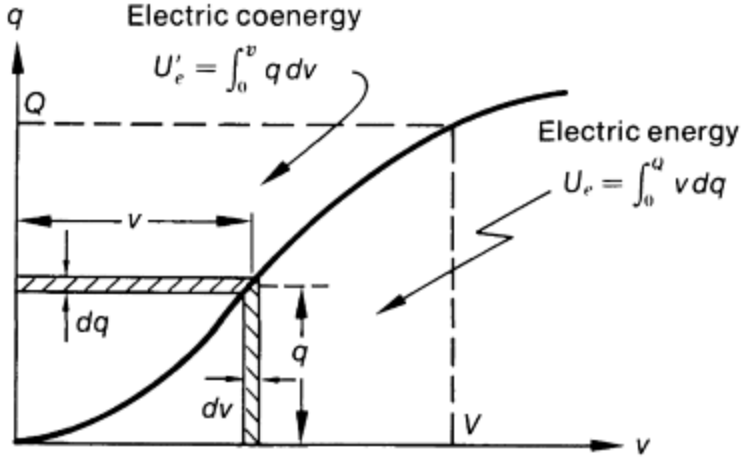

Figure C-2 Electric energy and coenergy in a capacitor. Coenergy describes the area above the curve while actual stored energy is the area below the curve. In a linear electrical system, coenergy is equal to energy. Figure from [74].

Though it has no physical meaning, coenergy is useful in analyzing the electromechanical electrowetting system. Since coenergy W_e' is equal to the stored energy, it follows that:

$$W_e + W_e' = vq \qquad \text{C.2}$$

By using equations C.1 and C.2, we effectively exchange the energy for coenergy and the voltage / charge relationship.

$$\mathrm{d}W_e' = q\mathrm{d}v + 2\pi a f^e \mathrm{d}a \qquad \text{C.3}$$

Boundary conditions require that $f^e(v = 0, a) = 0$. Thus, we can integrate the differential coenergy in terms of v, a to obtain the coenergy [72]:

$$W_e'(v, a) = \frac{1}{2} C(a) v^2 \qquad \text{C.4}$$

Since the function is analytical, we can use equation 2.8 to write

$$f^e = \frac{1}{2\pi a}\frac{\partial W_e'}{\partial a} \quad \text{C.5}$$

And holding a constant voltage, equation C.5 can be expressed as

$$f^e = \frac{1}{2\pi a}\frac{v^2}{2}\frac{\mathrm{d}C}{\mathrm{d}a} \quad \text{C.6}$$

By taking the final derivative of capacitance with respect to droplet contact radius, the electrically induced force per unit length on the contact line is expressed as:

$$f^e = \frac{\epsilon_d \epsilon_0}{2d} v^2 \quad \text{C.7}$$

One aspect interesting to note is that the force acting on the contact line is not a function of the droplet area in contact, but only of the dielectric material and applied voltage. To arrive at the final Lippmann-Young equation governing contact angle change due to applied electric force, the two contact line forces from equations 2.9 and equations C.7 are set in equilibrium $f^e = -f$.

$$cos\theta(v) = cos\theta^Y + \frac{\epsilon_d \epsilon_0}{2d\gamma_{LV}} v^2 \quad \text{C.8}$$